

**Backward ϕ photo-production from C and Cu
targets at $E_\gamma = 1.5 - 2.4$ GeV**

A dissertation presented

by

Takahiro Sawada



The Department of Physics in partial fulfillment of the requirements
for the degree of Doctor of Philosophy in the subject of Physics

Research Center for Nuclear Physics (RCNP)

Osaka University

10-1, Mihogaoka, Ibaraki, Osaka 567-0047, Japan

March 2013

Abstract

The backward ϕ photo-production from C and Cu targets at $E_\gamma = 1.5\text{-}2.4$ GeV has been studied at SPring-8/LEPS facility. This is the first measurement of the photo-produced ϕ mesons from nuclear targets with momentum less than 1.2 GeV/ c , where the ϕ mesons were identified from the K^+K^- invariant mass distributions. We have derived the transparency ratio from the production rates of ϕ mesons over the range of $0.3\text{-}2.0$ GeV/ c . We have confirmed that the transparency ratio decreases with ϕ momentum. We have performed the validation on the momentum dependence of $\sigma_{\phi N}$. The result suggests that $\sigma_{\phi N}$ increases as p_ϕ , although it is not statistically significant. We have confirmed that $\sigma_{\phi N}$ obtained in the low p_ϕ region is consistent with the theoretically predicted value in free space. The reduction of the transparency ratio shown in the high p_ϕ region suggests that a diffractive ϕ photo-production might have a strong A -dependence.

Contents

Title Page	1
Abstract	3
Table of Contents	4
List of Figures	6
List of Tables	11
1 Introduction	12
2 Experiment	17
2.1 SPring-8 Facility	17
2.2 Overview of LEPS Facility	19
2.3 Photon Beam	19
2.3.1 Backward Compton Scattering (BCS)	19
2.3.2 Laser Injection System	22
2.3.3 Photon Energy Tagging System	23
2.4 Nuclear Targets	23
2.5 Time Projection Chamber (TPC)	24
2.6 Trigger Counters	25
2.7 LEPS Spectrometer	26
2.7.1 Upstream-Veto Counter	26
2.7.2 Silica-Aerogel Čerenkov Counter	26
2.7.3 Drift Chambers	27
2.7.4 TOF Wall	28
2.7.5 Dipole Magnet	28
2.8 Data Acquisition	29
2.9 Coordinate System	32
3 Analysis	33
3.1 Outline of Data Analysis	33
3.2 Event Selection for the $\phi \rightarrow K^+K^-$ events	33
3.2.1 Tagging Counter	34
3.2.2 Number of Good Tracks	35
3.2.3 Particle Identification (PID)	36
3.2.4 Distance of Closest Approach (DCA) Cut	38
3.2.5 Veretex	40
3.2.6 Missing Mass	42
3.2.7 Summary of Selection Cuts	43
3.3 Yield of ϕ meson	46

4	Results and Discussions	48
4.1	Transparency Ratio T	48
4.2	Discussion	51
5	Conclusion	55
A	General Properties, Mechanical Design, and Operation of the TPC	57
A.1	General Properties of the TPC	57
A.1.1	Working Principle of the TPC	57
A.1.2	Gas Ionization by Charged Particles	58
A.1.3	Motion of Charge Carriers in Gases	59
A.1.4	Signal Formation	60
A.2	Mechanical Design and Operation of the TPC	61
A.2.1	Choice of Gas Mixture	61
A.2.2	Electric Field	61
A.2.3	Magnetic Field	62
A.2.4	Gas Amplification	62
B	Analysis Procedure for TPC	66
B.1	Outline	66
B.2	Preprocessing	67
B.2.1	Waveform Reconstruction from the Saturated Signals	67
B.2.2	Time Offset and Gas Mobility	67
B.3	Cluster Reconstruction	68
B.3.1	Cluster Reconstruction	68
B.3.2	Amount of Charge in Each Signal	70
B.3.3	Gain Calibration	71
B.4	Hit Reconstruction	71
B.5	Track Reconstruction	72
B.6	Particle Identification (PID)	73
B.6.1	Truncation and Weighted Average of dE/dx	73
B.6.2	Gain Drop due to the Space Charge	76
B.6.3	Selection Boundaries of dE/dx	81
C	Acceptance Correction	84
D	Scattering of Emitted Nucleon	86
E	Model Calculations	89
E.1	Glauber Approximation	89
E.2	Decay Probability inside the Nucleus	90
	Bibliography	92
	Acknowledgments	95

List of Figures

1.1	Masses of ρ , ω , and ϕ mesons as a functions of density, which is normalized by the normal nuclear density ρ_0 , predicted by Hatsuda and Lee [2,3]. The hatched regions represent the theoretical uncertainties which are caused in estimating quark condensates from limited experimental information.	12
1.2	e^+e^- invariant mass distributions obtained in p+Cu for slow ($\beta\gamma < 1.25$) ϕ mesons at KEK-PS E325 [4].	12
1.3	Conceptual diagrams of the incoherent ϕ photo-production from a nucleus (left), the A -dependence of the incoherent photo-production cross section (center), and the A -dependence of the transparency ratio (right).	13
1.4	(a) Missing energy spectrum of ϕ photo-production for the Li target. The hatched regions show the calculated spectra for the coherent and the incoherent processes by the Monte Carlo simulation, and the normalization is made to guide the eyes. (b) A -dependence of the number of events for ϕ photo-production from nuclei after the contribution of coherent production is subtracted. The data points are fitted with the parameterization $A^{0.72}$ [15].	14
1.5	Transparency ratios for the ϕ meson, normalized to carbon, as a function of the atomic mass A . The curves are Glauber calculations where the σ_{VN} is given in the legend.	15
1.6	Momentum dependence of the transparency ratio for ω (left) [16], η' (center) [17], and ϕ mesons (right) [19].	16
1.7	In-medium widths and inelastic meson-nucleon cross sections for ω (left) [16], η' (center) [17], and ϕ mesons (right) [19].	16
2.1	Location of SPring-8.	17
2.2	Aerial photograph of SPring-8 in September 2011.	18
2.3	Schematic configuration of the SPring-8 accelerator complex.	18
2.4	Schematic view of the LEPS facility at SPring-8. The facility consists of a laser-electron collision part in the storage ring, a tagging system, a laser hutch for a laser injection, and an experimental hutch. A schematic explanation of the collision between an electron and a laser photon in backward-Compton scattering is inserted in the figure.	19
2.5	Schematic view of the time projection chamber (TPC) and the LEPS spectrometer in an experimental hutch. The TPC sits in a solenoidal magnet, and surrounds the nuclear target. The LEPS spectrometer consists of a dipole magnet, three multi-wire drift chambers (DC1, DC2 and DC3), a plastic scintillator hodoscope (TOF wall), a plastic scintillator (Start Counter) and a silica aerogel Čerenkovcounter.	20
2.6	Difference in the configuration of experimental apparatuses and the detector acceptances between in the “LEPS standard setup” (top) and in the “TPC experiment setup” for this experiment (bottom). The detector acceptances are shown with the colored areas.	21
2.7	Kinematical variables of the backward-Compton-scattering process in the laboratory frame.	22

2.8	The differential cross section of BCS process (left) and the polarization as a function of the photon energy (right).	22
2.9	Schematic view of the laser operation system.	23
2.10	Schematic view of the tagging system.	24
2.11	Pictures of the nuclear targets: CH ₂ (left), C (center), and Cu (right).	24
2.12	Perspective view of the TPC and the side trigger counters. The arrows (from a to f) indicate the side trigger counters.	24
2.13	Cross sectional side view of the TPC.	24
2.14	Schematic drawing of the forward trigger counters (TPC-FWD). TPC-FWD consists of two trapezoidal scintillation counters and the other two rectangular ones. The start counter (SC) is placed just downstream of the TPC-FWD.	25
2.15	Schematic drawing of the start counter (SC).	26
2.16	Relation between momentum and β for e^+e^- , π and K . A particle with $\beta > 1/n$ emits Čerenkov lights. The line corresponding to an index of 1.03.	27
2.17	Silica aerogel Čerenkov counter (AC).	27
2.18	Schematic drawing of the wire configuration in the drift chambers.	28
2.19	Drawing of the TOF wall.	29
2.20	Distribution of the magnetic field B_y as a function of the z -position at $x=0$ and $y=0$. The position of $z=0$ corresponds to the center of the dipole magnet.	29
2.21	Diagram of the readout circuits for triggers.	30
2.22	Diagram of the readout circuits for triggers.	32
3.1	Notations for the each detection mode.	34
3.2	Distributions of the number of tracks in the tagging counter ($ntag$) for the C (left) and Cu (right) target run.	34
3.3	Distributions of the incident beam photon energy (E_γ) for the C (left) and Cu (right) target run.	35
3.4	Distributions of the number of good tracks in the TPC for the C (left) and Cu (right) target run.	36
3.5	Distributions of the number of good tracks in the LEPS spectrometer for the C (left) and Cu (right) target run.	36
3.6	Distribution of the probability of χ^2 for track fitting in the TPC for the C (left) and Cu (right) target run.	36
3.7	Distribution of the probability of χ^2 of track fitting in the LEPS spectrometer for the C (left) and Cu (right) target run.	37
3.8	Correlation between the momentum/charge and the square of mass reconstructed by the LEPS spectrometer for C (left), and Cu (right) target, after the number of good tracks cut is applied. The red lines indicate the boundaries for the K^+ and K^- selection.	38
3.9	The distribution of the DCA between the K^+ and the K^- tracks. Arrows indicate selection regions.	38
3.10	The distribution of the DCA between the proton track and K^+K^- vertex. Arrows indicate selection regions.	39
3.11	Vertex distribution for the K^+K^- in the x - y plane. The rectangles indicate the selection regions for the vertex cuts in the x - y plane.	40
3.12	Position of the Target. In the figure for C target (left), the data points show the z -coordinates of the upstream and the downstream edge of the C target. In the figure for Cu target (right), the data points show the z -coordinates of the center of Cu target.	41

3.13	Distributions of the z -vertex (vtz) of K^+K^- pair after the vertex selection cut in x - y plane. The origins are the center of targets. The arrows indicate the selection regions.	42
3.14	Distributions of the square of the missing mass for the reaction $\gamma p \rightarrow K^+K^- X$ ($MM^2(K^+K^-)$). The black(red) histogram represents the observed(simulated) data. The scaling of simulated data is determined arbitrarily. The arrows indicate the selection regions.	43
3.15	The invariant mass spectra of the final K^+K^- sample in the $tpcK^+K^-P$ (top), $tpcK^+K^-spP$ (center), and $tpcK^\pm PspK^\mp$ mode (bottom). The black, red, green, and blue lines represent the data, the fit results, the backgrounds, and the expected $\phi \rightarrow K^+K^-$ shapes, respectively.	47
4.1	Transparency ratio T for ϕ mesons on Cu target normalized to the C target, as a function of the ϕ momentum. The closed black points represent the result in this experiment. The open circle represents the result in the previous experiment, extracted only from C and Cu data.	51
4.2	The transparency ratio and the model calculations on the basis of some different models. The data obtained from this experiment are shown with closed blacks. The data obtained from the previous experiment [15], extracted only from C and Cu target, are superimposed into the same plot with open circles. The green dotted lines with the numerical values show the model calculations using the parameter α of the numerical values. The red lines show the results of fitting for the data obtained only from this experiment, and the blue lines show the results of fitting for the data obtained both from this experiment and the previous experiment.	53
A.1	Conceptual diagram for the working principle of a TPC. A particle passing through the gas cylinder volume produces free electrons along its track trajectory. Those ionization electrons drift towards the sense wires, and produce the avalanches in the immediate area of sense wires. The charges detected on the cathode pads give a two-dimensional projection of the particle trajectory. Combined with a measurement of the drift time, the particle trajectory in three dimension is reconstructed.	57
A.2	The distribution of the expected cluster size (left) and the distribution of the expected number of clusters per cm (right) assuming that the charged particle is proton with 0.5 GeV/c, and the volume is filled with Ar/CH ₄ (90:10) gas mixture at P = 1 atm, T = 300 K and B = 2 T. The effects of the argon M and L -shells are clearly seen in the left figure.	58
A.3	The drift velocities of electron as a function of the strength of electric field in several gases at P = 1 atm, T = 300 K and B = 2 T. The dotted line shows the setting value of electric field (180 V/cm) for the operation in this experiment.	61
A.4	The calculated electric field map in the TPC. The lines with green color show the equipotential lines, and the numerical values with yellow color show the electric potentials. Here, the length of the field cage in the z -direction is shorter than the real length.	62
A.5	The magnetic field B_z (a) and B_y (b) on the vertical plane ($x=0$ mm) around the TPC. The rectangles indicate the active volume of the TPC, and the cross marks indicate the center positions of the targets.	63
A.6	Schematic view of the gas amplification part of the TPC.	64
A.7	Drift lines of electrons from track when gate is opened (a) and closed (b). Drift lines of positive ions from sense wires when gate is closed (c).	64
A.8	The configuration of the cathode pad plane.	65

B.1	Conceptual diagram of data analysis: cluster reconstruction (left), hit reconstruction (center), and track reconstruction (right).	66
B.2	A saturated waveform (solid line) and a corrected one (dotted line) in a certain signal. . .	67
B.3	The mobility of the electron in the active volume of the TPC as a function of the run number.	68
B.4	T_0 of each FADC channel.	68
B.5	(a): A track flying parallel to the sense wire plane where the three sense wires (black, red, blue) are located on one cathode pad. (b): The induced currents (I_{out}) on the cathode pad arises from avalanches on each sense wire. Each lines are corresponding to the signals from the sense wire with same color. (c): Observed signal which is equal to the sum of components from each wires. (d)~(f): In the case of a track flying at an angle with the sense wire plane.	69
B.6	Conceptual diagrams of the cluster reconstruction.	70
B.7	The most probable value of energy deposition in every cathode pads before (top) and after (bottom) applying the gain correction.	71
B.8	The most probable value of energy deposition in every run before (top) and after (bottom) applying the gain correction.	72
B.9	Conceptual diagrams of $(dx)_{cathode}$ (left) and $(dx)_{hit}$ (right).	73
B.10	Distributions of $(dE/dx)_{wav}$ from the MIP particles with the various truncations: the simple average (a), the weighted average without truncation (b), and the weighted averages with $6\sigma \sim 1\sigma$ truncations (c)~(h). The red lines show the fit results with Gaussian. . . .	75
B.11	“RMS of $(dE/dx)_{wav}$ ” / $\langle (dE/dx)_{wav} \rangle$ with $6\sigma \sim 1\sigma$ truncations. The black and red lines show the results of the simple and the weighted average values without truncation.	76
B.12	A sample of $(dE/dx)_{hit}$ resolution as a function of the energy deposition, at layer 4 and at polar angle between 30 and 40 degrees.	76
B.13	Contour plots of potential near a sense wire without (left) and with (right) the space charge effect, calculated using the GARFIELD program [32]. The space charge reduces the gradient of potential.	77
B.14	The conceptual diagram of the local reduction of the electric field near a sense wire. The blue and red lines shows the electric fields without (left) and with (right) the space charge effect.	77
B.15	Correlation plots suggesting the magnitude of gain drop effect. Horizontal axis represents the <i>observed</i> avalanche density on sense wires, which is the result after the gain drop. Vertical axis represents the <i>expected</i> avalanche density on sense wire without the gain drop, assuming that the charged particle is p , K^+ , d , and π^- in the 1st ~ 4th rows, respectively. The curved line is the function representing the magnitude of gain drop effect.	79
B.16	Correlation between the dE/dx and the track polar angle of a positively charged particle measured by the TPC before (top) and after (bottom) the gain drop correction.	80
B.17	Correlation between the dE/dx and the momentum of a positively charged particle measured by the TPC before (top) and after (bottom) the gain drop correction. The red lines show the expected energy losses given from the Bethe-Bloch formula.	80
B.18	Conceptual diagram for obtaining the peak positions <i>Mean</i> and the widths <i>Sigma</i> of p and π^+ in the distribution of $(dE/dx)_{cathode}$ at certain polar angle and momentum.	81
B.19	Correlation plot between the <i>Mean</i> and the <i>Sigma/Mean</i> at various polar angles and momenta. The <i>Mean</i> and the <i>Sigma/Mean</i> are corresponding to the $(dE/dx)_{cathode}$ and the 1σ relative deviation of $(dE/dx)_{cathode}$, respectively.	81

- B.20 The yields of ϕ mesons as a function of the selection boundary cuts for Kaon in the $tpcK^+spK^-$ and $tpcK^-spK^+$ mode. The blue and red points represents the yields of ϕ mesons in the $tpcK^+spK^-$ and $tpcK^-spK^+$ mode, respectively. The data show a good agreement with the statistical expectation (black line). 82
- B.21 The yields of ϕ mesons as a function of the selection boundary cuts for Kaon in the $tpcK^+K^-$ mode. The red points represents the yields of ϕ mesons in the experimental data. The data show a good agreement with the statistical expectation (black line). . . . 82
- B.22 The ratio “Error of the yield of ϕ mesons / Yield of ϕ mesons” as a function of the selection boundary cuts for Kaon in the $tpcK^+spK^-$ and $tpcK^-spK^+$ mode. The blue and red points correspond to the $tpcK^+spK^-$ and $tpcK^-spK^+$ mode, respectively. The optimal selection boundary cut for Kaon is set to be 2.0σ where the ratio is minimized. 83
- B.23 The ratio “Error of the yield of ϕ mesons / Yield of ϕ mesons” as a function of the selection boundary cuts for Kaon in the $tpcK^+K^-$ mode. The optimal selection boundary cut for Kaon is set to be 1.5σ where the ratio is minimized. 83
- C.1 (Left): The transparency ratio for proton in the $\gamma A \rightarrow \pi^+\pi^-pX$ process as a function of the proton momentum in the $tpc \pi^+\pi^-p$ detection mode. The red points represent the results from Monte Carlo simulation with GHEISHA routine and the black points represent the results from experimental data. (Right): The ratio of the transparency ratios obtained from the Monte Carlo simulation and the experimental data. The black line is only guide line drew by eye. 85
- C.2 (Left): The transparency ratio for proton in the $\gamma A \rightarrow \pi^+\pi^-pX$ process as a function of the proton momentum in the $tpc \pi^\pm p sp \pi^\mp$ detection mode. The red points represent the results from Monte Carlo simulation with GHEISHA routine and the black points represent the results from experimental data. (Right): The ratio of the transparency ratios obtained from the Monte Carlo simulation and the experimental data. The black line is only guide line drew by eye. 85
- D.1 The $MM(K^+K^-p)$ distributions from C target. Each figure in left, center, or right column corresponds to the momentum of the emitted nucleon, and in top or bottom row corresponds to $tpcK^\pm P spK^\mp$ or $tpcK^+K^-P$ mode, respectively. The black, red, and blue lines show the experimental data, the components from no-scattering or elastic scattering, and the components from inelastic scattering. The number of percentage in figures represents the ratio of no-scattering or elastic scattering components to all. 87
- D.2 The $MM(K^+K^-p)$ distributions from Cu target. Each figure in left, center, or right column corresponds to the momentum of the emitted nucleon, and in top or bottom row corresponds to $tpcK^\pm P spK^\mp$ or $tpcK^+K^-P$ mode, respectively. The black, the red, and the blue lines show the experimental data, the components from no-scattering or elastic scattering, and the components from inelastic scattering. The number of percentage in figures represents the ratio of no-scattering or elastic scattering components to all. 88
- E.1 The transparency ratio T as a function of the emission angle of ϕ meson. The numerical values represent the assumed value of $\sigma_{\phi N}$ 90
- E.2 The conceptual diagram of the ϕ mesons decay inside the nucleus or outside the nucleus (left), and the relation N_ϕ^{in}/N_ϕ^{out} and p_ϕ for C and Cu nuclei obtained by the Monte Carlo calculation (right). 91

List of Tables

2.1	Specification of the Linac, the Booster Synchrotron and the Storage Ring of the SPring-8 [23].	18
2.2	Properties of the nuclear targets used in this experiment [24].	25
2.3	Design parameters of the DC's. The location of the center of each DC along the z-axis is measured from the center of the dipole magnet.	28
3.1	The total number of beam photons and trigger-accepted events	33
3.2	Summary of Trigger and Tagging counter cuts in all detection modes.	43
3.3	Summary of ϕ selection cuts in $tpcK^+K^-P$ mode.	44
3.4	Summary of ϕ selection cuts in $tpcK^+K^-spP$ mode.	44
3.5	Summary of ϕ selection cuts in $tpcK^+PspK^-$ mode.	45
3.6	Summary of ϕ selection cuts in $tpcK^-PspK^+$ mode.	45
3.7	The measured yields of ϕ meson.	46
4.1	Properties of nuclear targets used in this experiment.	49
4.2	Attenuation of the photon flux in the target.	50
4.3	Geometrical acceptance	50
4.4	The measured transparency ratio T .	51
4.5	Summary of the degree of coincidence between the experimental data and each models.	52
A.1	Characteristics of the wire grids.	63

Chapter 1

Introduction

The properties of hadrons, such as a mass, a decay width, and a branching ratio, have been extensively studied in the particle physics. The recent interests have been extended to understand how these properties are modified in a hot and/or dense matter. This issue is of fundamental importance since such modifications are related to the basic nature of the QCD. Theoretically, the possibility of a decreasing of the light vector meson masses in a nuclear medium was first pointed out by Brown and Rho [1]. Hatsuda and Lee calculated the density dependence of the ϕ meson mass based on a QCD sum rules as shown in Fig. 1.1.

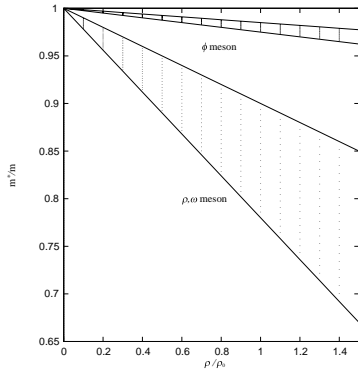


Figure 1.1: Masses of ρ , ω , and ϕ mesons as a functions of density, which is normalized by the normal nuclear density ρ_0 , predicted by Hatsuda and Lee [2, 3]. The hatched regions represent the theoretical uncertainties which are caused in estimating quark condensates from limited experimental information.

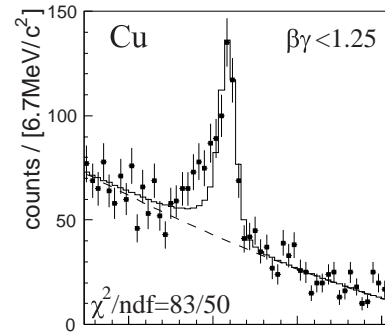


Figure 1.2: e^+e^- invariant mass distributions obtained in p+Cu for slow ($\beta\gamma < 1.25$) ϕ mesons at KEK-PS E325 [4].

The ϕ meson, which is a vector meson of an almost pure $s\bar{s}$ state, has attractive features as a probe to detect possible changes of its properties in the nuclear medium. The main modifications of the ϕ property in the nuclear medium are expected to be a dropping of its mass and a broadening of its spectral function due to the partial restoration of the chiral symmetry [2, 3] or the meson-nucleon interaction in the nuclear medium [5–9].

The most direct approach to observe the in-medium ϕ properties is a reconstruction of its mass spectra from the dilepton decay channel since this final state is free from the influence of hadronic interactions

in a nucleus. However, the small branching ratios for leptonic decays reduce the statistical quality of ϕ mesons, and many leptons produced by the many hadronic sources reduce the signal-to-background ratio. The KEK-PS-E325 collaboration has measured the ϕ production via the e^+e^- and K^+K^- decay channels in 12 GeV $p + A$ reactions. The e^+e^- invariant mass spectra from copper target indicated the significant excess on the low-mass side of the ϕ meson peak in the $\beta\gamma < 1.25$ region as shown in Fig. 1.2. They have estimated as a mass shift of 3.4% and a width increase by a factor of 3.6 at nuclear density ρ_0 from the e^+e^- spectrum [4]. However, the JLab/CLAS collaboration reported the e^+e^- spectrum with no significant mass shift from C, Ti, Fe, and Pb targets at $E_\gamma < 4$ GeV [10]. The verification of a mass-shift still requires more work.

Instead of obtaining the in-medium ϕ properties from fits to the observed invariant mass peak, the method of using the variation of the incoherent ϕ photo-production cross sections with the nuclear mass number A has been studied both theoretically [9, 11–14] and experimentally [10, 15–19]. This method has the advantage of being able to exploit the dominant K^+K^- branching ratio ($\sim 50\%$).

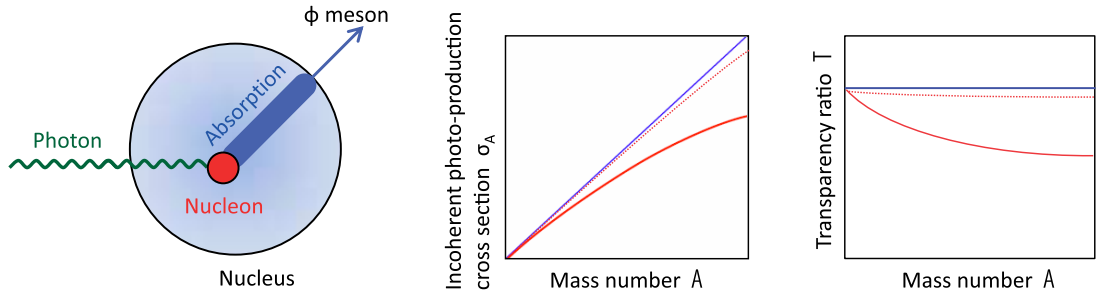


Figure 1.3: Conceptual diagrams of the incoherent ϕ photo-production from a nucleus (left), the A -dependence of the incoherent photo-production cross section (center), and the A -dependence of the transparency ratio (right).

The conceptual diagram of the incoherent ϕ photo-production from a nucleus is shown in Fig. 1.3 (left). A incident photon produces the ϕ meson on one nucleon in the nucleus. The nucleus is nearly transparent to the incident photon beams since the γ -nucleon total cross section ($\sigma_{\gamma N}$) is only ~ 0.14 mb at $E_\gamma = 1.5$ -2.4 GeV [20], which is approximately 200 times smaller than $\sigma_{\pi^\pm N}$ or σ_{pN} in this energy range. All of the nucleons in a nucleus participate to the ϕ photo-production, thus the total amount of ϕ mesons produced on the nucleons in a nucleus is expected to be proportional to the target mass number A .

The conceptual diagrams of the A -dependence of the incoherent ϕ photo-production cross section is shown in Fig. 1.3 (center). The ϕ -nucleon interaction cross section ($\sigma_{\phi N}$) is expected to be suppressed due to the OZI rule. Therefore, the incoherent ϕ photo-production cross section from a nucleus (σ_A) is expected to be close to the proportion with the target mass number A , as shown with the red dotted curve in Fig. 1.3 (center). On the other hand, if the ϕ meson flux is more decreased during passing through the more heavier nucleus or the ϕ production is more decreased on the more heavier nucleus, the A -dependence of σ_A deviates as shown with the red solid curve in Fig. 1.3 (center).

The conceptual diagram of the A -dependence of the transparency ratio is shown in Fig. 1.3 (right). The transparency ratio is defined as:

$$T_A = \frac{\sigma_{\gamma A \rightarrow \phi X} / A}{\sigma_{\gamma N \rightarrow \phi X}}. \quad (1.1)$$

Here, $\sigma_{\gamma A \rightarrow \phi X}$ is the incoherent ϕ photo-production cross section from a nucleus with the target mass

number A and $\sigma_{\gamma N \rightarrow \phi X}$ is the ϕ photo-production cross section on a free nucleon. If $\sigma_{\phi N}$ in the nuclear medium is the same as that in free space, T_A is expected to be close to unity, as shown with the red dotted curve in Fig. 1.3 (right). On the other hand, if the ϕ meson flux is more decreased during passing through the more heavier nucleus or the ϕ production is more decreased on the more heavier nucleus, the A -dependence of T_A deviates as shown with the red solid curve in Fig. 1.3 (right). To avoid the systematic uncertainties, the transparency ratio has been normalized to the carbon data:

$$T_{A/C} = \frac{\sigma_{\gamma A \rightarrow \phi X}/A}{\sigma_{\gamma C \rightarrow \phi X}/A_C}. \quad (1.2)$$

Both the A -dependence of the σ_A and the A -dependence of the T are related to the $\sigma_{\phi N}$ in the nuclear medium. The $\sigma_{\phi N}$ in the nuclear medium is extracted from the A -dependence of the σ_A or the A -dependence of the T , by comparing these data with the theoretical calculations based on the Glauber approximation. The detail of this procedure is described in Appendix. E.

The value of $\sigma_{\phi N}$ in the nuclear medium was reported by the SPring-8/LEPS collaboration [15]. The ϕ photo-production from Li, C, Al, and Cu targets has been measured via the K^+K^- decay channel at $E_\gamma = 1.5$ -2.4 GeV in the ϕ momentum range of 1.0-2.2 GeV/ c (the average ≈ 1.8 GeV/ c). After subtracting the coherent contributions, the incoherent ϕ photo-production cross section (σ_A) turned out to be proportional to $A^{0.72 \pm 0.07}$, as shown in Fig. 1.4, where A is the target mass number. The ϕ -nucleon interaction cross section ($\sigma_{\phi N}$) in the nuclear medium was estimated to be 35^{+17}_{-11} mb using the Glauber multiple scattering theory, while $\sigma_{\phi N}$ is predicted to be ≈ 10 mb from the theoretical calculations [21,22].

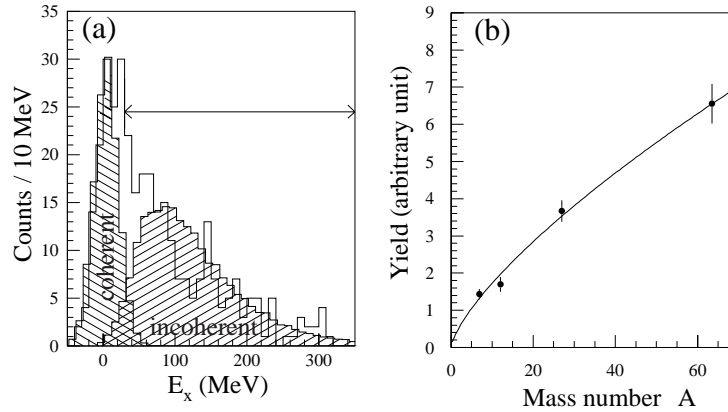


Figure 1.4: (a) Missing energy spectrum of ϕ photo-production for the Li target. The hatched regions show the calculated spectra for the coherent and the incoherent processes by the Monte Carlo simulation, and the normalization is made to guide the eyes. (b) A -dependence of the number of events for ϕ photo-production from nuclei after the contribution of coherent production is subtracted. The data points are fitted with the parameterization $A^{0.72}$ [15].

The value of $\sigma_{\phi N}$ in the nuclear medium was also reported by the JLab/CLAS collaboration [10]. The ϕ photo-production from ^2H , C, Ti, Fe, and Pb targets has been measured via the e^+e^- decay channel at $E_\gamma < 4$ GeV. The value of $\sigma_{\phi N}$ was estimated to be 16-70 mb from the transparency ratio measurement for an average ϕ momentum of 2 GeV/ c . This value was also large and consistent with the result from SPring-8/LEPS, although its error was large. The results are shown in Fig. 1.5.

The momentum dependence of the transparency ratio were reported by the COSY/ANKE collaboration [19]. The ϕ meson production in proton collisions with C, Cu, Ag, and Au targets has been measured

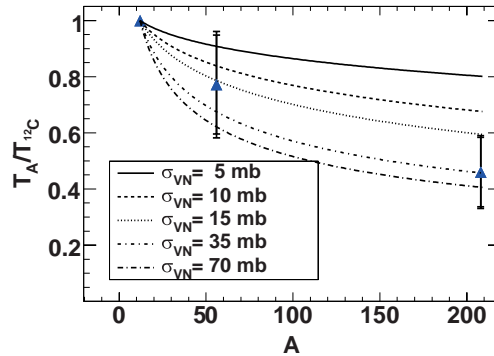


Figure 1.5: Transparency ratios for the ϕ meson, normalized to carbon, as a function of the atomic mass A . The curves are Glauber calculations where the σ_{VN} is given in the legend.

via the K^+K^- decay at an incident proton beam energy of 2.83 GeV. Although it is not easy to extract the information from the transparency ratio in proton induced reaction, there were indications of a significant momentum dependence in the transparency ratio and in the value of the extracted $\sigma_{\phi N}$. $\sigma_{\phi N}$ was estimated to be 14-21 mb over the momentum range of 0.6-1.6 GeV/ c , as shown in Fig. 1.6 (right) and Fig. 1.7 (right).

On the other hand, the CBELSA/TAPS collaboration reported that there is no momentum dependence for the ω mesons [16] and for the η' mesons [17]. in photo-nuclear reactions. A comparison to transport calculations gave the widths of 130-150 MeV for ω mesons and 15-25 MeV for the η' mesons at $\rho = \rho_0$, respectively. And the $\sigma_{\omega N}$ and $\sigma_{\eta' N}$ were estimated to be ≈ 70 mb and 3-10 mb. The transparency ratio were almost constant whereas the ϕ mesons indicated the momentum dependence. These results are shown in Fig. 1.6 and Fig. 1.7. They also reported that there is no momentum dependence for $\sigma_{\eta N}$ (≈ 30 mb) by the A -dependence measurement of η mesons production cross section.

In order to get a deeper insight into the properties of the ϕ meson in the nuclear matter, we have performed the new experiment. In this thesis, we report the backward ϕ photo-production from C and Cu targets at $E_\gamma = 1.5$ -2.4 GeV at SPring-8/LEPS facility. The data has been taken from September to December in 2004. The ϕ meson production using the photon beam allow us to extract the ϕ meson properties in the nuclear matter from the transparency ratio, with less ambiguity. We have measured the momentum dependence of the transparency ratio for the ϕ mesons, and verified the result of COSY/ANKE collaboration. By increasing the detector acceptance, covering a wider range of ϕ momentum compared to our previous reports [15], and adopting much improved analysis procedures, we have examined the transparency ratio of ϕ meson over the range of 0.3-2.0 GeV/ c . In the lower p_ϕ region, the ratio of the ϕ mesons decay inside the nucleus is higher, therefore the more accurate information in the nucleus is extracted. This is the first measurement of the photo-produced ϕ mesons from nuclear targets with momentum less than 1.2 GeV/ c , thus the more reliable result is expected. In the higher p_ϕ region, it allows us to perform the validation on a large $\sigma_{\phi N}$ obtained in the previous experiment.

In Chap. 2, the SPring-8/LEPS facility, detector system, and electronics are presented. The detail of the analysis is described in Chap. 3. The transparency ratio of ϕ meson are presented and discussed in Chap. 4. Finally, the conclusion is given in Chap. 5.

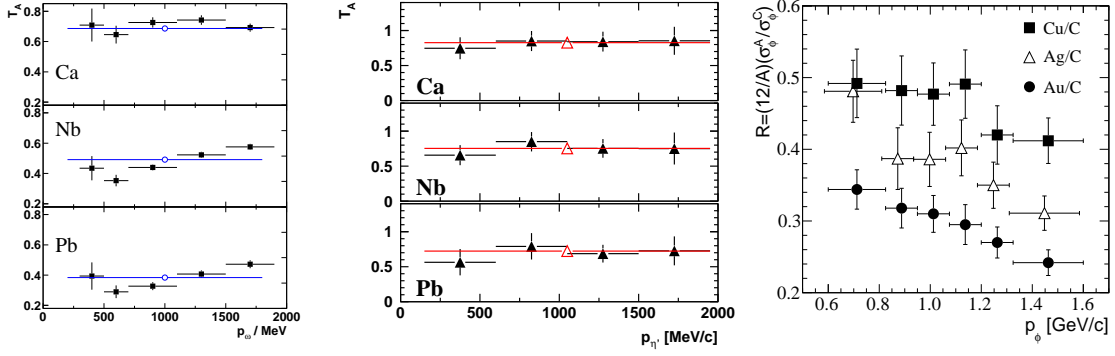


Figure 1.6: Momentum dependence of the transparency ratio for ω (left) [16], η' (center) [17], and ϕ mesons (right) [19].

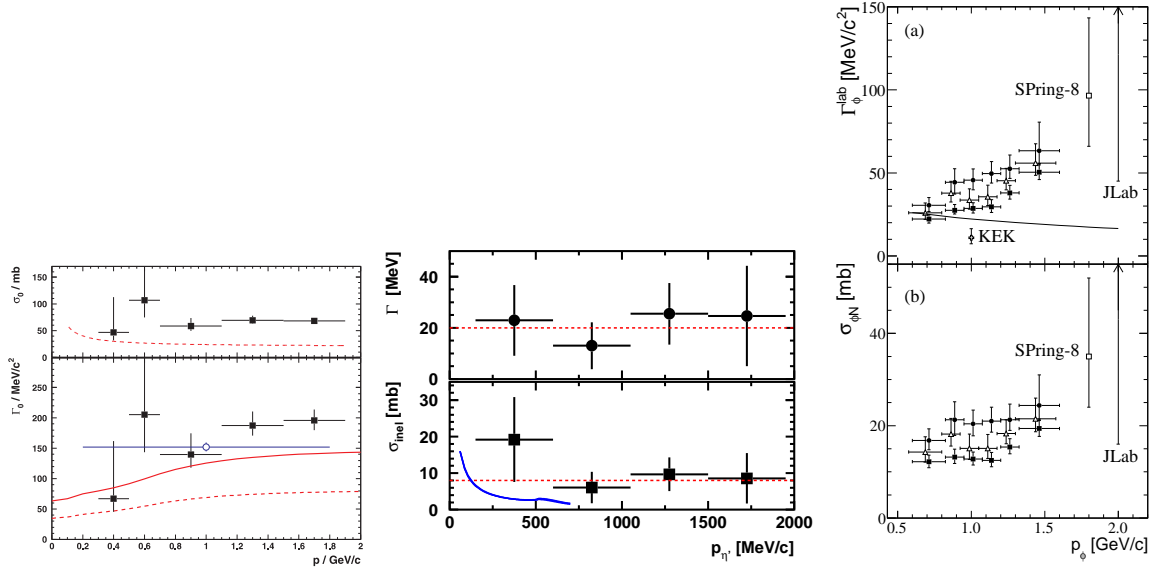


Figure 1.7: In-medium widths and inelastic meson-nucleon cross sections for ω (left) [16], η' (center) [17], and ϕ mesons (right) [19].

Chapter 2

Experiment

The experiment was carried out at the Laser Electron Photon beam line at SPring-8 (LEPS). The SPring-8/LEPS facility provides a linearly polarized photon beam with high intensity and large degree of polarization. The photons with the maximum energy of 2.4 GeV are produced by the backward Compton scattering (BCS) process of laser photons with 8-GeV electrons circulating in the storage ring. The energy of photon beam is measured by a tagging system located in the storage ring. The charged particles produced by photo-reactions are detected with the time projection chamber (TPC) and the LEPS spectrometer system.

The SPring-8/LEPS facility and the experimental apparatus are described in this chapter.

2.1 SPring-8 Facility

SPring-8 (an acronym for Super Photon ring-8 GeV) is a third-generation large-scale synchrotron radiation facility. It was opened in 1997, and located in Harima Science Garden City, Hyogo Prefecture, Japan, as shown in Fig. 2.1.

Third-generation facilities are optimized to use insertion devices, mainly undulators. A large-scale synchrotron radiation facility is generally defined as a facility that has electron energy of more than 5 GeV, and is capable of delivering X-rays from undulators. There are three third-generation large-scale synchrotron radiation facilities in the world today; European Synchrotron Radiation Facility (ESRF) in Grenoble, France, the Advanced Photon Source (APS) near Chicago, USA, and SPring-8 in Japan, accelerating electrons up to 6, 7 and 8 GeV, respectively.

Figure 2.2 shows the aerial view of SPring-8 in September 2011. The SPring-8 accelerator complex is composed of an 1 GeV electron linear accelerator (Linac), an 8 GeV booster synchrotron and an 8 GeV storage ring. The system configuration and main specifications are shown in Fig. 2.3 and in Table 2.1, respectively.

The linac is used as an injector into the booster synchrotron and the NewSUBARU. The electron beam is generated by a 180 kV electron gun. The extracted beam is bunched at a buncher and is accelerated up to 1 GeV with 25 accelerator cavities. Then the beam is transported to the booster synchrotron or to the NewSUBARU storage ring.

The electron beam from the linear accelerator is accelerated up to 8 GeV with the booster synchrotron.



Figure 2.1: Location of SPring-8.



Figure 2.2: Aerial photograph of SPring-8 in September 2011.

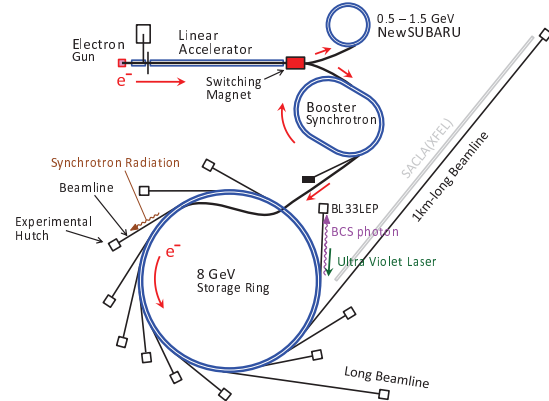


Figure 2.3: Schematic configuration of the SPring-8 accelerator complex.

The circumference of the booster synchrotron is 396.124 m with a racetrack shape, which consists of a FODO lattice of 40 cells. The accelerated 8 GeV beam is extracted and transported to the storage ring. The injection, acceleration and ejection are repeated at the repetition rate of 1 Hz.

The storage ring is a circular accelerator for light sources and its circumference is 1435.95 m long. Electrons are filled in some of the total 2436 bunches with various filling patterns, where the time interval of the successive bunches is 1.966 nsec. The maximum current of the 8 GeV electron beam is 100 mA. The stored electron beam emits synchrotron radiation at bending magnets and at inserted undulators or a wiggler. The emitted radiation is transported through beamlines to hutches in the experimental hall and used for experiments. Totally 62 beam lines can be constructed at this facility. 54 beam lines are operational and 3 beam line are planned or under construction in April 3, 2012.

Table 2.1: Specification of the Linac, the Booster Synchrotron and the Storage Ring of the SPring-8 [23].

Linac	
Electron beam energy	1 GeV
Nominal	1.2 GeV
Max.	
Length	140 m
Number of acceleration cavities	25 excluding ECS
Mode of the cavity	$2\pi / 3$ mode
Peak current/Pulse width	
into the Storage Ring	
Single bunch injection	2 A / 1 ns
Multi-bunch injection	350 mA / 40 ns
into the NewSUBARU	
Single bunch injection	200 mA / 1 ns
Repetition	60 pps (Max.)
RF frequency	2856 MHz
Voltage of electron gun	180 kV

Booster Synchrotron	
Energy	
Injection	0.9~1.15 GeV
Ejection	8 GeV
Circumference	396.124 m
Lattice	FODO
Number of cells / Symmetry	40 cells / 2
Number of bending magnets	64
Number of quadrupole magnets	40 / 40 (Focus / Defocus)
Current	10 mA
Repetition	1~8 pps (1 Hz)
RF frequency	508.58 MHz

Storage Ring	
Energy	< 8 GeV
Circumference	1435.95 m
Current	100 mA
RF frequency	508.6 MHz
Emittance *	3.4 nm-rad / 6.8×10^{-3} nm-rad (Horizontal/Vertical)
Electron beam size (σ) *	3.37×10^{-4} m / 1.16×10^{-5} m (Horizontal/Vertical)
Angular divergence (σ) *	5.55×10^{-5} rad / 1.7×10^{-6} rad (Horizontal/Vertical)
Beam lifetime	> 200 hr / > 15 hr at 1mA (Multi-bunch/Single bunch)
Lattice	Double-Bend Achromat HHLV (High Horizontal Low Vertical beta functions) + 4LSS (Long Straight Sections)
Number of cells	44 cells (33 normal cells + 8 matching cells)
Number of bending magnets	88
Number of quadrupole magnets (per cell)	10 normal cells + 13 matching cells
Energy spread (σ_E/E)	0.11 %

* Average values at the interaction region of the LEPS beam line.

2.2 Overview of LEPS Facility

The LEPS facility is a beam line for quark nuclear physics at SPring-8. The beam line consists of an interaction region of laser photons with circulating electrons, an tagging system, an laser hutch for laser injection, and an experimental hutch. The schematic view of the LEPS beam line is shown in Fig. 2.4.

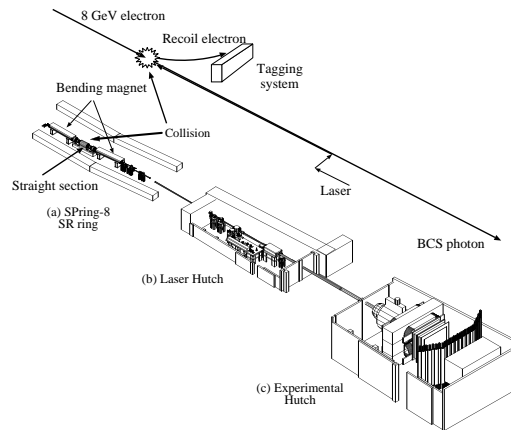


Figure 2.4: Schematic view of the LEPS facility at SPring-8. The facility consists of a laser-electron collision part in the storage ring, a tagging system, a laser hutch for a laser injection, and an experimental hutch. A schematic explanation of the collision between an electron and a laser photon in backward-Compton scattering is inserted in the figure.

Charged particles produced at the target are detected at sideward angle with the time projection chamber (TPC) and at forward angle with the LEPS spectrometer. The TPC is located in an experimental hutch, which sits in a solenoidal magnet and surrounds the nuclear target. The LEPS spectrometer is located at downstream of the TPC, which consists of a dipole magnet, three multi-wire drift chambers (DC1, DC2 and DC3), a plastic scintillator hodoscope (TOF wall), a plastic scintillator (Start Counter) and a silica aerogel Čerenkov counter. The schematic view of the TPC and the LEPS spectrometer in an experimental hutch is shown in Fig. 2.5. The details of the TPC and the LEPS spectrometer are described in Sec. 2.5 and Sec. 2.7, respectively.

The difference in the configuration of experimental apparatuses and the detector acceptances between in the “LEPS standard setup” and in the “TPC experiment setup” for this experiment is shown in Fig. 2.6. In the TPC experiment setup, a TPC surrounding the target for enlarging the detector acceptance was newly installed in 2003. Combined use of this TPC and the existing LEPS spectrometer provided the drastic increase of the detector acceptance.

2.3 Photon Beam

2.3.1 Backward Compton Scattering (BCS)

In this section we discuss the kinematics of the backward-Compton-scattering (BCS) process.

Figure 2.7 shows the kinematical variables in the BCS process. When a laser photon with an energy k_1 collides an electron with a high energy E_e with a relative angle $\theta_1 \simeq 180^\circ$, the photon is scattered

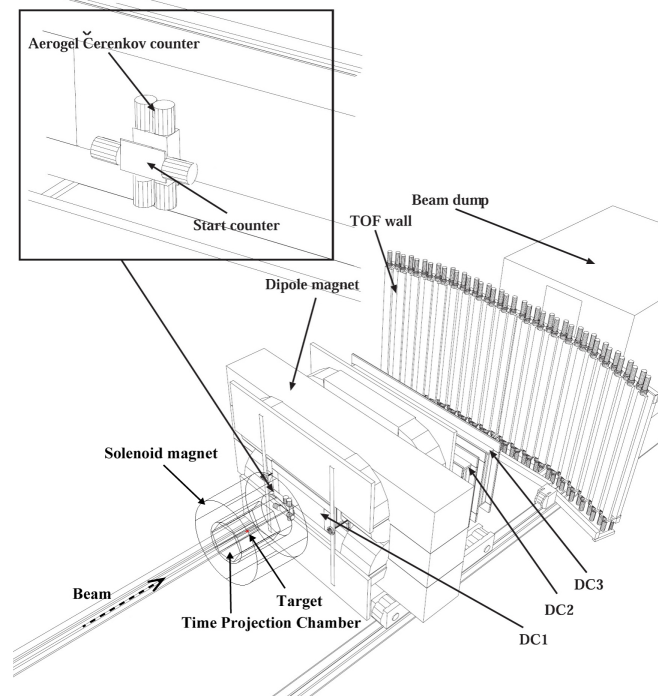


Figure 2.5: Schematic view of the time projection chamber (TPC) and the LEPS spectrometer in an experimental hutch. The TPC sits in a solenoidal magnet, and surrounds the nuclear target. The LEPS spectrometer consists of a dipole magnet, three multi-wire drift chambers (DC1, DC2 and DC3), a plastic scintillator hodoscope (TOF wall), a plastic scintillator (Start Counter) and a silica aerogel Čerenkovcounter.

with a scattering angle of θ_2 . The energy of a BCS photon E_γ is described as

$$E_\gamma = k_1 \frac{1 - \beta \cos \theta_1}{1 - \beta \cos \theta_2 + \frac{k_1(1 - \cos \theta)}{E_e}}, \quad (2.1)$$

where β is an incident electron velocity in unit of the speed of light and $\theta = \theta_2 - \theta_1$. Assuming $\gamma = E_e/m_e \gg 1$, $\beta \approx 1$, $\theta_1 \ll 1$, Eq. 2.1 is rewritten as

$$E_\gamma = \frac{4E_e^2 k_1}{m_e^2 + 4E_e k_1 + \theta_2^2 \gamma^2 m_e^2}, \quad (2.2)$$

where m_e is the electron mass of 0.511 MeV/ c and $\gamma \approx 16000$ at $E_e = 8$ GeV. The maximum energy of a BCS photon (Compton edge) is obtained at $\theta_2 = 0^\circ$:

$$E_\gamma^{max} = \frac{4E_e^2 k_1}{m_e^2 + 4E_e k_1}. \quad (2.3)$$

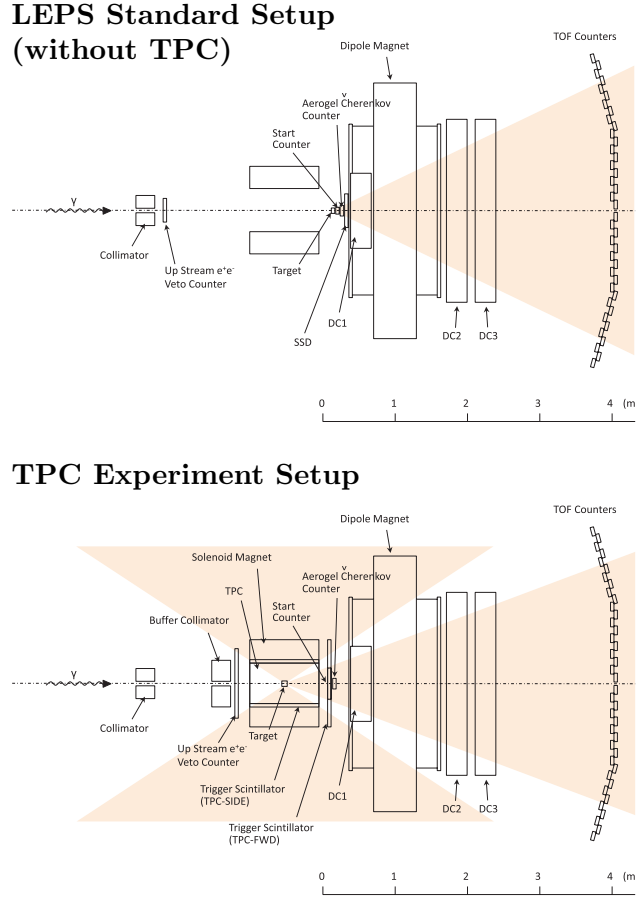


Figure 2.6: Difference in the configuration of experimental apparatuses and the detector acceptances between in the “LEPS standard setup” (top) and in the “TPC experiment setup” for this experiment (bottom). The detector acceptances are shown with the colored areas.

The differential cross section of the BCS process is written as a function of the BCS photon energy:

$$\frac{d\sigma}{dE_\gamma} = \frac{2\pi r_e^2 a}{E_\gamma^{max}} (\chi + 1 + \cos^2\alpha) \quad (2.4)$$

$$a = \frac{m_e^2}{m_e^2 + 4E_e k_1} \quad (2.5)$$

$$\chi = \frac{\rho^2(1-a)^2}{1-\rho(1-a)} \quad (2.6)$$

$$\cos\alpha = \frac{1-\rho(1+a)}{1-\rho(1-a)} \quad (2.7)$$

$$\rho = \frac{E_\gamma}{E_\gamma^{max}} \quad (2.8)$$

where $\gamma_e = 2.818$ fm is the classical electron radius.

The linear polarized BCS photons are made by using linear polarized laser photons. When a laser photon is polarized, the polarization is transferred to a BCS photon. The degree of polarization (P_γ) of

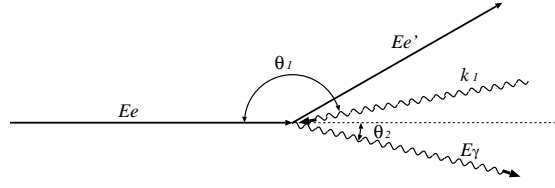


Figure 2.7: Kinematical variables of the backward-Compton-scattering process in the laboratory frame.

a BCS photon is proportional to that of a laser photon (P_{laser}). The linear polarization is given by

$$P_{\gamma} = P_{laser} \frac{(1 - \cos\alpha)^2}{2(\chi + 1 + \cos^2\alpha)}. \quad (2.9)$$

In the present experiment, a linear-polarized photon beam is produced by an Ar laser with a 351 nm wavelength. The differential cross section and the polarization for 275 nm, 351 nm and 488 nm laser are shown in Fig. 2.8.

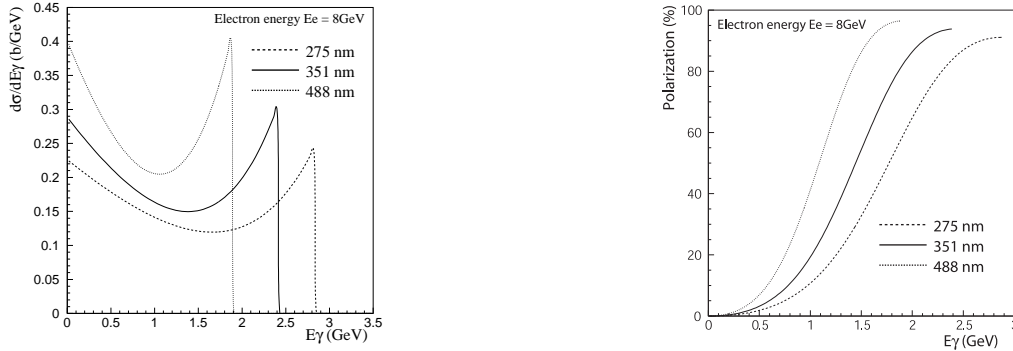


Figure 2.8: The differential cross section of BCS process (left) and the polarization as a function of the photon energy (right).

2.3.2 Laser Injection System

Figure 2.9 shows the laser-operating system placed in the laser hutch. The operating system consists of an Ar laser, a half-wave-length plate ($\lambda/2$ plate), a beam expander, four mirrors and a polarization monitor. The direction, shape, and polarization of laser photons are controlled by this system to achieve high intensity and a high polarization of the γ -ray photon beam. The laser photons pass through the $\lambda/2$ plate to change the direction of the polarization. The shape of the laser beam is tuned by the beam expander. The direction and position of the laser beam are tuned by the third and fourth mirrors. The laser beam is transferred to the beam line by the first and second mirrors. The polarization monitor is placed at the upstream of the collision part in the storage ring to measure laser photons which do not collide with the 8-GeV electrons.

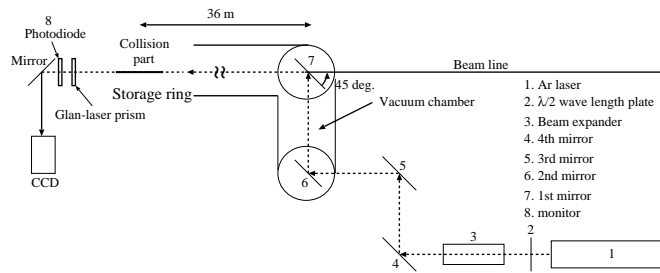


Figure 2.9: Schematic view of the laser operation system.

2.3.3 Photon Energy Tagging System

The energy E_γ of the BCS photon beam is determined by the recoil electron energy $E_{e'}$ as

$$E_\gamma = E_e - E_{e'}. \quad (2.10)$$

The energy of the 8-GeV circulating electron E_e was calculated on the basis of measured field distributions of magnets in the storage ring. The energy was determined as 7.975 ± 0.003 GeV. The energy $E_{e'}$ is measured by a tagging system located in the storage ring. Since an electron scattered by the BCS process loses its energy, it is relatively strongly bent and deviates from the normal orbit in the 8 GeV ring when it passes through the bending magnet placed at the end of the straight section. The tagging system is installed at the exit of the bending magnet to detect the recoil electrons.

A tagging system consists of scintillating fibers (TAG-SF) and plastic scintillator hodoscopes (TAG-PL). Figure 2.10 shows the structure of the tagging system. The tagging system is placed at the outside of a beam vacuum pipe for the 8 GeV electron beam. The tagging system covers a region 4.0–6.6 GeV in the energy of recoil electrons. This energy region corresponds to the energy of the BCS photons 1.4–3.0 GeV.

A hit position of an electron track is measured by the TAG-SF. The TAG-SF consists of two layers (TAG-SFF and TAG-SFB). Each fiber layer consists of 55 fiber bundles. Each fiber bundle is made of six fibers with the cross section of 1×1 mm². Two layers are arranged with an overlap of 0.5 mm to cover the inefficient region of the one layer.

TAG-PL consists of 2 layers of 5 plastic scintillation counters. The size of the plastic scintillator is 10.0 mm high, 7.4 mm wide, and 3.0 mm thick. The plastic scintillator which is closest to the 8 GeV electron beam has the width of 5.5 mm. The plastic scintillators are arranged with an overlap of 2.7 mm.

2.4 Nuclear Targets

We have used the nuclear targets of polyethylene (CH₂), carbon (C), and copper (Cu) in this experiment. Figure 2.11 shows the pictures of the nuclear targets. The diameters of all the targets are 25 mm, and the thicknesses of the targets are set to 0.1 radiation length: 47.0 mm for CH₂, 22.4 mm for C and 1.4 mm for Cu, respectively. The properties of the nuclear targets used in this experiment are summarized in Table 2.2. The data with the C and Cu targets have been used for the measurement of ϕ photo-production. To avoid the systematic errors due to the change of beam conditions, targets are exchanged every around two days.

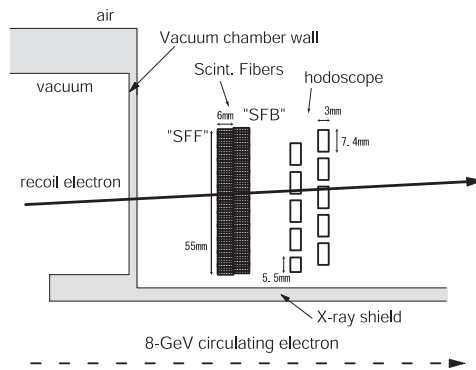
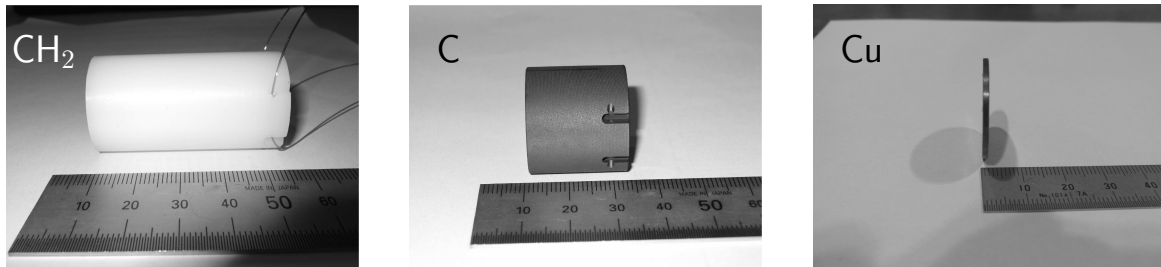


Figure 2.10: Schematic view of the tagging system.

Figure 2.11: Pictures of the nuclear targets: CH_2 (left), C (center), and Cu (right).

2.5 Time Projection Chamber (TPC)

The time projection chamber (TPC) was newly installed to enlarge the detector acceptance of LEPS detector systems in 2003, and has been used to detect the charged particles from ϕ meson photo-production. In this chapter, the basic design of the TPC are described. The general properties, the mechanical design, and the operation of the TPC are described in Appendix A, and the analysis procedure for TPC in Appendix B.

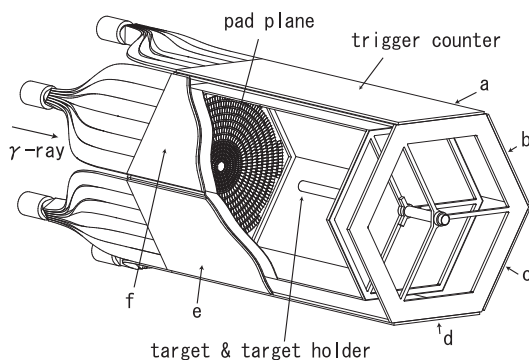


Figure 2.12: Perspective view of the TPC and the side trigger counters. The arrows (from a to f) indicate the side trigger counters.

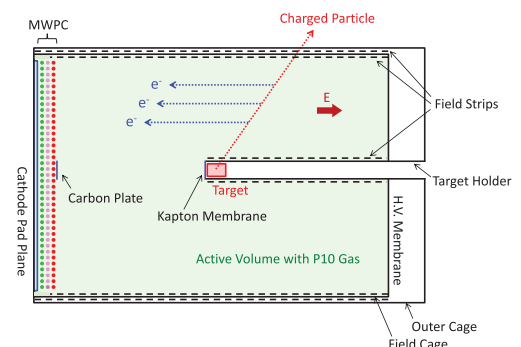


Figure 2.13: Cross sectional side view of the TPC.

A perspective view and a cross sectional side view of a TPC are shown in Fig. 2.12 and Fig. 2.13,

Table 2.2: Properties of the nuclear targets used in this experiment [24].

Target	Atomic Number	Atomic Mass	Diameter [mm]	Thickness [mm]	Radiation Length [%]	Nuclear Collision Length [%]	Nuclear Interaction Length [%]
CH ₂	-	-	25	47.0	10	7.98	5.71
C	6	12.011	25	22.4	10	7.21	4.98
Cu	29	63.546	25	1.4	10	1.53	0.94

respectively. The TPC is located in the center of solenoid magnet and the nuclear target is installed in the TPC. The TPC has a cylindrical active volume of 195 mm in radius and 730 mm in length, and its acceptance covers $20 < \theta < 160$ degrees through the full azimuthal angle, corresponding to 3.76π [sr]. It has been operated with Ar/CH₄ (90:10) gas mixture (P10 gas) at atmospheric pressure, the magnetic field of 2 T, and the electrical field of 18 V/mm. The signals are read through 1055 cathode pads arranged as concentric circles, and provides 14 three-dimensional coordinate measurements and energy-deposition information. The electric field is formed by the high voltage membrane and the field strips embedded on the inner and outer sides of the field cage and on the target holder. The field cage consists of six 1.6 mm thick Grade 10 Garolite (G-10), which is a continuous-woven glass fabric laminate with an epoxy resin. On both side of the plate copper strips of 35 μ m thick and 8 mm wide are embedded. The target holder is a 1mm thick cylinder made of G-10, and is put in the active volume of the TPC. The outer surface of the cylinder is covered with copper strips to form the electric field. The high voltage membrane is made of a copper-coated kapton, and located at the downstream end of the active volume.

2.6 Trigger Counters

The TPC is surrounded by eleven scintillation counters. Six scintillation counters (TPC-SIDE) are put on the sides of the TPC as shown in Fig. 2.12, and the four (TPC-FWD) and the start counter (SC) are placed between the TPC and the LEPS spectrometer (at forward direction of the TPC) as shown in Fig. 2.14 and Fig. 2.15. The logic signals from these counters are used for the trigger logic.

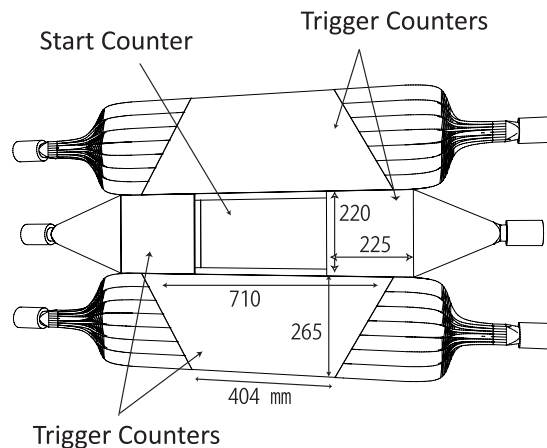


Figure 2.14: Schematic drawing of the forward trigger counters (TPC-FWD). TPC-FWD consists of two trapezoidal scintillation counters and the other two rectangular ones. The start counter (SC) is placed just downstream of the TPC-FWD.

TPC-SIDE and TPC-FWD is set to detect charged particles passing through the active volume of the TPC. The length and thickness of the TPC-SIDE are 880 mm and 1/4 inches, respectively, and the width are 285 mm, 270 mm, 285 mm, 240 mm, 270 mm and 270 mm for the counter a, b, c, d, e and f, respectively (a~f are corresponding to the ones in Fig. 2.12). The PMTs are connected to the upstream side of the plastic scintillators through the twisted light guides. The size of the TPC-FWD are indicated in Fig. 2.14, and the thickness are 5 mm for the rectangular one and 1/4 inches for the trapezoidal one. The rectangular scintillators are viewed by PMTs through the “*fish-tail*” type of light guides, and the trapezoidal ones are viewed by the both side of PMTs through the “*twisted*” light guides.

Figure 2.15 shows a schematic drawing of the SC. The SC is set to detect charged particles which are produced at the target and entered into the LEPS spectrometers, and also used as a reference counter to measure the time-of-flight with the RF signals. The size of the plastic scintillator is 370 mm width, 190 mm high and 5mm thickness. The PMTs are connected to the both side of the plastic scintillator through the fish-tail type of light guides.

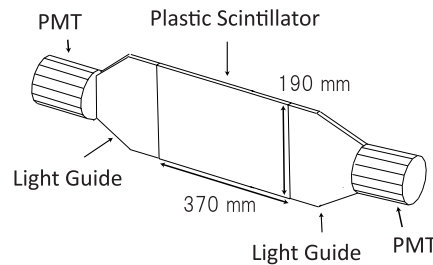


Figure 2.15: Schematic drawing of the start counter (SC).

2.7 LEPS Spectrometer

As shown in Fig. 2.5, the LEPS spectrometer consists of an upstream-veto counter, a silica aerogel Čerenkov counter, three multi-wire drift chambers (DC1, DC2 and DC3), a plastic scintillator hodoscope (TOF wall), and a dipole magnet. The details of each are described in below.

2.7.1 Upstream-Veto Counter

The photon beam is partly converted to e^+e^- pairs until achieving to the target in the air in the beam line, Al windows of the beam pipe or the collimators. These e^+e^- pairs are identified using the upstream veto counter, and vetoed at the trigger level. This counter is a plastic scintillator located at just downstream of the buffer collimator in the experimental hatch. The size is 620 mm high, 620 mm wide, and 3 mm thick. A 2-inch fine-mesh PMT is connected to the plastic scintillator through a light guide.

2.7.2 Silica-Aerogel Čerenkov Counter

A silica-aerogel Čerenkov counter (AC) is used to reject the backgrounds from e^+e^- events at the trigger level. The index of refraction of the silica aerogel radiator used in the present experiment is 1.03. Figure 2.16 shows the relation between momentum and velocity (β) of e^+e^- , pion and Kaon. When a particle with a velocity $\beta > 1/n$ passes through a transparent material with a refractive index n , Čerenkov

lights are emitted. The Čerenkov thresholds for e^+e^- , pion and Kaon are 0.002 GeV/c, 0.57 GeV/c and 2.0 GeV/c, respectively. The signal is used as a veto signal in the trigger logic.

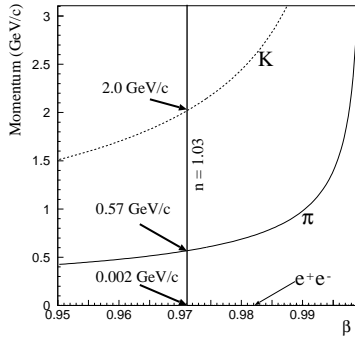


Figure 2.16: Relation between momentum and β for e^+e^- , π and K . A particle with $\beta > 1/n$ emits Čerenkov lights. The line corresponding to an index of 1.03.

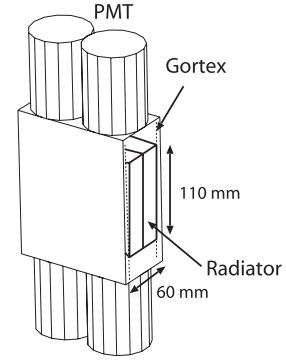


Figure 2.17: Silica aerogel Čerenkov counter (AC).

2.7.3 Drift Chambers

A tracking of a charged particle is performed by drift chambers. DC1 is located upstream of the dipole magnet. It has the active area of 600 mm \times 300 mm. Figure 2.18 shows a drawing of field, shield and sense wires. DC1 has 6 planes, x1, x2, u1, u2, v and x3. The x3 wires are made additionally because a charged particle begins to be spread out by the magnetic field in DC1. Sense wires of x1-x2 and u1-u2 are positioned with a 6 mm spacing and wires of x3 and v are positioned with a 12 mm spacing. The field wires are arranged in a hexagonal shape. The shield wires are positioned along the windows to shape the electric field. The inclination angle of the u and v wires is 45° with respect to the horizontal plane.

DC2 and DC3 are installed downstream of the dipole magnet and have the active area of 2000 mm \times 800 mm. Both DC2 and DC3 have 5 planes, x1, x2, u1, u2 and v. The design of DC2 and DC3 is the same as DC1, but there is no x3 wires in DC2 and DC3. Sense wires of x1-x2 and u1-u2 are positioned with a 10 mm spacing, and the wires of v are positioned with a 20 mm spacing. The u and v direction are inclined by 30° with respect to the vertical plane.

The material of the sense wires is gold-plated tungsten (Au-W) and the wire diameter is 25 and 30 μm for DC1 and DC2, DC3, respectively. The field and shield wires are made of Au-BeCu with a diameter of 100 μm . The windows are made of mylar with a thickness of 125 μm . The design parameters of the DC's are shown in Table 2.3. The gas mixture used to operate the DC's is Ar/CH₄ (70:30). The efficiency is more than 98% and is typically 99%.

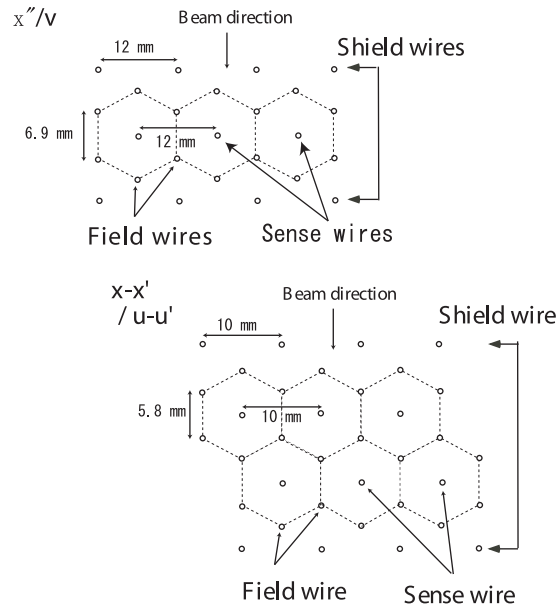


Figure 2.18: Schematic drawing of the wire configuration in the drift chambers.

Table 2.3: Design parameters of the DC's. The location of the center of each DC along the z-axis is measured from the center of the dipole magnet.

	Plane	Orientation	# of sense wires	Wire spacing (mm)	Active area $x \times y$ (mm ²)	Location z (mm)
DC1	x-x'	0°	48×2	6	600 × 300	-466.0
	u-u'	+45°	48×2	6		
	v	-45°	48	12		
	x''	0°	48	12		
DC2	x-x'	0°	104×2	10	2000 × 800	860.5
	u-u'	+30°	78×2	10		
	v	-30°	79	20		
DC3	x-x'	0°	104×2	10	2000 × 800	1260.5
	u-u'	+30°	78×2	10		
	v	-30°	79	20		

2.7.4 TOF Wall

The TOF wall is placed downstream of the DC3, and the time-of-flights of charged particles are measured by a TOF wall. Figure 2.19 shows a schematic view of the TOF wall and drawing of a TOF counter. The TOF wall consists of 40 plastic scintillator bars with the size of 200 cm long, 12 cm wide, and 4 cm thick. Two 2-inch PMT's are attached to both sides through a light guide. Each bar is overlapped with adjacent bars by 1 cm. Sideway bars are aligned in the planes tilted by ± 15 degrees. The z-position of the TOF wall is set at 3151.5 mm away from the center of the dipole magnet.

2.7.5 Dipole Magnet

A dipole magnet is used as a momentum analyzer magnet to bend charged particles. The magnet is placed at the center of the LEPS spectrometer. The magnet has an aperture with 550 mm high and

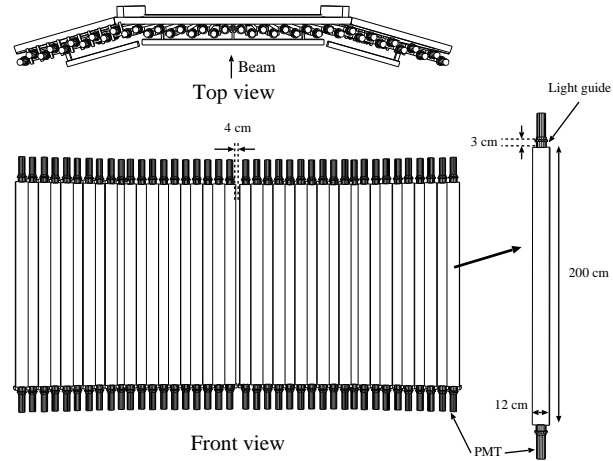


Figure 2.19: Drawing of the TOF wall.

1350 mm wide. The length of the pole along the beam is 600 mm. Fig. 2.20 shows the distribution of the

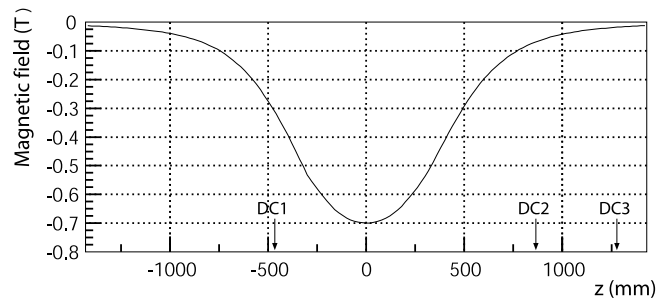


Figure 2.20: Distribution of the magnetic field B_y as a function of the z -position at $x=0$ and $y=0$. The position of $z=0$ corresponds to the center of the dipole magnet.

magnetic field B_y along the y -direction as a function of the z -axis at $x=0$ and $y=0$. We used the TOSCA simulation program to obtain the distribution. The direction of the magnetic field is from down to up. The current is set at 800 A, and the strength of the magnetic field is 0.7 T at the center.

2.8 Data Acquisition

The trigger signal is made using the signals from the tagging system (TAG), upstream-veto counter (UP), aerogel Čerenkov counter (AC), TOF counters, TPC-SIDE counters and TPC-FWD counters. The trigger signals for each detector subsystem are described below, and the logic diagram is shown in Fig. 2.21.

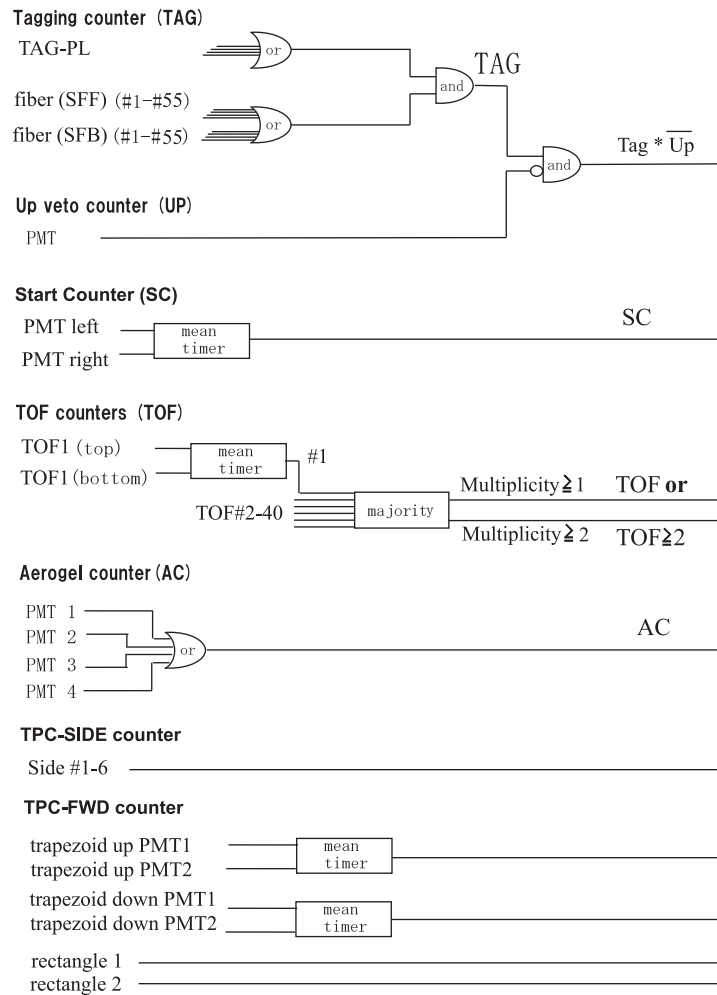


Figure 2.21: Diagram of the readout circuits for triggers.

TAG In the tagging system, OR signals from the scintillation fibers are made in each layer (TAG-SFF and TAG-SFB) and TAG-PL hodoscope. Then the AND signal of them are used in the trigger logic.

UP The logic signal from the upstream-veto counter is used as a veto signal. The width of the veto signal is set to be 75 nsec.

SC The coincidence signal from both PMT's of the SC is used in the trigger logic. The coincidence signal supplies the common start and stop in the TDC modules. The width of the coincidence signal is set 25 nsec.

AC The OR signal from four PMT's of the AC is used to make a veto signal for a trigger logic. The width of the veto signal is set 75 nsec.

TOF In the TOF system, the mean timing of the logic signals from the two PMT's of a TOF counter is made by a mean timer module (CAMAC C561). The signal from the mean timer module is read

by the majority logic unit module 4532 (CAMAC). The signals of the multiplicity ≥ 1 or ≥ 2 are used in the trigger logic.

TPC-SIDE, TPC-FWD All of counters except for two trapezoidal counters of the TPC-FWD are viewed by one PMT, and the logic signal is used for the trigger. The trapezoidal counters of the TPC-FWD are viewed by two PMT's, and the mean timing of the the signals are used for the trigger logic. The logic signal from the trigger counters for the TPC is read by the majority logic unit module.

Three trigger conditions are used for the data taking. The trigger(a) is for events in which at least three counters are fired, called as “three charge trigger”. The trigger(b) is for events in which at least two counters are fired, called as “two charge trigger”. And the trigger(c) is for events with two charged particles in the LEPS spectrometer and at least one particle hitting the TPC-SIDE counter.

The trigger logics are written as

$$\begin{aligned} \text{Trigger(a)} &= \text{TAG} \otimes \overline{\text{UP}} \otimes \overline{\text{AC}} \otimes (\text{TPC-SIDE} + \text{TPC-FWD} + \text{SC} \otimes \text{TOF}) \geq 3 \\ \text{Trigger(b)} &= \text{TAG} \otimes \overline{\text{UP}} \otimes \overline{\text{AC}} \otimes (\text{TPC-SIDE} + \text{TPC-FWD} + \text{SC} \otimes \text{TOF}) \geq 2 \\ \text{Trigger(c)} &= \text{TAG} \otimes \overline{\text{UP}} \otimes \overline{\text{AC}} \otimes (\text{TPC-SIDE} \geq 1) \otimes \text{SC} \otimes (\text{TOF} \geq 2), \end{aligned}$$

where “ \otimes ” represents the AND logic, and the “+” represents the OR logic. The logic diagrams are shown in Fig. 2.22. Because the rate of the trigger(b) is too high to read out the data of the TPC, the trigger(b) is scaled down by a factor of 2~3. In the study of ϕ production by $\gamma p \rightarrow \phi p \rightarrow K^+ K^- p$ reaction, three charged particles are produced in the final state. Thus, the trigger(a) is used as the main trigger for the data taking. For the analysis of the ϕ photo-production, the data taken with the trigger(a) is used.

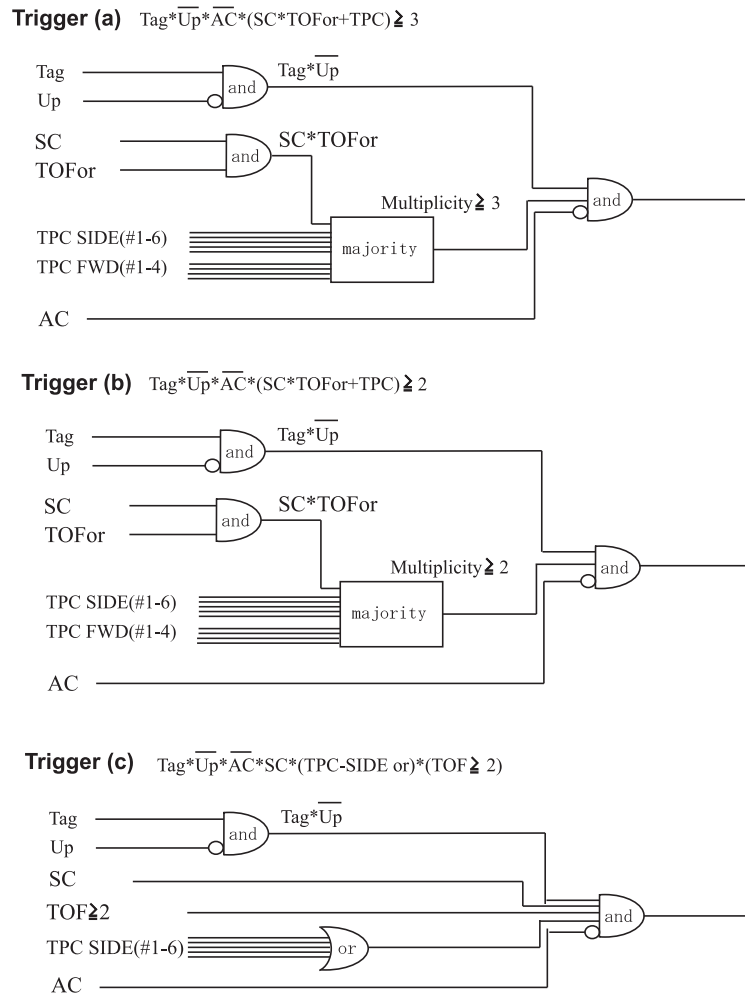


Figure 2.22: Diagram of the readout circuits for triggers.

2.9 Coordinate System

A common coordinate system is used throughout LEPS. The center of the dipole magnet is defined as the origin of the coordinate system. The z -axis runs along the beam line, and the $+z$ direction is defined as the direction of photon-beam flux. The x - y plane is perpendicular to the z -axis. Looking $+z$ direction, the $+x$ -axis points to the left side, and the $+y$ -axis points upward. “Upstream” and “Downstream” mean the $-z$ and $+z$ directions, respectively.

The coordinates are often described also in polar coordinate system. The r is defined as the distance from the z -axis, the azimuthal angle ϕ is defined as angle measured clockwise from the $+x$ -axis around the z -axis, and the polar angle θ is defined as the angle from the $+z$ -axis.

Chapter 3

Analysis

3.1 Outline of Data Analysis

Data described in this thesis has been taken from September to December in 2004, with C and Cu targets and linearly polarized photon beams. The total number of beam photons on the targets and the total number of trigger-accepted events in this period are summarized in Table 3.1. The total number of beam photons is obtained by the number of tagger trigger with the dead time correction and the transmission ratio of beam photons from the collision point to the target (0.526).

Table 3.1: The total number of beam photons and trigger-accepted events

	C	Cu
Number of beam photons on target (Vert./Hori.)	$2.79 \times 10^{11} / 2.60 \times 10^{11}$	$3.33 \times 10^{11} / 3.30 \times 10^{11}$
Number of trigger-accepted events (Vert./Hori.)	$2.79 \times 10^7 / 2.63 \times 10^7$	$1.59 \times 10^7 / 1.66 \times 10^7$

The details of the reconstruction framework of the TPC are described in Appendix B. Various cuts used for the selection of $\phi \rightarrow K^+K^-$ events are described in Sec. 3.2. Extraction of the yield of ϕ mesons determined from the K^+K^- invariant mass distribution is described in Sec. 3.3.

3.2 Event Selection for the $\phi \rightarrow K^+K^-$ events

In this section, various cuts used for the selection of $\phi \rightarrow K^+K^-$ events are discussed. Before that, we describe definitions of some notations at first. In this analysis, we have been detected three particles K^+K^-p using the TPC and the LEPS spectrometer as shown in Fig. 3.1. We classify the event category according to the combination of which particles are detected in which detectors. The notations are as follows:

- *tpcK⁺K⁻P* mode
 K^+ , K^- , and proton are detected in TPC
- *tpcK⁺K⁻spP* mode
 K^+ and K^- are detected in the TPC
proton are detected in the LEPS spectrometer
- *tpcK⁺PspK⁻* mode
 K^+ and proton are detected in the TPC
 K^- is detected in the LEPS spectrometer

- $tpcK^-PspK^+$ mode
 K^- and proton are detected in the TPC
 K^+ is detected in the LEPS spectrometer
- $tpcK^\pm PspK^\mp$ mode
Combination of $tpcK^+PspK^-$ and $tpcK^-PspK^+$ mode

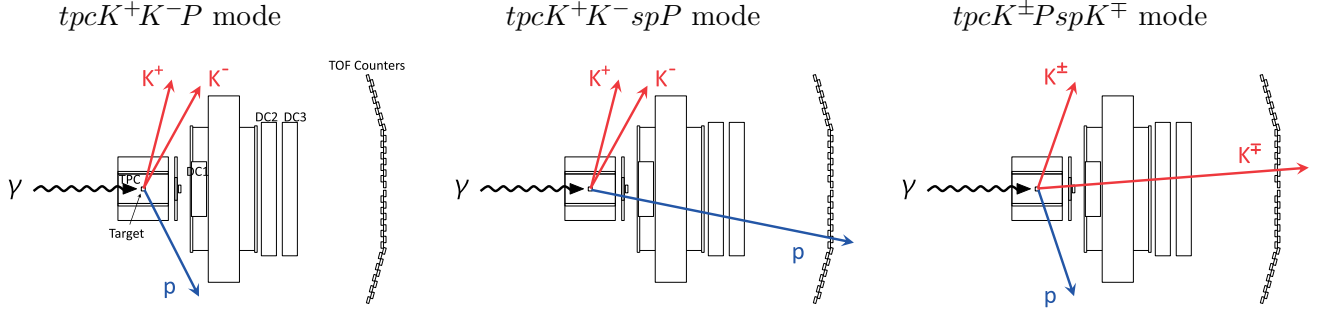


Figure 3.1: Notations for the each detection mode.

3.2.1 Tagging Counter

The energy of photon beam is measured with the tagging counter. The tagger cut is used to select the good track of the recoil electron by the backward-Compton scattering process in the tagging system. Figure 3.2 shows the distributions of the number of reconstructed tracks in the tagging counter ($ntag$) for the C and Cu target. When the $ntag$ is equal to one, the track is used.

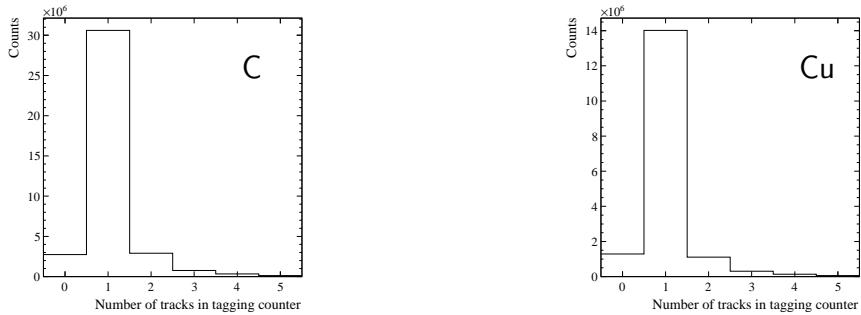


Figure 3.2: Distributions of the number of tracks in the tagging counter ($ntag$) for the C (left) and Cu (right) target run.

Figure 3.3 shows the distributions of the incident beam photon energy (E_γ) for the C and Cu target. We require that the E_γ is smaller than 2.5 GeV because events with E_γ greater than 2.5 GeV are background due to X-rays and electro-magnetic showers.

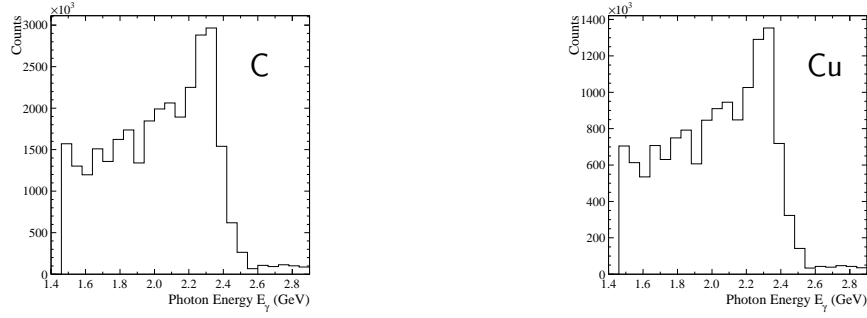


Figure 3.3: Distributions of the incident beam photon energy (E_γ) for the C (left) and Cu (right) target run.

3.2.2 Number of Good Tracks

To select the reaction $\gamma p \rightarrow K^+ K^- p$, the detection of K^+ , K^- , and proton are required. A pre-selection cut using the number of good tracks is applied as follow:

- $tpcK^+K^-P$ mode
Number of good tracks in TPC ≥ 3
- $tpcK^+K^-spP$ mode and $tpcK^\pm PspK^\mp$ mode
Number of good tracks in TPC ≥ 2
Number of good tracks in the LEPS spectrometer ≥ 1

here, the good tracks are required the high probability of χ^2 for track fitting. The probability of χ^2 for track fitting is used to select good tracks, to reject the background events in TPC, and to reject the decay-in-flight tracks in the LEPS spectrometers. The probability of χ^2 is defined as

$$Prob(\chi^2, ndf) = \int_{\chi^2}^{\infty} f(\chi'^2, ndf) d\chi'^2 \quad (3.1)$$

where f is the standard χ^2 distribution with the number of degree of freedom ndf . Figure 3.4 and Fig. 3.5 show the distributions of the number of good tracks in the TPC and the LEPS spectrometer, respectively. Figure 3.6 and Fig. 3.7 show the distributions of the probability of χ^2 for track fitting in TPC and the LEPS spectrometer, respectively. The probability of χ^2 is required to be larger than 0.02.

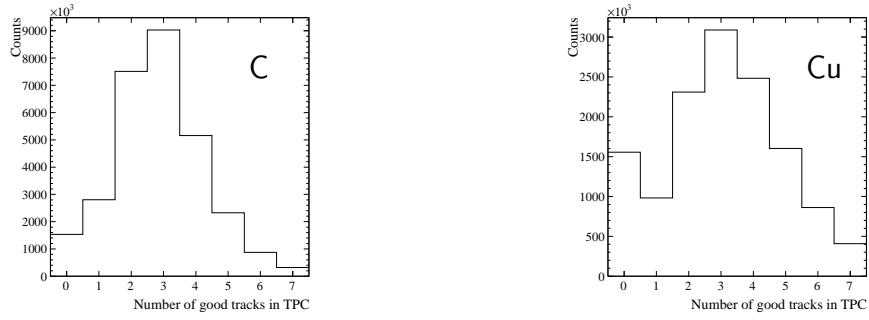


Figure 3.4: Distributions of the number of good tracks in the TPC for the C (left) and Cu (right) target run.

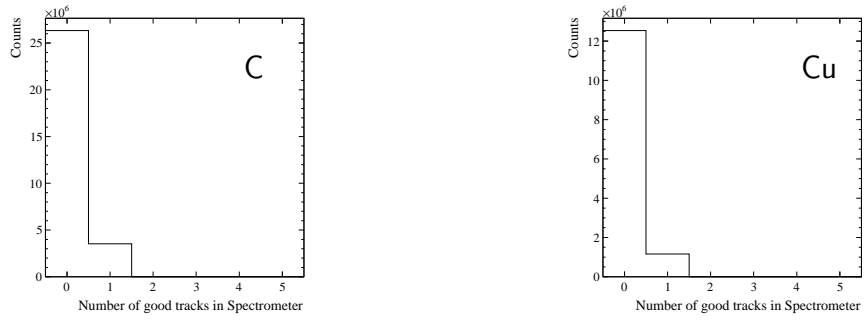


Figure 3.5: Distributions of the number of good tracks in the LEPS spectrometer for the C (left) and Cu (right) target run.

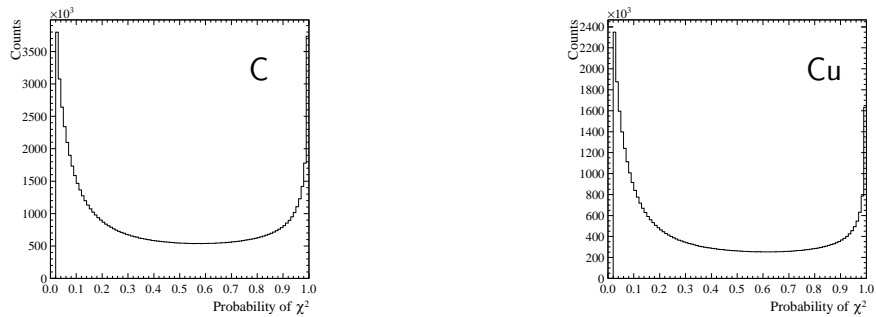


Figure 3.6: Distribution of the probability of χ^2 for track fitting in the TPC for the C (left) and Cu (right) target run.

3.2.3 Particle Identification (PID)

PID with the TPC

The optimal selection boundary of dE/dx for Kaon PID is set where the ratio $\delta N_\phi/N_\phi$ is minimized. Here, N_ϕ is the yield of ϕ mesons and δN_ϕ is the error of N_ϕ . The selection boundary of dE/dx for Kaon

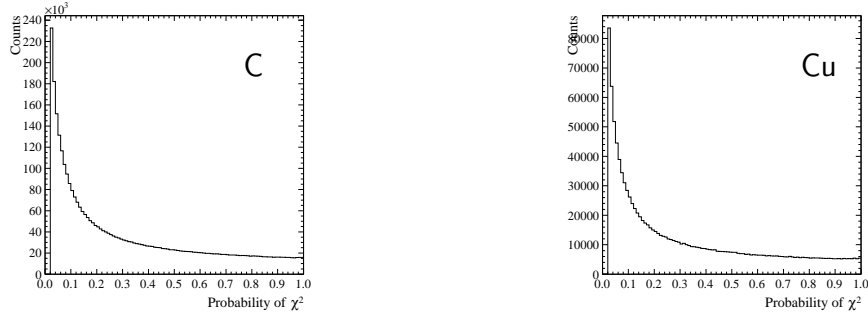


Figure 3.7: Distribution of the probability of χ^2 of track fitting in the LEPS spectrometer for the C (left) and Cu (right) target run.

in the TPC is defined as 1.5σ of dE/dx resolution for the $tpcK^+K^-P$ and $tpcK^+K^-spP$ mode whereas 2σ for the $tpcK^\pm PspK^\mp$ mode. The selection boundary of dE/dx for proton in the TPC is defined as 4σ for all the modes. The details of the study for PID with the TPC are described in Appendix B.6.

PID with the LEPS Spectrometer

The mass square of a charged particle (M^2) is obtained as

$$M^2 = p^2 \frac{(1 - \beta^2)}{\beta^2}, \quad (3.2)$$

$$\beta = \frac{L}{cT}, \quad (3.3)$$

where p is the momentum of particle, L is the path length of the particle trajectory, and c is the speed of light. T is the time-of-flight where the RF signal is used to determine a start timing. The resolution of the squared mass (σ_{M^2}) is represented as

$$\sigma_{M^2}^2 = 4M^4 \left(\frac{\sigma_p}{p}\right)^2 + 4c^2 p^2 (p^2 + M^2) \left(\frac{\sigma_{TOF}}{L_{typ}}\right)^2, \quad (3.4)$$

where L_{typ} is set to the typical path length (4100 mm). The σ_p is the resolution of momentum and described as

$$\left(\frac{\sigma_p}{p}\right)^2 = \left(\frac{a_1}{\beta}\right)^2 + p^2 a_2^2, \quad (3.5)$$

where a_1 term represents the effect of the multiple scattering and a_2 term represents the spatial resolutions of the drift chambers. a_1 and a_2 are estimated as 0.0087 and 0.0042, respectively, by Monte Carlo calculation. The σ_{TOF} is the resolution of TOF measurement and determined as 0.13 by real data.

The kaon and proton identification regions are shown in Figure 3.8. The selection boundaries for kaon and proton are defined as 4σ used with momentum dependent mass resolution in Eq. 3.4, and the additional cut is set on the squared mass from 0.15 to 0.55 $(\text{GeV}/c^2)^2$ for kaon.

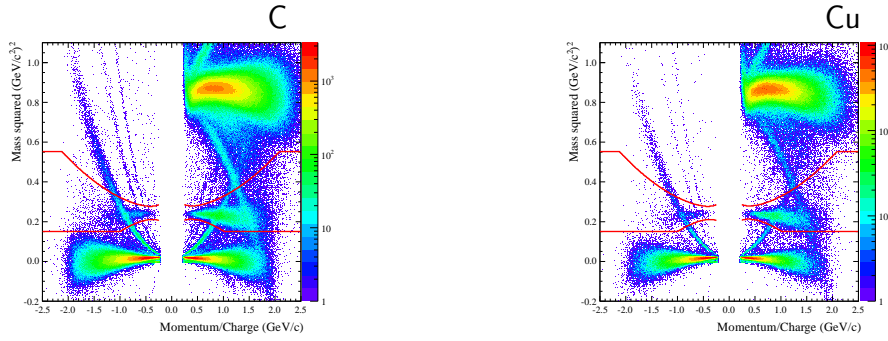


Figure 3.8: Correlation between the momentum/charge and the square of mass reconstructed by the LEPS spectrometer for C (left), and Cu (right) target, after the number of good tracks cut is applied. The red lines indicate the boundaries for the K^+ and K^- selection.

3.2.4 Distance of Closest Approach (DCA) Cut

In the $\phi \rightarrow K^+K^-$ decay process, a K^+ and a K^- have the same vertex where the ϕ meson decays. Therefore, the distance of closest approach (DCA) of a K^+ and a K^- from the decayed ϕ meson should be zero, ideally. However, the calculated DCA from the tracking information is not always zero due to the detector resolution and the multiple scattering effect. The distributions of the DCA between the K^+

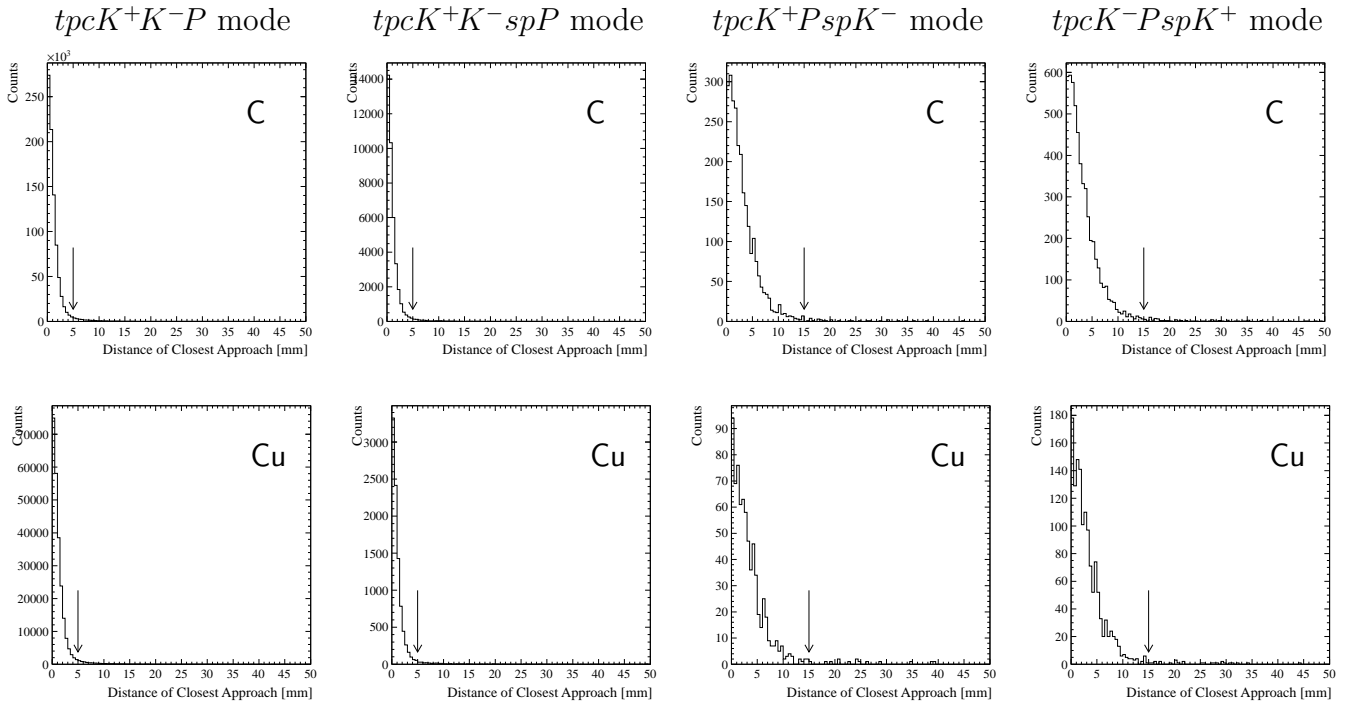


Figure 3.9: The distribution of the DCA between the K^+ and the K^- tracks. Arrows indicate selection regions.

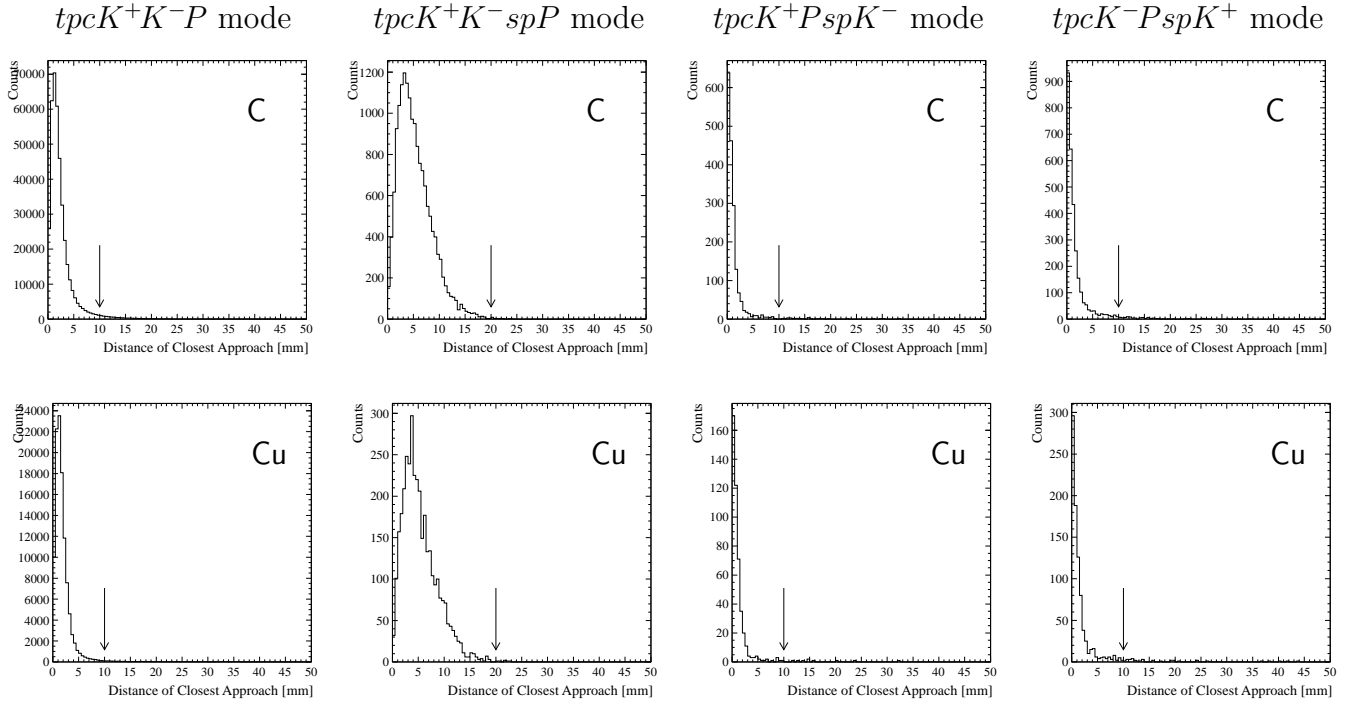


Figure 3.10: The distribution of the DCA between the proton track and K^+K^- vertex. Arrows indicate selection regions.

and the K^- tracks are shown in Fig. 3.9. The same for between the proton track and the K^+K^- vertex are shown in Fig. 3.10. Arrows in the figures indicate selection regions. Selection regions are estimated using the Monte Carlo simulation as listed below:

- $tpcK^+K^-P$ mode

$$\text{DCA between } K^+ \text{ and } K^- \leq 5 \text{ mm} \quad (3.6)$$

$$\text{DCA between proton and } K^+K^- \text{ vertex} \leq 10 \text{ mm} \quad (3.7)$$

- $tpcK^+K^-spP$ mode

$$\text{DCA between } K^+ \text{ and } K^- \leq 5 \text{ mm} \quad (3.8)$$

$$\text{DCA between proton and } K^+K^- \text{ vertex} \leq 20 \text{ mm} \quad (3.9)$$

- $tpcK^\pm PspK^\mp$ mode

$$\text{DCA between } K^+ \text{ and } K^- \leq 15 \text{ mm} \quad (3.10)$$

$$\text{DCA between proton and } K^+K^- \text{ vertex} \leq 10 \text{ mm} \quad (3.11)$$

Here, we counted any combination of all candidate tracks for kaon.

3.2.5 Vertex

The vertex for the K^+K^- pair should be inside the target material if the detector resolution is negligible because the life time of ϕ meson is very short (46.2 fm). In order to select events from targets, vertex cuts in the $x-y$ plane and in the z -coordinate are required.

Cut in the $x-y$ plane

The reconstructed vertex distributions for the K^+K^- in the $x-y$ plane are shown in Fig. 3.11. We

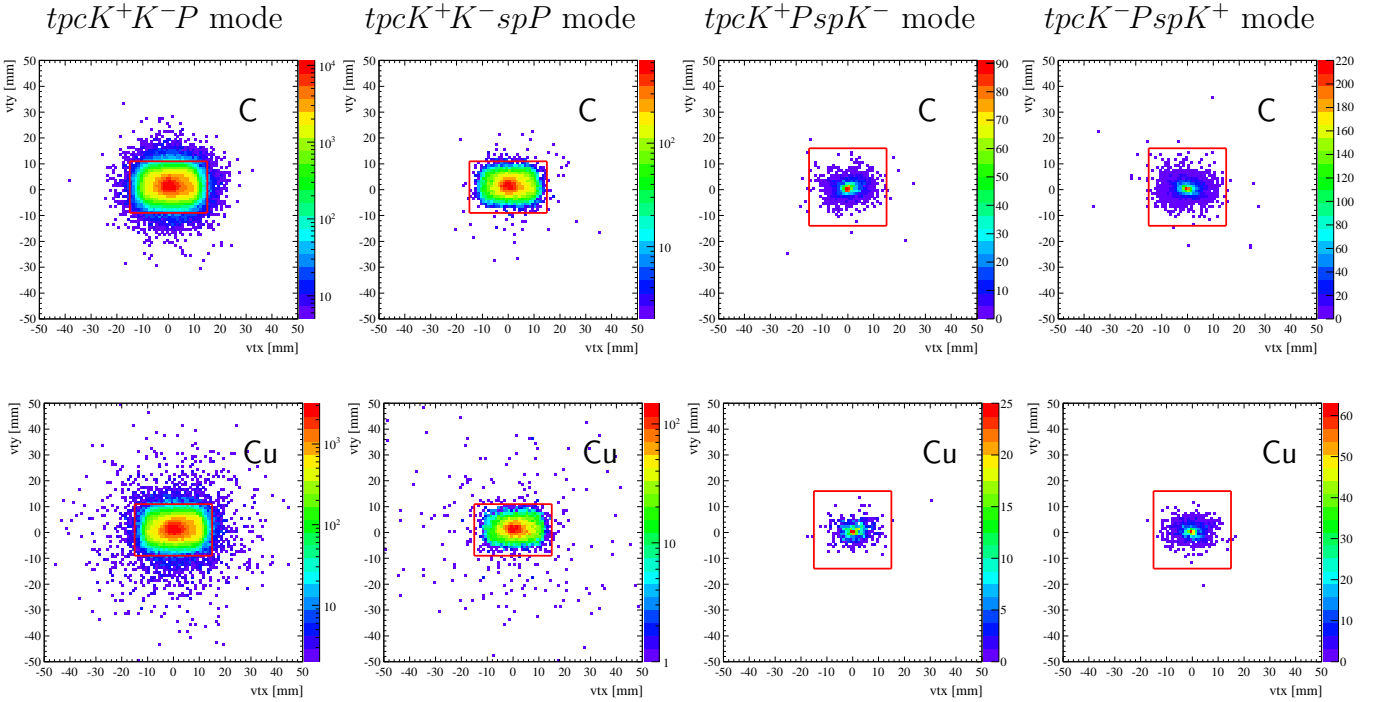


Figure 3.11: Vertex distribution for the K^+K^- in the $x-y$ plane. The rectangles indicate the selection regions for the vertex cuts in the $x-y$ plane.

requires the vertex to be inside the rectangles shown in Fig. 3.11, which is required as

- $tpcK^+K^-P$ and $tpcK^+K^-spP$ mode

$$-15 < vtx < 15 \text{ mm}, \quad -9 < vty < 11 \text{ mm} \quad (3.12)$$

- $tpcK^\pm PspK^\mp$ mode

$$-15 < vtx < 15 \text{ mm}, \quad -14 < vty < 16 \text{ mm} \quad (3.13)$$

in $x-y$ plane.

Cut in the z -coordinate

We have used the nuclear targets of CH_2 , C and Cu in this experiment. To avoid the systematic errors due to the change of beam conditions, targets are exchanged every around two days. Each time targets are exchanged, the position of installed target could be shifted along the target holder (along the z -axis) within the accuracy of alignment. Figure 3.12 (left) and (right) show the z -positions of the C and Cu

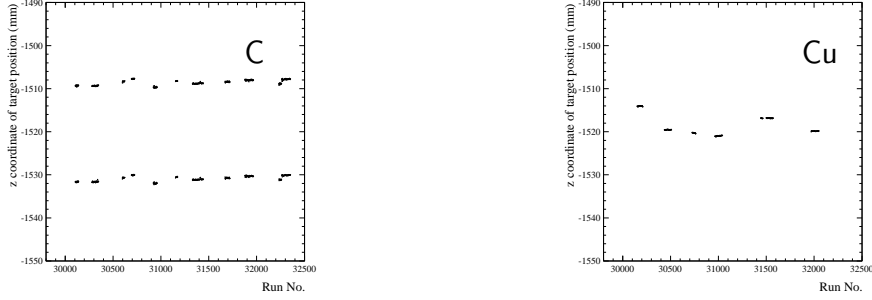


Figure 3.12: Position of the Target. In the figure for C target (left), the data points show the z -coordinates of the upstream and the downstream edge of the C target. In the figure for Cu target (right), the data points show the z -coordinates of the center of Cu target.

target as a function of the *run-Number*, respectively. The C target had the 22.4 mm thickness, and the data points in figure show the z -coordinates of the upstream and the downstream edge of the C target evaluated by fitting the z -vertex distribution with a Gaussian convoluted step function. The Cu target had the 1.4 mm thickness, and the data points in figure show the z -coordinates of the center of Cu target evaluated by fitting the z -vertex distribution with a Gaussian function.

Figure 3.13 shows the distributions of the z -vertex (vtz) of K^+K^- pair after the vertex selection cut in x - y plane. The origins in figure are the center of targets. To select the K^+K^- pair from the target, the vertex cuts of vtz are required as

- $tpcK^+K^-P$ and $tpcK^+K^-spP$ mode
 - $-14 < vtz - \text{center of target} < 14 \text{ mm}$ for C
 - $-10 < vtz - \text{center of target} < 10 \text{ mm}$ for Cu

$$(3.14)$$

- $tpcK^\pm PspK^\mp$ mode
 - $-30 < vtz - \text{center of target} < 30 \text{ mm}$ for C
 - $-25 < vtz - \text{center of target} < 25 \text{ mm}$ for Cu.

$$(3.15)$$

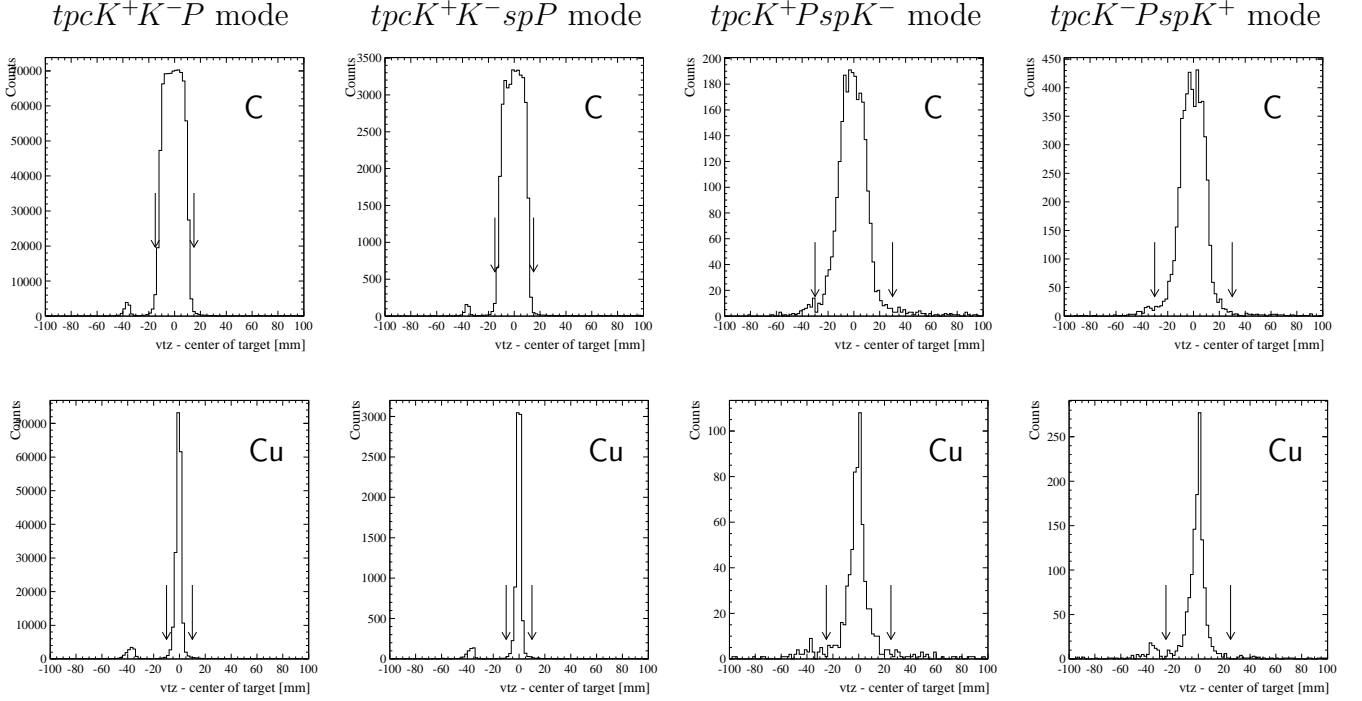


Figure 3.13: Distributions of the z -vertex (vtz) of K^+K^- pair after the vertex selection cut in x - y plane. The origins are the center of targets. The arrows indicate the selection regions.

3.2.6 Missing Mass

We have been applied the missing mass cut to select the $\gamma N \rightarrow \phi N$ quasi-free incoherent production, though the coherent process is suppressed due to the heavy mass of the ϕ meson near the threshold of ϕ photo-production. Under the assumption that the target is a proton at rest, the missing mass for the reaction $\gamma p \rightarrow K^+K^-X$ ($MM(K^+K^-)$) is given by

$$MM^2(K^+K^-) = \left(E_\gamma + m_p - \sqrt{m_{K^+}^2 + p_{K^+}^2} - \sqrt{m_{K^-}^2 + p_{K^-}^2} \right)^2 - (p_\gamma - p_{K^+} - p_{K^-})^2, \quad (3.16)$$

where E_γ is the energy of beam photon, m_{K^\pm} (m_p) stand for the kaon (proton) mass, and p_{K^\pm} are the measured K^\pm momenta with the energy loss correction. Figure 3.14 shows the distributions of $MM^2(K^+K^-)$. The arrows indicate the selection regions, which requires below conditions:

- $tpcK^+K^-P$ and $tpcK^+K^-spP$ mode

$$0. \leq MM^2(K^+K^-) \leq 1.4 \text{ (GeV}/c^2)^2 \quad (3.17)$$

- $tpcK^\pm PspK^\mp$ mode

$$0.4 \leq MM^2(K^+K^-) \leq 1.5 \text{ (GeV}/c^2)^2 \quad (3.18)$$

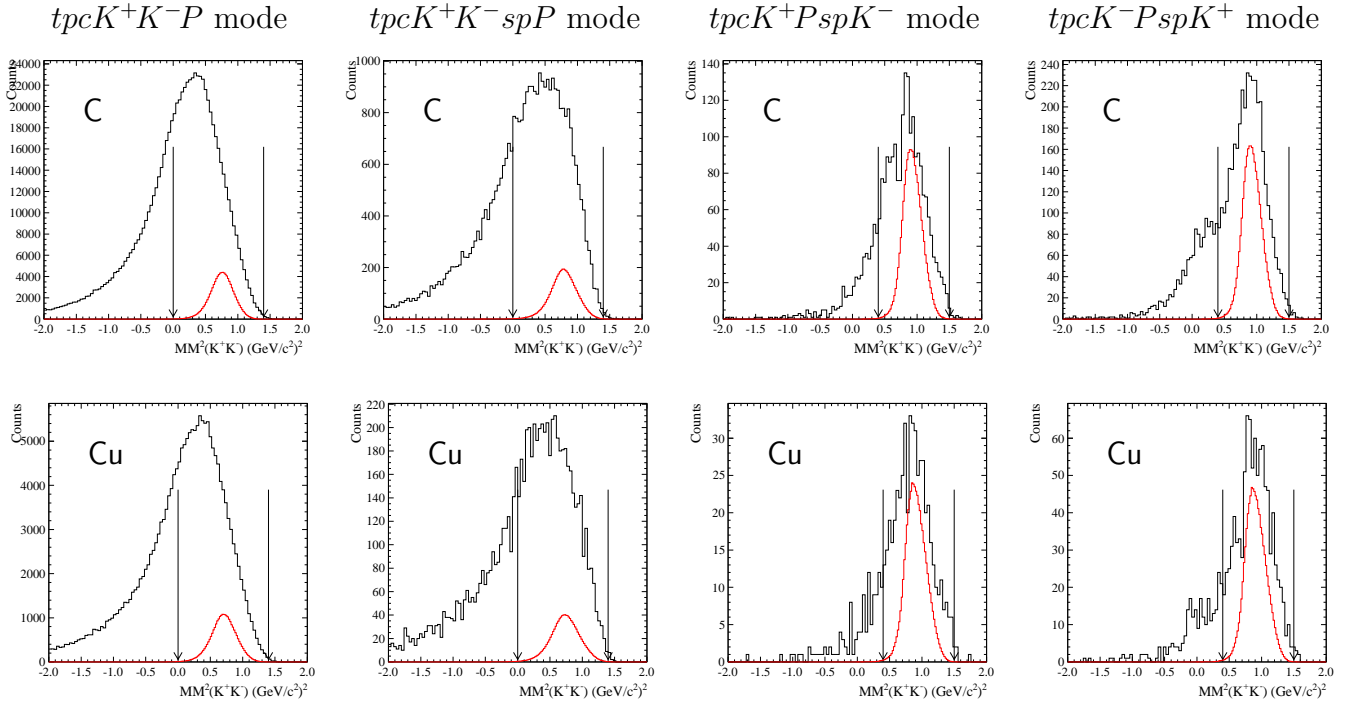


Figure 3.14: Distributions of the square of the missing mass for the reaction $\gamma p \rightarrow K^+ K^- X$ ($MM^2(K^+ K^-)$). The black(red) histogram represents the observed(simulated) data. The scaling of simulated data is determined arbitrarily. The arrows indicate the selection regions.

3.2.7 Summary of Selection Cuts

The number of events after the various cuts discussed above are summarized in Table 3.2 ~ 3.6. Table 3.2 shows the summary of trigger and tagging counter cuts in all detection modes. Table 3.3 ~ 3.6 show the summaries of ϕ selection cuts in $tpcK^+K^-P$, $tpcK^+K^-spP$, $tpcK^+PspK^-$ and $tpcK^+PspK^-$ mode, respectively. Here, the rejection factor is defined as

$$\text{Rejection factor} = \frac{\text{The number of events before the cut}}{\text{The number of events after the cut}}$$

and is noted in bracket in each Tables.

Table 3.2: Summary of Trigger and Tagging counter cuts in all detection modes.

Cut	C	Cu
Trigger		
3 charge trigger	3.76×10^7	1.69×10^7
Tagging counter		
1 recoil electron	3.06×10^7 (1.23)	1.40×10^7 (1.21)
$E_\gamma < 2.5$ GeV	2.99×10^7 (1.02)	1.37×10^7 (1.02)

Table 3.3: Summary of ϕ selection cuts in $tpcK^+K^-P$ mode.

Cut	C		Cu	
Preselection				
Number of good-tracks in TPC ≥ 3	1.80×10^7	(1.66)	8.85×10^6	(1.55)
K^+K^- selection				
K^+K^- selection in TPC	8.19×10^5	(22.0)	2.27×10^5	(39.1)
DCA between K^+ and K^- *	8.28×10^5	(0.986)	2.28×10^5	(0.992)
x - y vertex	8.12×10^5	(1.02)	2.23×10^5	(1.02)
z vertex	7.76×10^5	(1.05)	1.94×10^5	(1.15)
Missing mass	4.83×10^5	(1.60)	1.16×10^5	(1.67)
Proton selection				
Proton selection in TPC	3.34×10^5	(1.45)	8.32×10^4	(1.39)
DCA between proton and K^+K^- vertex	3.26×10^5	(1.02)	8.24×10^4	(1.01)

* We counted any combination of all candidate tracks.

Table 3.4: Summary of ϕ selection cuts in $tpcK^+K^-spP$ mode.

Cut	C		Cu	
Preselection				
Number of good-tracks in the LEPS spectrometer ≥ 1	3.52×10^6	(8.47)	1.16×10^6	(11.8)
Number of good-tracks in the TPC ≥ 2	2.69×10^6	(1.31)	9.20×10^5	(1.27)
K^+K^- selection				
K^+K^- selection in the TPC	3.90×10^4	(68.9)	9.25×10^3	(99.5)
DCA between K^+ and K^- *	3.81×10^4	(1.02)	9.03×10^3	(1.02)
x - y vertex	3.73×10^4	(1.02)	8.81×10^3	(1.02)
z vertex	3.61×10^4	(1.03)	7.89×10^3	(1.12)
Missing mass	2.34×10^4	(1.54)	5.01×10^3	(1.57)
Proton selection				
Proton selection in the LEPS spectrometer	1.62×10^4	(1.44)	3.50×10^3	(1.43)
DCA between proton and K^+K^- vertex	1.62×10^4	(1.00)	3.50×10^3	(1.00)

* We counted any combination of all candidate tracks.

Table 3.5: Summary of ϕ selection cuts in $tpcK^+PspK^-$ mode.

Cut	C		Cu	
Preselection				
Number of good-tracks in the LEPS spectrometer ≥ 1	3.52×10^6	(8.47)	1.16×10^6	(11.8)
Number of good-tracks in the TPC ≥ 2	2.69×10^6	(1.31)	9.20×10^5	(1.27)
K^+K^- selection				
K^- selection in the LEPS spectrometer	6.87×10^3	(392)	1.85×10^3	(498)
K^+ selection in the TPC	2.51×10^3	(2.74)	6.96×10^2	(2.65)
DCA between K^+ and K^- *	2.58×10^3	(0.974)	7.23×10^2	(0.963)
x - y vertex	2.57×10^3	(1.00)	7.22×10^2	(1.00)
z vertex	2.44×10^3	(1.05)	6.32×10^2	(1.14)
Missing mass	1.97×10^3	(1.24)	5.07×10^2	(1.25)
Proton selection				
Proton selection in TPC	1.60×10^3	(1.23)	4.04×10^2	(1.25)
DCA between proton and K^+K^- vertex	1.58×10^3	(1.01)	3.97×10^2	(1.02)

* We counted any combination of all candidate tracks.

Table 3.6: Summary of ϕ selection cuts in $tpcK^-PspK^+$ mode.

Cut	C		Cu	
Preselection				
Number of good-tracks in the LEPS spectrometer ≥ 1	3.52×10^6	(8.47)	1.16×10^6	(11.8)
Number of good-tracks in the TPC ≥ 2	2.69×10^6	(1.31)	9.20×10^5	(1.27)
K^+K^- selection				
K^+ selection in the LEPS spectrometer	4.36×10^4	(61.7)	1.43×10^4	(64.2)
K^- selection in TPC	5.31×10^3	(8.21)	1.40×10^3	(10.3)
DCA between K^+ and K^- *	5.26×10^3	(1.01)	1.38×10^3	(1.02)
x - y vertex	5.25×10^3	(1.00)	1.37×10^3	(1.00)
z vertex	5.06×10^3	(1.04)	1.23×10^3	(1.12)
Missing mass	3.69×10^3	(1.37)	9.59×10^2	(1.28)
Proton selection				
Proton selection in TPC	2.62×10^3	(1.41)	7.24×10^2	(1.32)
DCA between proton and K^+K^- vertex	2.55×10^3	(1.03)	7.00×10^2	(1.03)

* We counted any combination of all candidate tracks.

3.3 Yield of ϕ meson

The yield of ϕ mesons is obtained from the K^+K^- invariant mass distribution. The K^+K^- invariant mass ($M(K^+K^-)$) is given by

$$M^2(K^+K^-) = \left(\sqrt{m_{K^+}^2 + p_{K^+}^2} + \sqrt{m_{K^-}^2 + p_{K^-}^2} \right)^2 - |p_{K^+} + p_{K^-}|^2 \quad (3.19)$$

where m_{K^+} and m_{K^-} stand for the kaon mass, and p_{K^+} and p_{K^-} are the measured K^+ and K^- momenta with the energy loss correction, respectively. The invariant mass spectra of the final K^+K^- sample for the C and Cu targets in the $tpcK^+K^-P$, $tpcK^+K^-spP$, and $tpcK^\pm PspK^\mp$ mode are shown in Fig. 3.15. Here, we combined two data sets (the $tpcK^+PspK^-$ and $tpcK^-PspK^+$ modes) into the one (the $tpcK^\pm spK^\mp$ mode) because of the low statistics of each yields of ϕ meson in the $tpcK^+PspK^-$ and $tpcK^-PspK^+$ modes. Each K^+K^- sample are divided into the two kinematical regions of the laboratory momentum of ϕ meson (p_ϕ). The $tpcK^+K^-P$ and $tpcK^+K^-spP$ mode are divided into $p_\phi = 0.3-0.6$ and $0.6-0.8$ GeV/ c , and the $tpcK^\pm spK^\mp$ mode is divided into $0.6-1.3$ and $1.3-2.0$ GeV/ c . In the $tpcK^+K^-P$ and $tpcK^+K^-spP$ mode, we used only K^+K^- sample with $p_\phi < 0.8$ GeV/ c for the better K/π separation. We fitted each mass spectrum with the resonance shape of $\phi \rightarrow K^+K^-$ determined by the Monte Carlo simulation and a 2nd-order polynomial as a background in the mass region from $2m_{K^\pm}(0.987)$ to 1.2 GeV/ c^2 . Fits are performed by using the maximum likelihood method. To examine the quality of the fit, the likelihood chi-square χ_λ^2 , which is defined in Ref. [25] as

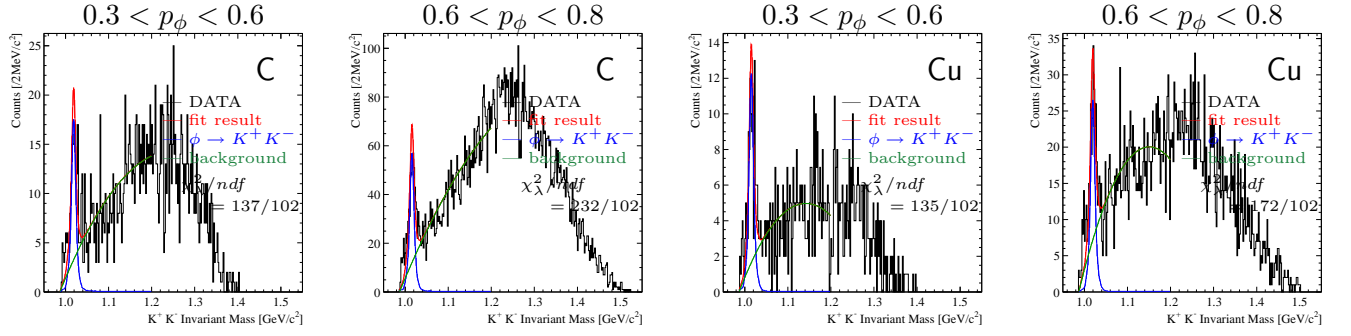
$$\chi_\lambda^2 = 2 \sum_i (y_i - n_i + n_i \ln(n_i/y_i)) \quad (3.20)$$

where n_i is the number of events in the i -th bin and y_i is the number of events predicted by the fit, is calculated. The calculated χ_λ^2 divided by the number of degrees of freedom are shown in each figure. The yields of ϕ meson in each detection mode and kinematical region are summarized in Table 3.7.

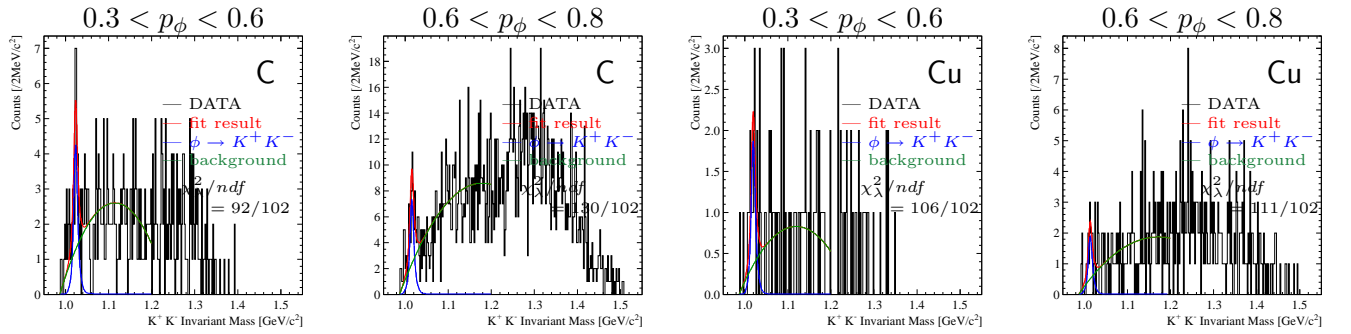
Table 3.7: The measured yields of ϕ meson.

Detection Mode	p_ϕ [GeV/ c]	C	Cu
$tpcK^+K^-P$	0.3 – 0.6	125 ± 14	87 ± 11
	0.6 – 0.8	405 ± 26	188 ± 17
$tpcK^+K^-spP$	0.3 – 0.6	28 ± 7	13 ± 4
	0.6 – 0.8	48 ± 9	13 ± 5
$tpcK^\pm PspK^\mp$	0.6 – 1.3	178 ± 16	49 ± 9
	1.3 – 2.0	250 ± 21	41 ± 10

tpcK⁺K⁻P mode



tpcK⁺K⁻spP mode



tpcK[±]PspK[∓] mode

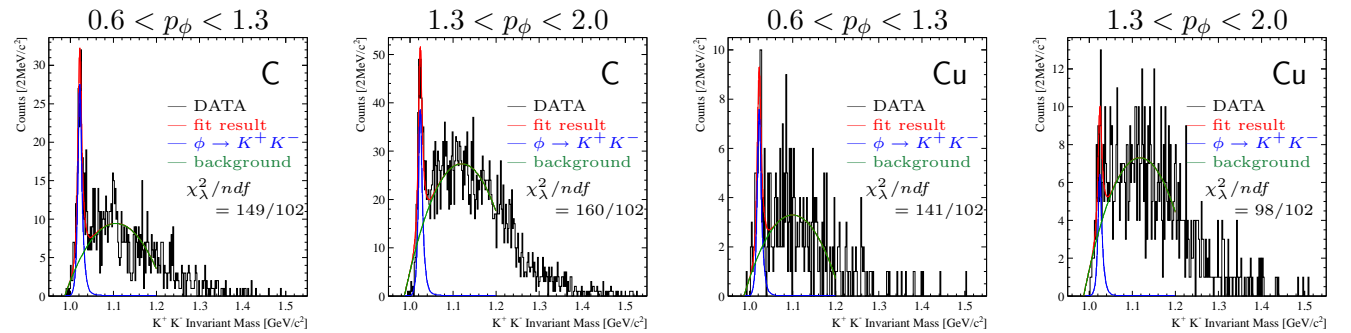


Figure 3.15: The invariant mass spectra of the final K^+K^- sample in the *tpcK⁺K⁻P* (top), *tpcK⁺K⁻spP* (center), and *tpcK[±]PspK[∓]* mode (bottom). The black, red, green, and blue lines represent the data, the fit results, the backgrounds, and the expected $\phi \rightarrow K^+K^-$ shapes, respectively.

Chapter 4

Results and Discussions

4.1 Transparency Ratio T

The transparency ratio T for ϕ mesons is defined as

$$T = \frac{R_{Cu}^\phi/A_{Cu}}{R_C^\phi/A_C}, \quad (4.1)$$

where $A_C = 12.011$ and $A_{Cu} = 63.546$ are the mass numbers of C and Cu nuclei. R_C^ϕ and R_{Cu}^ϕ are the production rates for the incoherent ϕ photo-production on C and Cu nuclei, respectively. The basic ideas of the transparency ratio is described in Chap. 1.

The production rate for the incoherent ϕ photo-production on the nucleus is written for each nucleus A as

$$R_A^\phi = \frac{N_A^\phi}{N_A^{beam} N_A^{nuclei} \eta_A^{att} \eta_A^{geo} BR}, \quad (4.2)$$

where the variables denote as follows:

- N^ϕ : Number of observed ϕ mesons,
- N^{beam} : Number of beam photons on target,
- N^{nuclei} : Number of target nuclei in a unit area,
- η^{att} : Attenuation factor of the photon flux in the target material,
- η^{geo} : Geometrical acceptance,
- BR : Branching ratio of the $\phi \rightarrow K^+ K^-$ process (0.489 ± 0.005 [20]),

Hence, the Eq. 4.1 is rewrite as

$$T = \frac{N_{Cu}^\phi}{N_C^\phi} \cdot \frac{A_C}{A_{Cu}} \cdot \frac{N_C^{beam}}{N_{Cu}^{beam}} \cdot \frac{N_C^{nuclei}}{N_{Cu}^{nuclei}} \cdot \frac{\eta_C^{att}}{\eta_{Cu}^{att}} \cdot \frac{\eta_C^{geo}}{\eta_{Cu}^{geo}}. \quad (4.3)$$

The values of N_C^ϕ and N_{Cu}^ϕ are given in Table 3.7. In the rest of this section, we describe how to estimate the other terms. Most of systematic errors such as the detector acceptances, detector inefficiencies, and analysis inefficiencies are canceled by taking the ratio.

Difference in the Number of Beam Photons

The N_C^{beam} and N_{Cu}^{beam} are determined by summing the numbers of beam photons with vertically and horizontally polarization. The detail of the number of beam photons on the target is given in Table 3.1. The ratio of N_C^{beam}/N_{Cu}^{beam} is 0.813.

Difference in the Number of Target Nuclei

The number of target nuclei in a unit area is calculated as

$$\begin{aligned} & \text{The number of target nuclei in a unit area [cm}^{-2}\text{]} \\ &= \frac{\xi \text{ [cm]} \times \rho \text{ [g/cm}^3\text{]}}{A \text{ [g/mol]}} \times N_A \text{ [mol}^{-1}\text{]} \end{aligned} \quad (4.4)$$

where A , ξ , and ρ are the mass number, the thickness, and the density, respectively. $N_A = 6.02214129(27) \times 10^{23}$ [mol⁻¹] stands for the Avogadro constant. Table 4.1 shows the properties of nuclear targets used in this experiment. The ratio of $N_C^{nuclei}/N_{Cu}^{nuclei}$ is 18.1. and A_C/A_{Cu} is 5.29.

Table 4.1: Properties of nuclear targets used in this experiment.

Target	C	Cu
Mass number A	12.011	63.546
Thickness ξ [cm]	2.24	0.14
Density ρ [g/cm ³]	1.90	8.92
Number of nuclei in a unit area [cm ⁻²]	2.13×10^{23}	1.18×10^{22}

Difference in Attenuation of the Photon Flux

The photon flux is attenuated during passing through the material. The attenuation of the photon flux is described as

$$N_\gamma/N_\gamma^0 = \exp\{-(\mu/\rho)x\}, \quad (4.5)$$

where N_γ^0 is a incident photon flux, N_γ is a photon flux emerged after penetrating a layer of material, x is a travel distance defined as mass per a unit area, and ρ is a material density. The Eq. 4.5 is rewritten as

$$\mu/\rho = x^{-1} \ln(N_\gamma^0/N_\gamma). \quad (4.6)$$

μ/ρ is determined from measured values of N_γ^0 , N_γ , and x , experimentally, and called as the mass attenuation coefficient [26]. Here, we adopt the dimensionless variable x_0 , which is defined as $x_0 \equiv (\mu/\rho)x_{targ}$ where x_{targ} is the target thickness as mass per a unit area. x_0 stands for the target thickness in the unit length through which the photon intensity becomes $1/e$.

The averaged photon flux in the target is obtained by multiplying the photon flux by the attenuation factor in the target (η_{att}). The η_{att} is described as

$$\eta_{att} = \frac{1}{x_0} \int_0^{x_0} \exp(-t) dt = \frac{1}{x_0} \{1 - \exp(-x_0)\}. \quad (4.7)$$

Table 4.2 shows the summary of the mass attenuation coefficient μ/ρ , the thickness x_0 , and the averaged attenuation factor η_{att} , where the mass attenuation coefficients μ/ρ are set the values at $E_\gamma = 2$ GeV. The ratio of $\eta_C^{att}/\eta_{Cu}^{att}$ is 0.999.

Table 4.2: Attenuation of the photon flux in the target.

Target	C	Cu
Mass attenuation coefficient μ/ρ [cm ² /g]	1.74×10^{-2}	5.83×10^{-2}
Thickness x_0	0.0741	0.0728
Attenuation factor η_{att}	0.964	0.964

Difference in Geometrical Acceptance

The geometrical acceptance is estimated using the Monte Carlo simulation as

$$\eta_{geo} = \frac{\text{The number of observed } \phi \text{ mesons}}{\text{The number of generated } \phi \text{ mesons}}, \quad (4.8)$$

and summarized in Table 4.3. In the simulation, ϕ mesons are generated with a flat phase space distribution and with the mass distribution forced to have the Breit-Wigner. The generated ϕ mesons are forced to decay into K^+K^- . The daughter particles are traced in the detector simulation using GEANT3 [27]. The angular distribution of the ϕ mesons decay into K^+K^- is considered to be isotropic.

By taking the ratio of the η_C^{geo} to η_{Cu}^{geo} , the contributions from detector acceptances, the detector inefficiencies, and the analysis inefficiency are canceled out. The remaining contribution is mainly from the difference in the attenuation of charged particles in each target material. The detail of this contribution is discussed in Appendix C.

Table 4.3: Geometrical acceptance

Detection Mode	p_ϕ [GeV/c]	Acceptance		
		η_C^{geo}	η_{Cu}^{geo}	$\eta_C^{geo}/\eta_{Cu}^{geo}$
$tpcK^+K^-P$	0.3 – 0.6	$(1.57 \pm 0.02) \times 10^{-3}$	$(3.25 \pm 0.04) \times 10^{-3}$	0.483 ± 0.009
	0.6 – 0.8	$(1.79 \pm 0.01) \times 10^{-2}$	$(3.17 \pm 0.01) \times 10^{-2}$	0.565 ± 0.002
$tpcK^+K^-spP$	0.3 – 0.6	$(6.37 \pm 0.01) \times 10^{-2}$	$(9.51 \pm 0.02) \times 10^{-2}$	0.670 ± 0.002
	0.6 – 0.8	$(4.97 \pm 0.01) \times 10^{-2}$	$(5.61 \pm 0.01) \times 10^{-2}$	0.887 ± 0.002
$tpcK^\pm PspK^\mp$	0.6 – 1.3	$(8.25 \pm 0.02) \times 10^{-3}$	$(8.68 \pm 0.02) \times 10^{-3}$	0.950 ± 0.003
	1.3 – 2.0	$(3.59 \pm 0.01) \times 10^{-2}$	$(3.60 \pm 0.01) \times 10^{-2}$	0.998 ± 0.003

Transparency Ratio T

The transparency ratio T for ϕ mesons is derived from Eq. 4.3 with above results, and are summarized in Table 4.4. Figure 4.1 shows the transparency ratio T as a function of the ϕ meson laboratory momentum. The results in this experiment are shown with closed blacks. Here, we combines two data sets ($tpcK^+K^-P$ and $tpcK^+K^-spP$ modes) into the one in weighted average method because of its low statistics. The result in the previous experiment [15], extracted only from C and Cu data, is superimposed in the same plot with open circle. The horizontal dots and bars represent the mean and the RMS value of the ϕ momentum in each kinematical bin. The vertical error bars show statistical errors only. The systematic uncertainty arises from the evaluation of the number of ϕ meson is estimated as $\sim 7\%$ by varying the fit parameters, the range of fitting, and the order of the polynomial background. The systematic effects arise from the run dependence of the target position is estimated as $\sim 1\%$ using Monte Carlo calculation, the ϕ meson emission angle dependence for the transparency ratio as $\sim 5\%$ discussed in Appendix E, and the trigger caused by the inelastic scattering of the emitted nucleon as $\sim 10\%$ discussed in Appendix D.

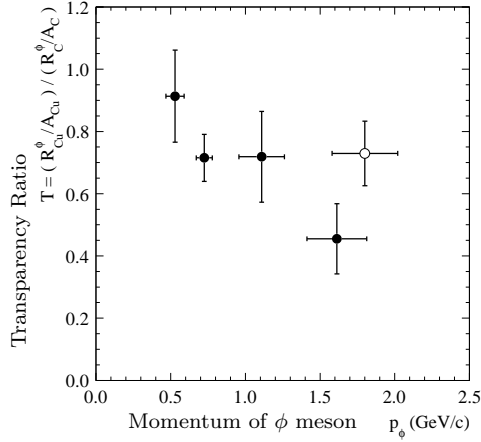


Figure 4.1: Transparency ratio T for ϕ mesons on Cu target normalized to the C target, as a function of the ϕ momentum. The closed black points represent the result in this experiment. The open circle represents the result in the previous experiment, extracted only from C and Cu data.

Table 4.4: The measured transparency ratio T

Detection Mode	p_ϕ [GeV/c]	T
$tpcK^+K^-P$	0.3 – 0.6	0.93 ± 0.16
	0.6 – 0.8	0.72 ± 0.08
$tpcK^+K^-spP$	0.3 – 0.6	0.84 ± 0.36
	0.6 – 0.8	0.64 ± 0.27
Weighted average of $tpcK^+K^-P$ and $tpcK^+K^-spP$	0.3 – 0.6	0.91 ± 0.15
	0.6 – 0.8	0.72 ± 0.08
$tpcK^\pm PspK^\mp$	0.6 – 1.3	0.72 ± 0.15
	1.3 – 2.0	0.45 ± 0.11

4.2 Discussion

We have confirmed that the transparency ratio decreases with ϕ momentum, which is the same tendency as the result of COSY/ANKE collaboration [19].

We have performed the validation on the momentum dependence of $\sigma_{\phi N}$. In order to extract $\sigma_{\phi N}$ from the transparency ratio, an optical model of a Glauber multiple scattering theory has been applied. The detail of this procedure is discussed in Appendix E.1. When the ϕ mesons decay inside the nucleus, the K^+K^- invariant mass spectrum might be strongly distorted by the K^-N or the K^+N interaction. Therefore we assumed that a ϕ meson was lost if it decayed inside nuclei. The data obtained from this experiment is used for the following calculations. First, on the assumption that $\sigma_{\phi N}$ is a constant (, independent of p_ϕ), $\sigma_{\phi N}$ is estimated to be $21.7^{+8.7}_{-6.2}$ mb, which agrees with the result in previous experiment within the statistical errors. Next, on the assumption that $\sigma_{\phi N}$ increases as p_ϕ , the proportionality constant is estimated to be $23.9^{+9.7}_{-6.9}$ mb/(GeV/c), which derives $\sigma_{\phi N} = 12.0^{+4.9}_{-3.5}$ mb ($43.0^{+17.5}_{-12.4}$ mb) at $p_\phi = 0.5$ GeV/c (1.8 GeV/c) where 0.5 GeV/c (1.8 GeV/c) is the average p_ϕ in the lowest p_ϕ bin in this experiment (the average p_ϕ in the previous experiment). Last, on the assumption that $\sigma_{\phi N}$ increases as p_ϕ^2 , the proportionality constant is estimated to be $27.2^{+13.5}_{-9.2}$ mb/(GeV/c)², which derives $\sigma_{\phi N} = 6.8^{+3.4}_{-2.3}$ mb ($88.1^{+43.7}_{-29.8}$ mb) at $p_\phi = 0.5$ GeV/c (1.8 GeV/c). Although the values of χ^2/ndf

Table 4.5: Summary of the degree of coincidence between the experimental data and each models.

Results of fitting for the data obtained only from this experiment.

Model function		Parameter α		χ^2/ndf	χ^2 probability
$\sigma_{\phi N} = \alpha$	w/ $K^\pm N$ interactions	$21.7^{+8.7}_{-6.2}$	mb	6.95/3	7 %
	w/o $K^\pm N$ interactions	$22.3^{+8.3}_{-6.0}$	mb	6.73/3	8 %
$\sigma_{\phi N} = \alpha \cdot p_\phi$	w/ $K^\pm N$ interactions	$23.9^{+9.7}_{-6.9}$	mb/(GeV/c)	2.77/3	43 %
	w/o $K^\pm N$ interactions	$24.9^{+9.4}_{-6.8}$	mb/(GeV/c)	2.48/3	48 %
$\sigma_{\phi N} = \alpha \cdot p_\phi^2$	w/ $K^\pm N$ interactions	$27.2^{+13.5}_{-9.2}$	mb/(GeV/c) ²	1.32/3	72 %
	w/o $K^\pm N$ interactions	$29.3^{+13.6}_{-9.4}$	mb/(GeV/c) ²	1.20/3	75 %

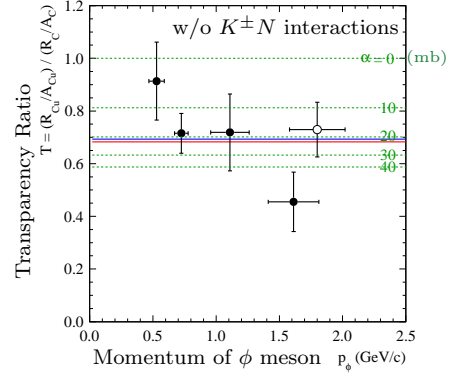
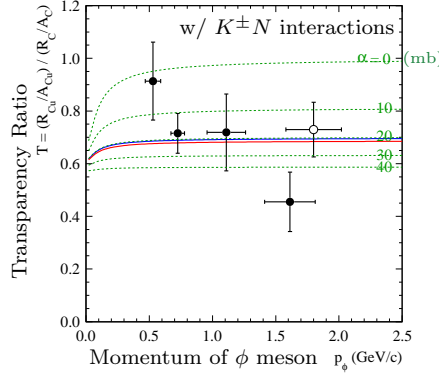
Results of fitting for the data obtained both from this experiment and the previous experiment.

Model function		Parameter α		χ^2/ndf	χ^2 probability
$\sigma_{\phi N} = \alpha$	w/ $K^\pm N$ interactions	$20.4^{+7.0}_{-5.3}$	mb	7.10/4	13 %
	w/o $K^\pm N$ interactions	$21.0^{+6.8}_{-5.1}$	mb	6.89/4	14 %
$\sigma_{\phi N} = \alpha \cdot p_\phi$	w/ $K^\pm N$ interactions	$19.6^{+7.4}_{-5.4}$	mb/(GeV/c)	4.51/4	34 %
	w/o $K^\pm N$ interactions	$20.7^{+7.4}_{-5.4}$	mb/(GeV/c)	4.38/4	36 %
$\sigma_{\phi N} = \alpha \cdot p_\phi^2$	w/ $K^\pm N$ interactions	$19.1^{+10.4}_{-6.8}$	mb/(GeV/c) ²	5.48/4	24 %
	w/o $K^\pm N$ interactions	$21.6^{+10.8}_{-7.4}$	mb/(GeV/c) ²	5.76/4	22 %

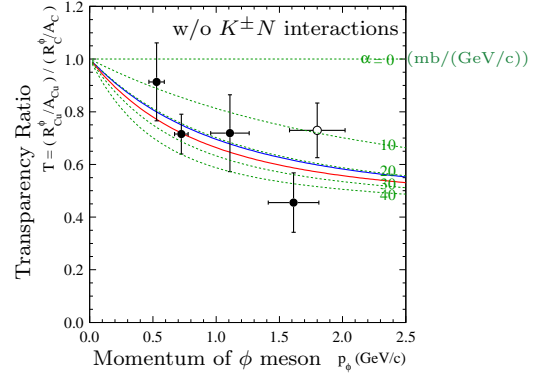
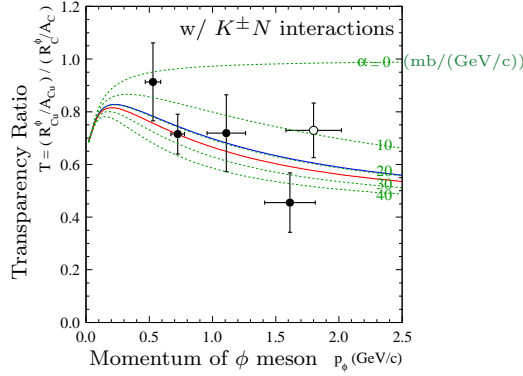
is better when it is assumed that $\sigma_{\phi N}$ increases as p_ϕ^2 , these are not significant differences between each assumption. Whereas, in the case that the data obtained both from this experiment and from previous experiment is used for the calculations, the values of χ^2/ndf is slightly worse when it is assumed that $\sigma_{\phi N}$ increases as p_ϕ . We have confirmed that the above results are not affected significantly by the presence of the $K^\pm N$ interactions in our momentum region. The transparency ratio T and the model calculations are shown in Fig. 4.2. The data obtained from this experiment are shown with closed blacks. The data obtained from the previous experiment [15], extracted only from C and Cu target, are superimposed into the same plot with open circles. The green dotted lines with the numerical values show the model calculations using the parameter α of the numerical values. The red lines show the results of fitting for the data obtained only from this experiment, and the blue lines show the results of fitting for the data obtained both from this experiment and the previous experiment. The degree of coincidence between the data and each models are summarized in Table 4.5.

The result suggests that $\sigma_{\phi N}$ increases as p_ϕ , although it is not statistically significant. In the lower p_ϕ , the ratio of the ϕ mesons decay inside the nucleus is higher, therefore the more accurate information in the nucleus is extracted. At the average of ϕ momentum in the lowest momentum bin in this experiment, the ratio of the ϕ mesons decay inside and outside the nucleus N_ϕ^{in}/N_ϕ^{out} is 0.047 (for C) 0.11 (for Cu) at $\langle p_\phi \rangle \approx 0.5$ GeV/c. Whereas, at the average in the previous experiment, N_ϕ^{in}/N_ϕ^{out} is 0.015 (for C) 0.034 (for Cu) at $\langle p_\phi \rangle \approx 1.8$ GeV/c. The ratio of the decay inside the nucleus in the lowest momentum bin in this experiment is approximately three times higher than the average in the previous experiment. We have confirmed that $\sigma_{\phi N}$ obtained in the low p_ϕ region is consistent with the theoretically predicted value in free space (≈ 10 mb [21, 22]). On the other hand, $\sigma_{\phi N}$ obtained in the high p_ϕ region is consistent with the result of previous experiment (≈ 35 mb [15]). For further study, it is essential to measure the absolute cross section, improve the statistical precision, and take the data with many kinds of target nuclei, especially with deuteron. The LEPS collaboration has studied the incoherent ϕ photo-production from deuteron at forward angles at $E_\gamma = 1.5$ -2.4 GeV, and reported that a significant reduction of the transparency ratio for the deuteron [28]. Since the deuteron is composed of a loosely bound proton and neutron, where the nuclear medium effect is minimal, this observation suggests that some effect other

Model function: $\sigma_{\phi N} = \alpha$



Model function: $\sigma_{\phi N} = \alpha \cdot p_{\phi}$



Model function: $\sigma_{\phi N} = \alpha \cdot p_{\phi}^2$

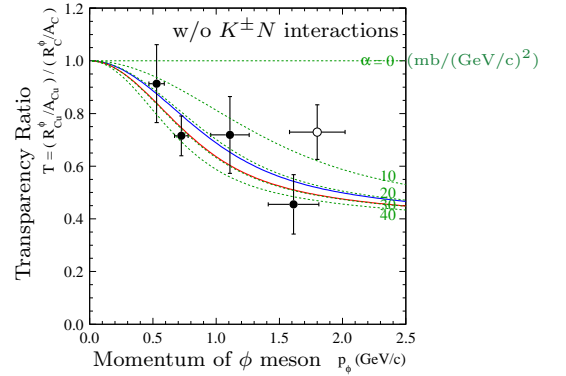
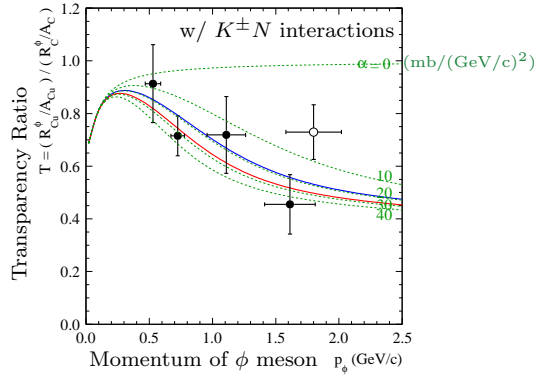


Figure 4.2: The transparency ratio and the model calculations on the basis of some different models. The data obtained from this experiment are shown with closed blacks. The data obtained from the previous experiment [15], extracted only from C and Cu target, are superimposed into the same plot with open circles. The green dotted lines with the numerical values show the model calculations using the parameter α of the numerical values. The red lines show the results of fitting for the data obtained only from this experiment, and the blue lines show the results of fitting for the data obtained both from this experiment and the previous experiment.

than nuclear density is necessary to achieve a complete understanding of the reduction of the ϕ production in the nuclear medium.

Chapter 5

Conclusion

The backward ϕ photo-production from C and Cu targets at $E_\gamma = 1.5$ -2.4 GeV has been studied at SPring-8/LEPS facility.

In our previous publication [15], we reported the ϕ photo-production from Li, C, Al, and Cu targets at forward angle with the LEPS spectrometer in the ϕ momentum range of 1.0-2.2 GeV/ c (the average ≈ 1.8 GeV/ c). The incoherent ϕ photo-production cross section (σ_A) turned out to be proportional to $A^{0.72 \pm 0.07}$, where A is the target mass number. The ϕ -nucleon interaction cross section ($\sigma_{\phi N}$) in the nuclear medium was estimated to be 35^{+17}_{-11} mb using the Glauber multiple scattering theory, while $\sigma_{\phi N}$ is predicted to be ≈ 10 mb from the theoretical calculations. The COSY/ANKE collaboration reported that the transparency ratio for ϕ mesons decreases with ϕ momentum [19], whereas the CBELSA/TAPS collaboration reported that the transparency ratio for ω [16], and η' mesons [17] are constant, independent to their momenta.

In order to obtain the further knowledge, we have performed the new experiment with a time projection chamber (TPC), which was newly installed to enlarge the detector acceptance. Combined use of the TPC and the existing LEPS spectrometer provides a drastic increase of the detector acceptance and gives a wide momentum coverage of 0.3-2.0 GeV/ c for ϕ mesons. It is the first measurement of the photo-produced ϕ mesons from nuclear targets with momentum less than 1.2 GeV/ c , where the ϕ mesons were identified from the K^+K^- invariant mass distributions. We have derived the transparency ratio from the production rates of ϕ mesons over the range of 0.3-2.0 GeV/ c . We have confirmed that the transparency ratio decreases with ϕ momentum, which is the same tendency as the result of COSY/ANKE collaboration [19].

We have performed the validation on the momentum dependence of $\sigma_{\phi N}$. In order to extract $\sigma_{\phi N}$ from the transparency ratio, an optical model of a Glauber multiple scattering theory has been applied. The detail of this procedure is discussed in Appendix E.1. When the ϕ mesons decay inside the nucleus, the K^+K^- invariant mass spectrum might be strongly distorted by the K^-N or the K^+N interaction. Therefore we assumed that a ϕ meson was lost if it decayed inside nuclei. The data obtained from this experiment is used for the following calculations. First, on the assumption that $\sigma_{\phi N}$ is a constant (, independent of p_ϕ), $\sigma_{\phi N}$ is estimated to be $21.7^{+8.7}_{-6.2}$ mb, which agrees with the result in previous experiment within the statistical errors. Next, on the assumption that $\sigma_{\phi N}$ increases as p_ϕ , the proportionality constant is estimated to be $23.9^{+9.7}_{-6.9}$ mb/(GeV/ c), which derives $\sigma_{\phi N} = 12.0^{+4.9}_{-3.5}$ mb ($43.0^{+17.5}_{-12.4}$ mb) at $p_\phi = 0.5$ GeV/ c (1.8 GeV/ c) where 0.5 GeV/ c (1.8 GeV/ c) is the average p_ϕ in the lowest p_ϕ bin in this experiment (the average p_ϕ in the previous experiment). Last, on the assumption that $\sigma_{\phi N}$ increases as p_ϕ^2 , the proportionality constant is estimated to be $27.2^{+13.5}_{-9.2}$ mb/(GeV/ c)², which derives $\sigma_{\phi N} = 6.8^{+3.4}_{-2.3}$ mb ($88.1^{+43.7}_{-29.8}$ mb) at $p_\phi = 0.5$ GeV/ c (1.8 GeV/ c). Although the values of χ^2/ndf is better when it is assumed that $\sigma_{\phi N}$ increases as p_ϕ^2 , these are not significant differences between each assumption. Whereas, in the case that the data obtained both from this experiment and from previous experiment is used for the calculations, the values of χ^2/ndf is slightly worse when it is assumed that $\sigma_{\phi N}$

increases as p_ϕ . We have confirmed that the above results are not affected significantly by the presence of the $K^\pm N$ interactions in our momentum region.

The result suggests that $\sigma_{\phi N}$ increases as p_ϕ , although it is not statistically significant. In the lower p_ϕ , the ratio of the ϕ mesons decay inside the nucleus is higher, therefore the more accurate information in the nucleus is extracted. We have confirmed that $\sigma_{\phi N}$ obtained in the low p_ϕ region is consistent with the theoretically predicted value in free space (≈ 10 mb [21,22]). On the other hand, $\sigma_{\phi N}$ obtained in the high p_ϕ region is consistent with the result of previous experiment (≈ 35 mb [15]). The reduction of the transparency ratio shown in the high p_ϕ region suggests that a diffractive ϕ photo-production might have a strong A -dependence. For further study of this phenomenon, it is essential to measure the absolute cross section, improve the statistical precision, and take the data with many kinds of target nuclei, especially with deuteron. The LEPS collaboration has studied the incoherent ϕ photo-production from deuteron at forward angles at $E_\gamma = 1.5$ -2.4 GeV, and reported that a significant reduction of the transparency ratio for the deuteron [28]. Since the deuteron is composed of a loosely bound proton and neutron, where the nuclear medium effect is minimal, this observation suggests that some effect other than nuclear density is necessary to achieve a complete understanding of the reduction of the ϕ production in the nuclear medium.

Appendix A

General Properties, Mechanical Design, and Operation of the TPC

A.1 General Properties of the TPC

A.1.1 Working Principle of the TPC

The TPC is a particle detector invented by David R. Nygren in the late 1970s [29]. This device is a three-dimensional tracking detector which consists of a gas-filled cylindrical chamber with multi-wire proportional chambers (MWPC) as endplate. The TPC records the trajectories of the charged particles, measures their momenta, and identifies the particles by measuring their ionization energy losses (dE/dx).

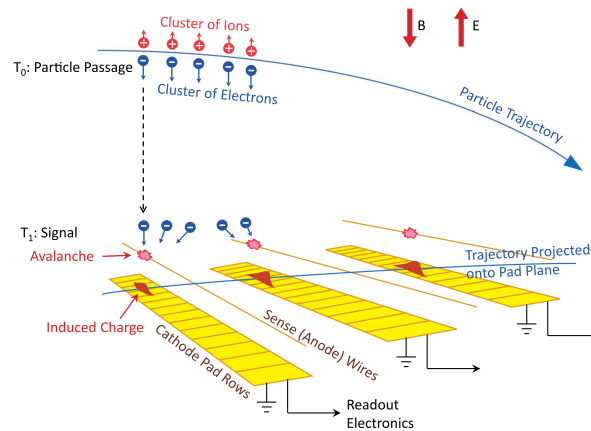


Figure A.1: Conceptual diagram for the working principle of a TPC. A particle passing through the gas cylinder volume produces free electrons along its track trajectory. Those ionization electrons drift towards the sense wires, and produce the avalanches in the immediate area of sense wires. The charges detected on the cathode pads give a two-dimensional projection of the particle trajectory. Combined with a measurement of the drift time, the particle trajectory in three dimension is reconstructed.

A particle passing through the gas cylinder volume produces free electrons along its track trajectory (in Appendix A.1.2). Those ionization electrons drift in the electric field (in Appendix A.1.3) towards the MWPC part, which is arranged with the sense (anode) wires and the cathode pad rows, and produce the avalanches. The center-of-gravity method for signals induced on the row of cathode pads (in Appendix A.1.4), gives the positions of avalanches on sense wires and the trajectories of tracks projected

onto the cathode plane. z -coordinate (along the cylinder axis) is given by the drift time of the ionization electrons. Many reconstructed space points for each track allow a full reconstruction of the particle trajectories. This is illustrated in Fig. A.1

A magnetic field is often applied parallel to the electric field in order to measure the momenta of charged particles and to suppress the transverse diffusion of electrons over long drift distances. The momenta of charged particles are known from the curvatures of their trajectory in the magnetic field. The suppression of the transverse diffusion is described in Appendix A.1.3. The simultaneous measurement of track momentum and of the energy deposition per unit length (dE/dx) allows to identify particle.

A.1.2 Gas Ionization by Charged Particles

A charged particle passing through the gas volume loses energy by excitation and ionization of gas. The most ionizing collisions produce only one electron/ion pairs. The primary electron produces secondary electrons due to collisions with other gas molecules until their kinetic energy is used up. The secondary electrons are usually created very close to the first electron/ion pair, therefore forming “clusters” along particle trajectory. In rare collisions, electron are ejected with high energy, so-called “ δ -electrons”, which leave a particle trajectory, produce more electrons, and create a track itself.

The distribution of the number of electrons in one cluster, so-called “Cluster size”, and the distribution of the number of clusters per cm are estimated using the HEED program [30]. These results are shown in Fig. A.2, assuming that the charged particle is proton with 0.5 GeV/c, and the volume is filled with Ar/CH₄ (90:10) gas mixture at $P = 1$ atm, $T = 300$ K and $B = 2$ T.

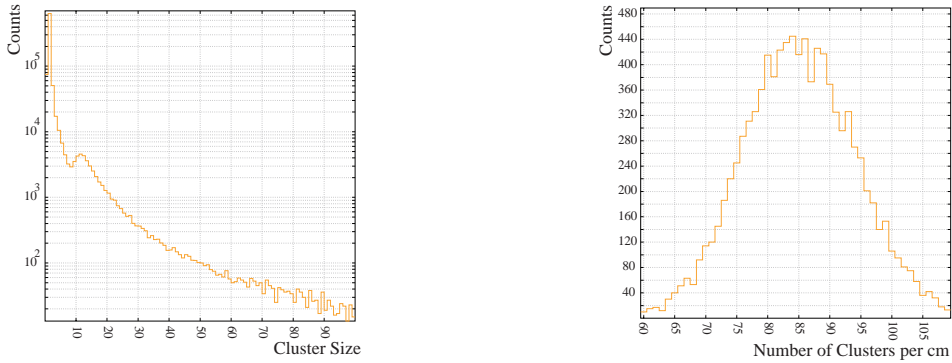


Figure A.2: The distribution of the expected cluster size (left) and the distribution of the expected number of clusters per cm (right) assuming that the charged particle is proton with 0.5 GeV/c, and the volume is filled with Ar/CH₄ (90:10) gas mixture at $P = 1$ atm, $T = 300$ K and $B = 2$ T. The effects of the argon M and L -shells are clearly seen in the left figure.

The particle identification (PID) with the TPC is based on the mean rate of energy loss per unit path-length of a relativistic charged particle in a medium, which is described by the “*Bethe-Bloch*” formula,

$$-\left\langle \frac{dE}{dx} \right\rangle = K z^2 \frac{Z}{A} \frac{1}{\beta^2} \left[\frac{1}{2} \ln \frac{2m_e c^2 \beta^2 \gamma^2 T_{\max}}{I^2} - \beta^2 - \frac{\delta(\beta\gamma)}{2} \right], \quad (\text{A.1})$$

where E is energy deposition from the incident particle, x is distance travelled by the incident particle, K/A is $4\pi N_A r_e^2 m_e c^2 / A$, N_A is Avogadro’s number, r_e is classical electron radius, m_e is electron mass, Z is atomic number of absorber, A is atomic mass of absorber, ze is charge of incident particle, T_{\max} is maximum kinetic energy, and I is mean excitation energy. It describes the mean energy loss in the region

$0.1 \lesssim \beta\gamma \lesssim 1000$ with an accuracy of a few %, and depend only on the momentum and its charge and rest mass of the particle. Thus, the simultaneous measurement of track momentum and of the energy loss per unit length allows to identify particles.

A.1.3 Motion of Charge Carriers in Gases

Drift

The electrons and ions created during the ionization process drift through the gas volume, due to the influence of electric and magnetic fields. In the equilibrium state, the vector sum of the electric force for the accelerating, of the Lorentz force for bending, and of the friction force for decelerating by the collisions with gas molecules, will vanish. The particle's equation of motion is

$$q \cdot \mathbf{E} + q \cdot (\mathbf{v}_{\text{drift}} \times \mathbf{B}) - k \cdot \mathbf{v}_{\text{drift}} = 0 \quad (\text{A.2})$$

where $\mathbf{v}_{\text{drift}}$ is the drift velocity vector, \mathbf{E} and \mathbf{B} are the electric and the magnetic fields, $k (> 0)$ is the phenomenological proportionality constant, $\tau = |m/k|$ is the mean time between collisions of the particle with gas molecules, and q and m are the charge and the mass of particle. The drift velocity vector $\mathbf{v}_{\text{drift}}$ reaches a local maximum if the gas molecules become invisible to the electron. This occurs when the quantum mechanical wavelength of the particle is equal to the width of the potential in which it travels, known as Ramsauer-Townsend effect.

Equation A.2 is solved for the drift velocity vector $\mathbf{v}_{\text{drift}}$. This result is the ‘‘Langevin Equation’’ written in the following way for an electron:

$$\mathbf{v}_{\text{drift}} = -\frac{\mu|\mathbf{E}|}{1 + \omega^2\tau^2} \left(\hat{\mathbf{E}} - \omega\tau(\hat{\mathbf{E}} \times \hat{\mathbf{B}}) + \omega^2\tau^2(\hat{\mathbf{E}} \cdot \hat{\mathbf{B}})\hat{\mathbf{B}} \right), \quad (\text{A.3})$$

where $\hat{\mathbf{E}}$ and $\hat{\mathbf{B}}$ are unit vectors in the directions of the corresponding fields respectively, μ is the electron mobility in the gas, and $\omega = |(q/m)\mathbf{B}|$ is the cyclotron frequency. The first term of Equation A.3 indicates the drift velocity of electron without the magnetic field. The second term represents the force which bends the electrons in the direction perpendicular to the electric and magnetic field. The third term represents the force which carries the electron not along the electric field, but along the magnetic field.

In a TPC, the so-called ‘‘ $E \times B$ effect’’ is distinguished as two different ones. One is the ‘‘*wire* $E \times B$ effect’’, caused by the Lorentz force in the space around the sense wires. This effect leads to the worsening of position resolution in $r \cdot \phi$ direction, but does not cause a systematic distortion of its position. In this analysis, the ‘‘*wire* $E \times B$ effect’’ is implemented into the *resolution-map*, and its position distortion is not considered further. The other is the ‘‘*drift* $E \times B$ effect’’, arisen from the inhomogeneities of the electric and the magnetic fields in the active gas volume in the TPC. This latter effect is discussed in more detail below.

Here, we think about the distortions of drift trajectory in gas volume arising from the inhomogeneities of the electric and the magnetic fields. Assuming a nearly homogeneous electric field $\mathbf{E} = (E_x, E_y, E_z)$ and magnetic field $\mathbf{B} = (B_x, B_y, B_z)$ with small transverse components $|E_x|, |E_y| \ll |E_z|$, and $|B_x|, |B_y| \ll |B_z|$, using Equation A.3, we obtain the components of the approximative distortions:

$$\begin{aligned} \Delta_x &\simeq -\frac{L}{1 + \omega^2\tau^2} \left(+\omega\tau \frac{B_y}{B_z} + \omega^2\tau^2 \frac{B_x}{B_z} + \frac{E_x}{E_z} - \omega\tau \frac{E_y}{E_z} \right), \\ \Delta_y &\simeq -\frac{L}{1 + \omega^2\tau^2} \left(-\omega\tau \frac{B_x}{B_z} + \omega^2\tau^2 \frac{B_y}{B_z} + \frac{E_y}{E_z} + \omega\tau \frac{E_x}{E_z} \right) \end{aligned} \quad (\text{A.4})$$

where $L (> 0)$ is the drift length, $E_z > 0$ and $B_z < 0$. By contrast, in case of $|E_x|, |E_y| \not\ll |E_z|$ or $|B_x|, |B_y| \not\ll |B_z|$, the approximative Equation A.4 holds no more, and the calculation of drift orbit requires to solve the Equation A.3 strictly.

Diffusion

A charge cloud of electrons drifting through a gas volume is subject to the influence of scattering with the gas molecules. Such cloud spreads out/along the field lines, and these processes are called transversal/longitudinal diffusion respectively. The mean squared deviations σ_T and σ_L in transversal and longitudinal directions during the drift of the electrons cloud over a distance L is described as:

$$\sigma_T = D_T \sqrt{L} \quad (\text{A.5})$$

$$\sigma_L = D_L \sqrt{L}, \quad (\text{A.6})$$

where D_T and D_L are the transverse and longitudinal diffusion coefficients respectively.

The transverse diffusion is suppressed by a magnetic field parallel to \mathbf{E} according to

$$\sigma_T(B) = \frac{\sigma_T(0)}{\sqrt{1 + \omega^2 \tau^2}}, \quad (\text{A.7})$$

where $\sigma_T(0)$ is the transverse diffusion at $B = 0$ T. This reduction is essential for the operation of the TPC because it has long drift distance. However, the longitudinal diffusion remains unchanged:

$$\sigma_L(B) = \sigma_L(0). \quad (\text{A.8})$$

A.1.4 Signal Formation

Gas Amplification

An drift electron reached in the high electric field up to several 10^4 V/cm around the thin sense (anode) wires starts an avalanche multiplication. The physical processes inside the avalanche are quite complicated, as they involve single and multiple ionization, optical and metastable excitations, recombinations, and energy transfer by collisions between atoms.

The gas chamber is usually operated in proportional mode, and the created signal is proportional to the number of electrons collected. However, the photons created in the avalanche process, which have enough energy, can travel further from the original avalanche, start other avalanches, and cause the loss of the proportionality. This is the reason why an organic quench gas is mixed into the noble gas. Organic molecules have a high cross section for photons, and prevent the affection from photons. In this experiment, we mixed CH_4 into Ar as quench gas (See in Appendix A.2.1).

Signal Induction

The movement of electrons and ions induce a electric signal not only on the wires but also on the cathode pads. The electrons created in avalanche move and absorb to the wire within a nanosecond, and result a very short signal pulse. The ions created in avalanche move away from the wire slowly, which velocity is a factor of 10^3 smaller than electrons one, result a signal with a long tail. The center-of-gravity of induced signals gives the location of avalanche, and the sum of the induced signal gives the total number of avalanche electrons, which is proportional to the primary electrons.

The signals induced on the wire and the grounded cathode pads are processed by readout electronics, which consist of amplifiers, shapers, and digitizer for the waveform of signals.

A.2 Mechanical Design and Operation of the TPC

A.2.1 Choice of Gas Mixture

The drift velocity for the electrons in the gas must be known with a sufficient accuracy in order to convert the measured time into a position. But the drift velocity could be changed with the small variations in temperature and pressure. To minimize the influence from these variations, we set the electric field in the TPC corresponds to the peak in the drift velocity curve. Operating on the peak of the velocity curve makes the drift velocity stable and insensitive to small variations in temperature and pressure.

The values of drift velocity for some gases at $P = 1$ atm, $T = 300$ K, and $B = 2$ T are shown in Fig. A.3. These have been computed with the MAGBOLTZ program [31].

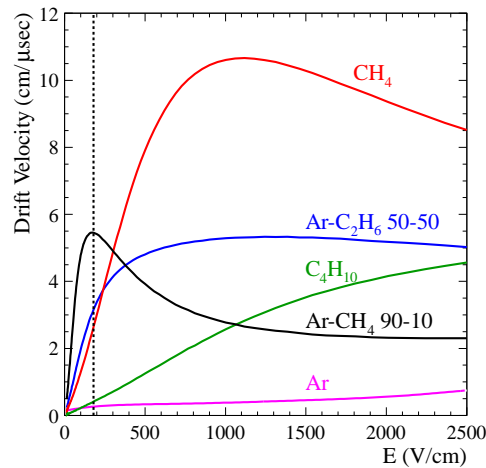


Figure A.3: The drift velocities of electron as a function of the strength of electric field in several gases at $P = 1$ atm, $T = 300$ K and $B = 2$ T. The dotted line shows the setting value of electric field (180 V/cm) for the operation in this experiment.

In this experiment, the TPC is filled with Ar/CH₄ (90:10) gas mixture (called as “P10” gas mixture) regulated at atmospheric pressure. The attribute of P10 gas mixture is a fast drift velocity which peaks at a low electric field strength. The dotted line in Fig. A.3 shows the setting value of electric field (18 V/mm) for the operation.

A.2.2 Electric Field

The calculation of the electric field in the TPC is performed using the GARFIELD program [32]. The field strips on the field cage and on the target holder, The high voltage membrane, the cathode pad plane the sense, field, shield, and gate wires, are taken into account in the calculation. The length of the field cage in the z-direction is shorter than the real length because the memory size is not sufficiently large to include all strips on the field cage. The equipotential contour plot in the TPC is shown in Fig. A.4.

The electric field near the field cage or the target holder is distorted due to the configuration structure of the field strips. In this analysis, the signals from the most inner layer (1st layer) and the most outer layer (14th layer) are not used for the track reconstruction, to keeping the good performance of the TPC.

We only used the signals from 2st to 13th layers, on the assumption that the electric field is homogeneous as $\mathbf{E} = (0, 0, +18.)$ [V/mm].

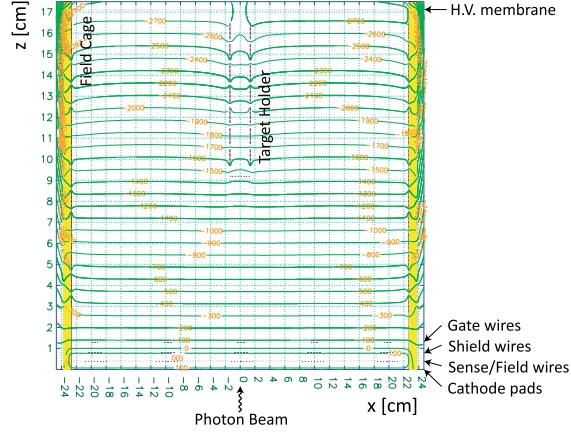


Figure A.4: The calculated electric field map in the TPC. The lines with green color show the equipotential lines, and the numerical values with yellow color show the electric potentials. Here, the length of the field cage in the z -direction is shorter than the real length.

A.2.3 Magnetic Field

In this experiment, the two magnets, superconducting solenoidal magnet and the dipole magnet, are used.

The TPC is sit in the superconducting solenoidal magnet. The magnet is used to measure the momenta of the charged particles in the TPC, and to suppress the transverse diffusion of electrons over long drift distances. The magnet has an aperture with 300 mm in radius, and the center of the magnet is located at $z=1527$ mm along the beam axis. The magnitude of the magnetic field is 2 Tesla at the center of the solenoid magnet.

The dipole magnet is placed at the center of the experimental hutch ($z=0$ mm), and is used to analyze the momenta of the charged particles flighting into the forward angles. The dipole magnet has an aperture with 1350 mm width and 550 mm high, and the length between the pole edges is 600 mm. The magnitude of the magnetic field is 0.7 Tesla at the center of the dipole magnet.

The magnetic filed in the TPC is composed of the field from the solenoidal magnet mainly, and of the small leakage field from the the dipole magnet. Figure A.5 shows the magnetic field map for B_z and B_y on the vertical plane ($x=0$ mm) around the TPC calculated using the RADIA program [33]. The sums of the magnetic field of the solenoid and the dipole magnet are shown. The rectangles indicate the active volume of the TPC, and the cross marks indicate the center positions of the targets ($z=-1527$ mm).

A.2.4 Gas Amplification

The gas amplification part of the TPC consists of a gate-wire grid, a shield-wire grid, a sense-wire (anode-wire) grid and a cathode pad plane. Figure A.6 shows a schematic drawing of the gas amplification part.

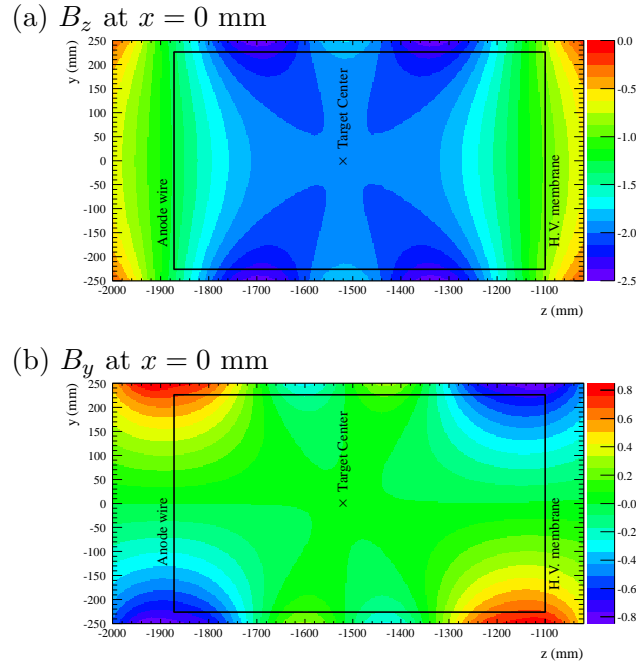


Figure A.5: The magnetic field B_z (a) and B_y (b) on the vertical plane ($x=0$ mm) around the TPC. The rectangles indicate the active volume of the TPC, and the cross marks indicate the center positions of the targets.

Wires

The gate-wire grid is used to prevent the electrons ionized by the synchrotron X-rays or the positive ions created by avalanche, and played an important role to avoid the space charge effect. The voltage of the gate wires is set to be -290 V/ -110 V alternately when the gate is closed, and set to -90 V and opened for 25 μ sec when the trigger signal comes. Figure A.7(a-b) show the trajectory of electrons when the gate is opened or closed, and (c) shows the trajectory of positive ions from sense wires when the gate is closed, computed with the GARFIELD program [32]. The shield wires are set to be 0 V to form the electric field in the avalanche region. The sense and field wires are stretched alternately with 4 mm spacing, and the spacing to the cathode pad plane is 4 mm. The reference voltage of the sense wires is set to be $+1.62$ kV. We adjusted the voltage of the sense wires finely, every few hours, in order to maintain a constant gain. In order to avoid an electric discharge between the sense and field wire, The voltage of the field wires are set to $+220$ V.

The characteristics of the wire grids are summarized in Table A.1.

Table A.1: Characteristics of the wire grids.

	Material	diameter (μ m)	Wire spacing (mm)	Distance from pad plane (mm)	Number of wires	Applied voltage (V)
Gate	Au-BeCu	100	2	13	191	-90 (open) -290/-110 (close)
Shield	Au-BeCu	100	2	8	191	0
Field	Au-BeCu	100	4	4	96	+220
Sense	Au-W	20	4	4	95	+1620

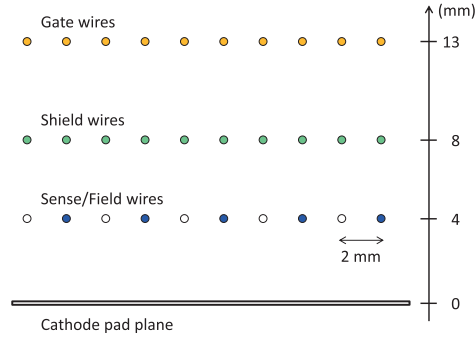


Figure A.6: Schematic view of the gas amplification part of the TPC.

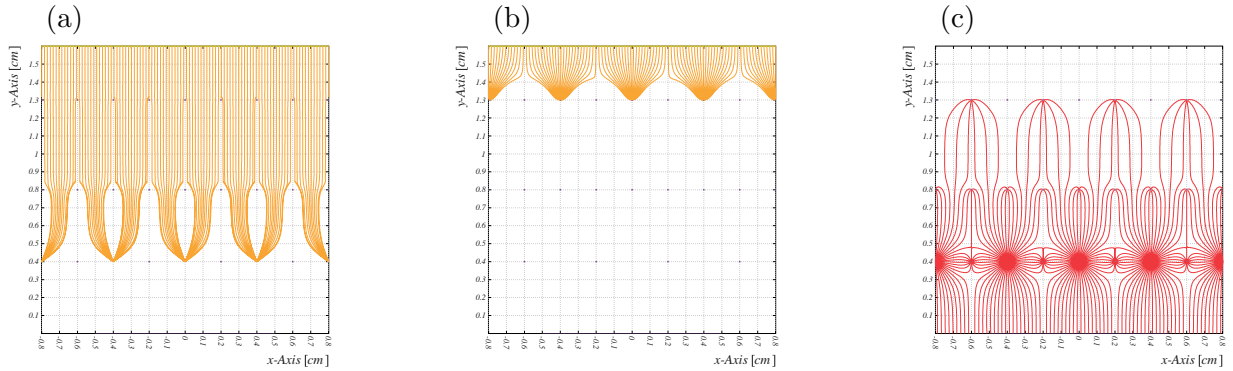


Figure A.7: Drift lines of electrons from track when gate is opened (a) and closed (b). Drift lines of positive ions from sense wires when gate is closed (c).

Cathode Pads

In the vicinity of a sense wire, the electrons create an avalanche and induce signals on the cathode pads. The signals are read through cathode pads which are arranged as 14 concentric circles. The pad size at inner 6 rows, from 16.5 to 61.5 mm in radii, had $4.5 \text{ mm} \times 7.0 \text{ mm}$. And the pad size at outer 8 rows, from 75.5 to 194.5 mm in radii, had $7.5 \text{ mm} \times 13.0 \text{ mm}$. The total of inner pads are 293, and of outer pads are 762. The configuration of the pad plane is shown in Fig. A.8.

Readout Electronics

Signals from the TPC are amplified by charge-sensitive preamplifiers and shaping amplifiers. The preamplifier has the integration time of 132 nsec and the gain of 2.5 V/pC . The shaping amplifier is the CR-(RC)^4 type band-pass filter with the shaping time of 20 nsec. The FWHM of the output signal from the shaping amplifier is typically 200 nsec. The waveform of signals is digitized by the flash analog-to-digital converter (FADC) module. The FADC has a of 10 bit resolution and 40 MHz sampling rate.

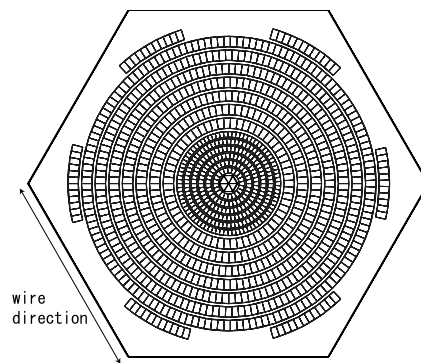


Figure A.8: The configuration of the cathode pad plane.

Appendix B

Analysis Procedure for TPC

B.1 Outline

This chapter focuses on the reconstruction framework. In this chapter, we use the following terms:

- “Cluster” means a set of adjacent (in space and in time) signals on cathode pads that are generated by the same particle crossing the sensitive element of a detector.
- “Hit” is the estimated space point where a particle crossed the sensitive element of a detector. Hit is a container of measurements on a segment of the particle trajectory.
- “Track” is the estimated trajectory of the particle with a set of five parameters.

The “cluster/hit/track reconstruction” means a series of steps for the making clusters/hits/tracks, respectively, and their conceptual diagrams are shown in Fig. B.1.

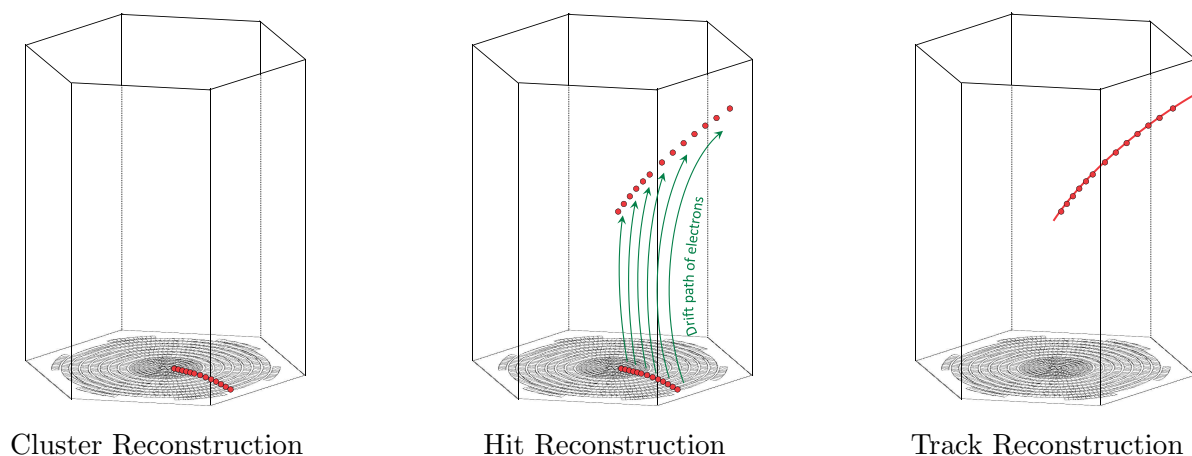


Figure B.1: Conceptual diagram of data analysis: cluster reconstruction (left), hit reconstruction (center), and track reconstruction (right).

B.2 Preprocessing

B.2.1 Waveform Reconstruction from the Saturated Signals

The signals from the TPC are amplified by the charge-sensitive preamplifiers and the shaping amplifiers. And the waveforms of the amplified signals are digitized and recorded by the FADC module with 10 bit resolution and 40 MHz sampling rate. However, the charged particles passing through the gas volume with slow $\beta\gamma$ (like a proton with small momentum) lose large energies by excitation and ionization of gas, and the signal heights generated from such particles sometimes exceed beyond the dynamic range of the FADC module and the waveforms are recorded with the saturation of pulse height. Before a series of data processing, we performed the waveform reconstruction from the saturated signals.

The original waveform of such a saturated signal is estimated by fitting the Gaussian convoluted exponential function to the waveform. In the following analysis, the timing and the height of signal are determined using the corrected waveform. Figure B.2 shows a saturated waveform (solid line with black color) and a corrected one (dotted line with red color) in a certain signal.

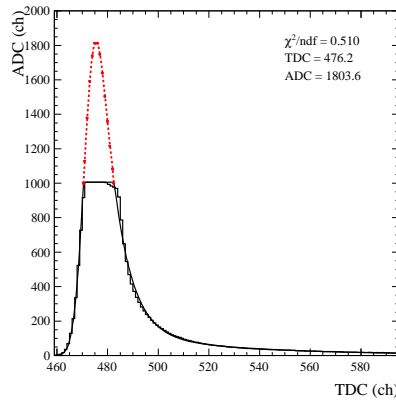


Figure B.2: A saturated waveform (solid line) and a corrected one (dotted line) in a certain signal.

B.2.2 Time Offset and Gas Mobility

The time offset has several origins: the trigger delay, the time of signal transmission in the front end of electronics, and the time of drifting from the gating grid to the sense wires and so on.

The trigger delay is constant over the full volume of the TPC, so the timing offset is adjusted together with the gas mobility. The *global* time offset and the gas mobility is monitored using the z-coordinate of carbon plate embedded on the shield wire and of the kapton membrane embedded on the upstream edge of the target holder in the two-track vertex (*vtz*) distribution. Figure B.3 shows the mobility of the electron in the active volume of the TPC. The mobility has changed while the data taking, depending on the pressure of the P-10 gas. The *global* time offset is set the constant value of $+3.253 \mu\text{sec}$.

The local variations of the time offset is appear due to the differences of circuit length between each electronic channel, and the asymmetry in geometry between the arrays of sense wires and of pad rows, and so on. The time zero (T_0) in every FADC channel is determined using the z-component of tracking residual from traversing tracks parallel to cathode pad plane. Figure B.4 shows the T_0 in each FADC channel.

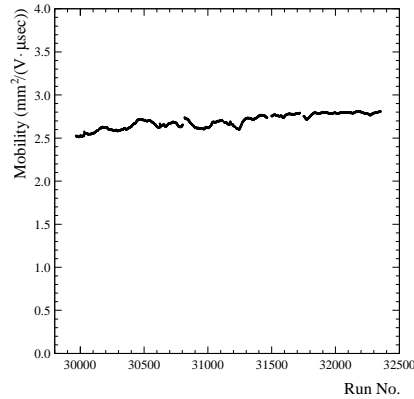


Figure B.3: The mobility of the electron in the active volume of the TPC as a function of the run number.

Time zero (T_0) in every FADC channel is determined using the z-component of tracking residual from drifting tracks parallel to cathode pad plane. Figure B.4 shows the T_0 position of each FADC channel.

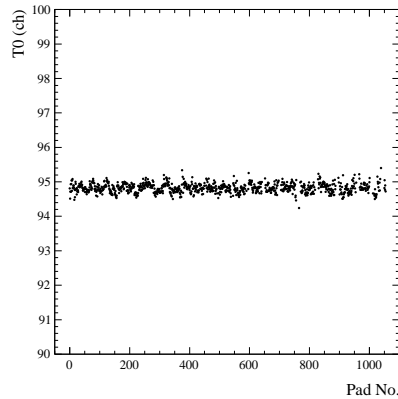


Figure B.4: T_0 of each FADC channel.

To determine the mobility and T_0 with precision, the accurate reconstruction of hits and tracks is essential. So, the parameters of these and others are determined with many times iteration alternately.

B.3 Cluster Reconstruction

B.3.1 Cluster Reconstruction

The multiple tracks or even a single track which traverse at a large angle to the sense wire plane make the signals consist of multiple peaks structure, called as “pile-up pulse”. We will describe the ways to treat pile-up pulses and to perform the “cluster reconstruction” process, in below.

At first, we will think about the simple case that only one track traverses parallel to the sense wire

plane where the three sense wires (black, red, and blue) are located on one cathode pad, as shown in Fig. B.5 (a). Figure B.5 (b) shows the induced currents on the cathode pad arisen from avalanches on each sense wire. Each lines are corresponding to the signals from the sense wire with same color. Figure B.5 (c) shows the observed signal which is equal to the sum of components from each wires. Its shape is the clean and sharp.

Next, we will think about the another case that the track traverses at an large angle to the sense wire plane as shown in Fig. B.5 (d). Because of the differing distances to the sense wires, the induced currents on the cathode pad arisen from avalanches on each wires are spread out over a time period corresponding to the drift times of the electrons, sometimes up to a few μsec , as shown in Fig. B.5 (e). The induced current on the cathode pad is amplified by charge-sensitive preamplifier with the integration time constant of 132 nsec. When the induced current keeps on arising beyond the integration time constant of preamplifier, the preamplifier starts to discharge before finishing to collect whole signal, and make the multi peak and long tail structure in output signal as shown in Fig. B.5 (f). In reality, the dispersion of cluster size distribution make the signal shape to be with more complicated fluctuation.

The shaping amplifiers are used following the charge sensitive preamplifier stage, and perform to produce an output pulse spread and shaped like a Gaussian function. And the waveforms of the amplified signals are digitized and recorded by the FADC module.

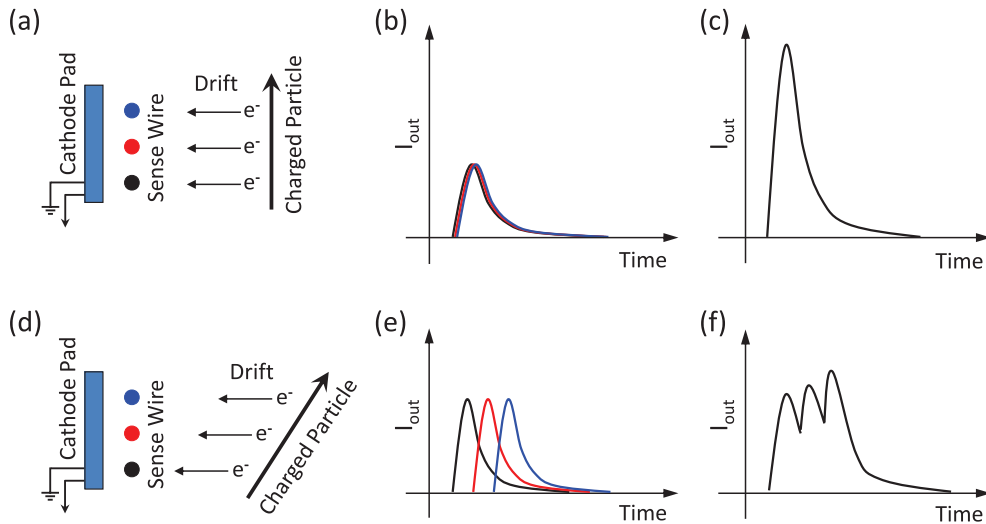


Figure B.5: (a): A track flying parallel to the sense wire plane where the three sense wires (black, red, blue) are located on one cathode pad. (b): The induced currents (I_{out}) on the cathode pad arises from avalanches on each sense wire. Each lines are corresponding to the signals from the sense wire with same color. (c): Observed signal which is equal to the sum of components from each wires. (d)~(f): In the case of a track flying at an angle with the sense wire plane.

Figure B.6 shows the conceptual diagram of the cluster reconstruction, where the array of FADC channels is corresponding to the one of cathode pads.

The signals in each FADC channel are split at local minimum points, and the created fragment pulses are associated with the coincidence of the peak timing in neighborhood channels (in figure, the succeeded ones show with the red points, and failed ones with the blue points). The fragment pulses A-1, B-1, C-1, and D-1 are grouped into “pre-cluster A”, and C-4, D-4 and E-4 into “pre-cluster B”. After the hit- and the track-reconstruction (See section B.5) using *pre-clusters*, some of the remaining signals (the

blue points in figure) are re-combined with other fragment and are re-grouped into clusters, judging by the trajectories of each tracks and the pulse shapes. B-1,2 and D-1,2,3 and D-4,5 are re-combined respectively, and finally two clusters: the “cluster A” consists of A-1, B-1,2, C-1, and D-1,2,3, and the “cluster B” consists of C-4, D-4,5, and E-4, are formed.

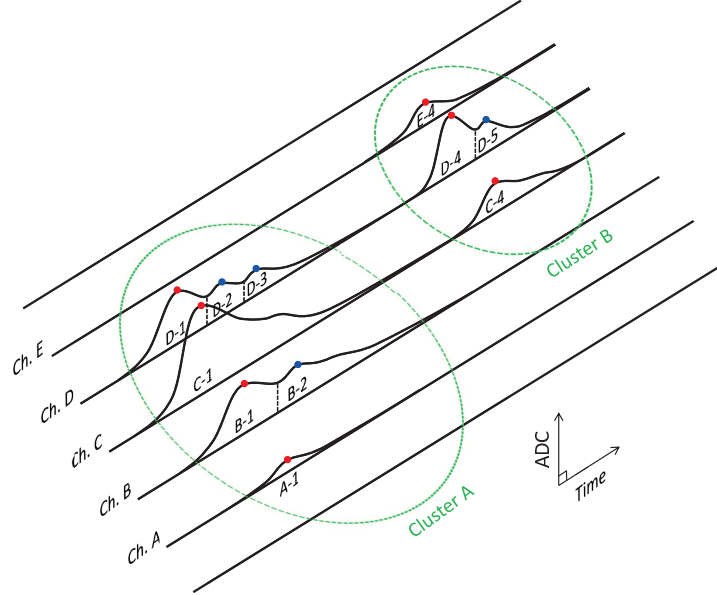


Figure B.6: Conceptual diagrams of the cluster reconstruction.

B.3.2 Amount of Charge in Each Signal

The measurement of the amount of charge with accuracy is thought to be essential for the reconstruction of hit positions and the particle identification (PID) with accuracy. With this aim, we think the following two approaches for the measurement of the amount of charge in each signal (in each channel):

Method. 1 : Measuring the height of a signal pulse in FADC.

Method. 2 : Measuring the time integration of a signal pulse in FADC.

In the case that the pulse-duration time is sufficiently shorter than the time constant of the amplifiers, the amplifier stage in this experiment is worked as a current integrator, which is an electronic device performing a time integration of an electric current, thus measuring a total electric charge. The amplified signal, same as the input signal into the FADC, has the pulse height which is proportional to a inputted total electric charge. However, in the case that the pulse-duration time is no longer short, the amplified signal shows the pulse height reduction with the pulse-duration time dependence, and the waveform with complicated structure as described in Sec. B.2.1. Although, the *Method. 1* is the general and simple method used for measuring the the amount of charge, we need to decompose the pile-up pulse perfectly, and to sum up the pulse heights of each decomposed pulse with the pulse height correction for the pulse-duration time dependence. Actually, this is not always easy because of the large fluctuation of waveform.

By contrast, in the method *Method. 2* , the time integration of FADC signal is always proportional to the amount of a inputted total electric charge, with independent of both the pulse shape and the

pulse-duration time. We adopted the method *Method. 2* for the measurement of charge in each signal in this analysis.

B.3.3 Gain Calibration

The gain correction is applied as follow:

$$ADC_{cor} = ADC_{orig} * par1 + par2 \quad (\text{B.1})$$

where ADC_{orig} and ADC_{cor} are the original ADC values and the corrected one, and $par1$ and $par2$ are coefficients for the gain correction, depending on the *pad-ID* and on the *run-Number*.

The coefficients are determined in such a way that the most probable value of the energy deposition from π^+ and proton is to be constant in every cathode pad and in every run. The track selection cuts are applied as follows: the track had the positive charge, had the momentum between 0.25 and 0.30 GeV/c, and traversed parallel to the sense wire plane. Figure B.7 shows the most probable value of energy deposition from π^+ and proton *in every cathode pads* before (top) and after (bottom) applying the gain correction. And, Figure B.8 (top) shows the most probable value of energy deposition from π^+ and proton *in every run* before (top) and after (bottom) applying the gain correction. These figures show the improvements in the *pad-ID* and the *run-Number* dependences after applying the gain correction.

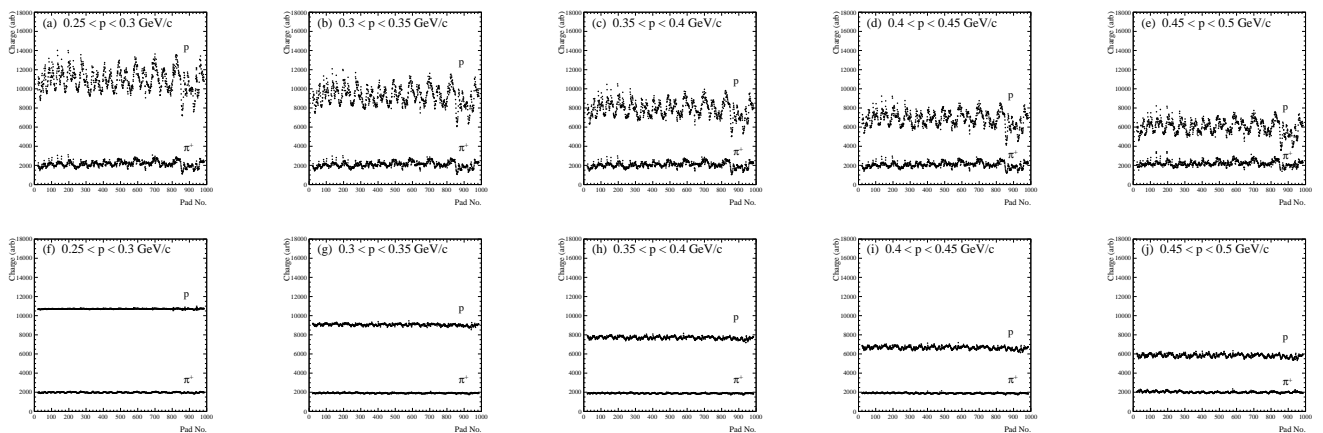


Figure B.7: The most probable value of energy deposition in every cathode pads before (top) and after (bottom) applying the gain correction.

B.4 Hit Reconstruction

The cluster coordinate is obtained in the cylindrical coordinate system defined in Sec. 2.9. The radial coordinate (r) is obtained from the center of the pad layer, and the coordinate along the pad row (ϕ) is obtained from the center-of-gravity of the induced charges, where typically three pads have induced charges from an avalanche, and a Gaussian charge distribution is assumed.

The hit coordinate is obtained by solving the equation of motion of electrons in the gas with the electric and magnetic field using the cluster coordinate and drift time. The details are described in Appendix A.1.3.

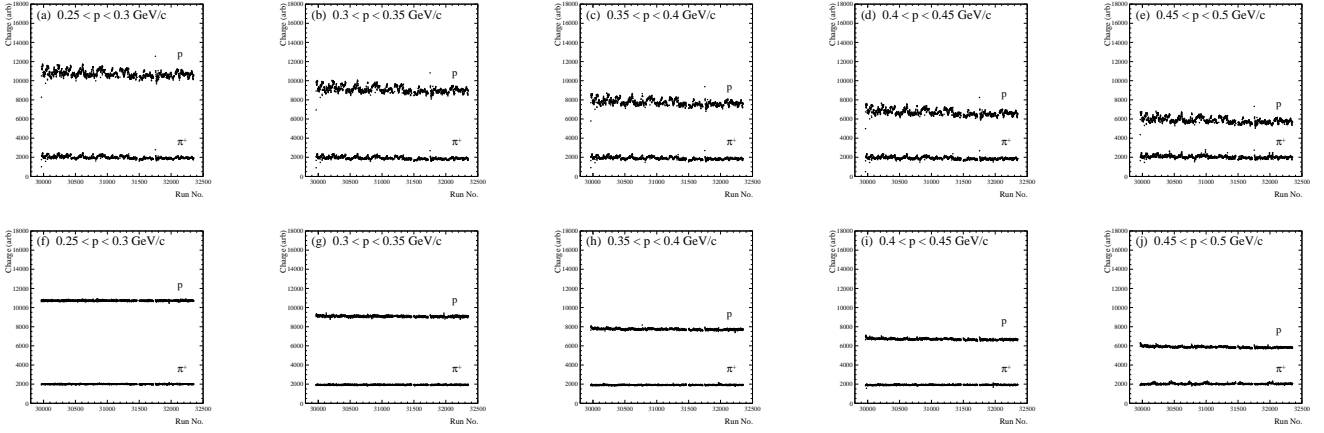


Figure B.8: The most probable value of energy deposition in every run before (top) and after (bottom) applying the gain correction.

B.5 Track Reconstruction

The finding of the track is performed on the basis of the principle in Ref. [34], and the algorithm is as follows:

- *Step.1*
Selecting the hits on the most outer three layers.
- *Step.2*
Reconstructing a helix from the coordinates of the selected hits.
- *Step.3*
Searching a hits which associates with the helix in the next inner layer. and to register the hits to the track candidate if it is close to the helix within 3 mm in $r\phi$ direction and 6 mm in z direction.
- *Step.4*
Obtaining the helix parameters using all of the hits registered to the track candidate.
- *Step.5*
The procedures *Step.3* and *Step.4* are repeated until all layers are searched. If the number of hits associated with the track candidate is less than 5, the track candidate is discarded.

The momentum of a detected particle is obtained by solving the equation of motion in the inhomogeneous magnetic field with the Runge-Kutta integration and fitting with MINUIT routine [35]. If the χ^2 probability for the track fitting is less than 0.02, the hit with the largest χ^2 value is removed, and the track fitting is applied again. This procedure is repeated until the χ^2 probability become larger than 0.02, or the number of hits associated with the track becomes less than 6. In order to reject noise, tracks with χ^2 probability are selected.

After the track reconstruction, we calculated the following variables:

- $(dx)_{\text{cathode}}$: path length of each hit on cathode plane.

- $(dx)_{\text{hit}}$: path length of each hit in three dimension.

The conceptual diagrams of them are shown in Fig. B.9. These variables are used for the calculation and correction of dE/dx , described in Appendix B.6.

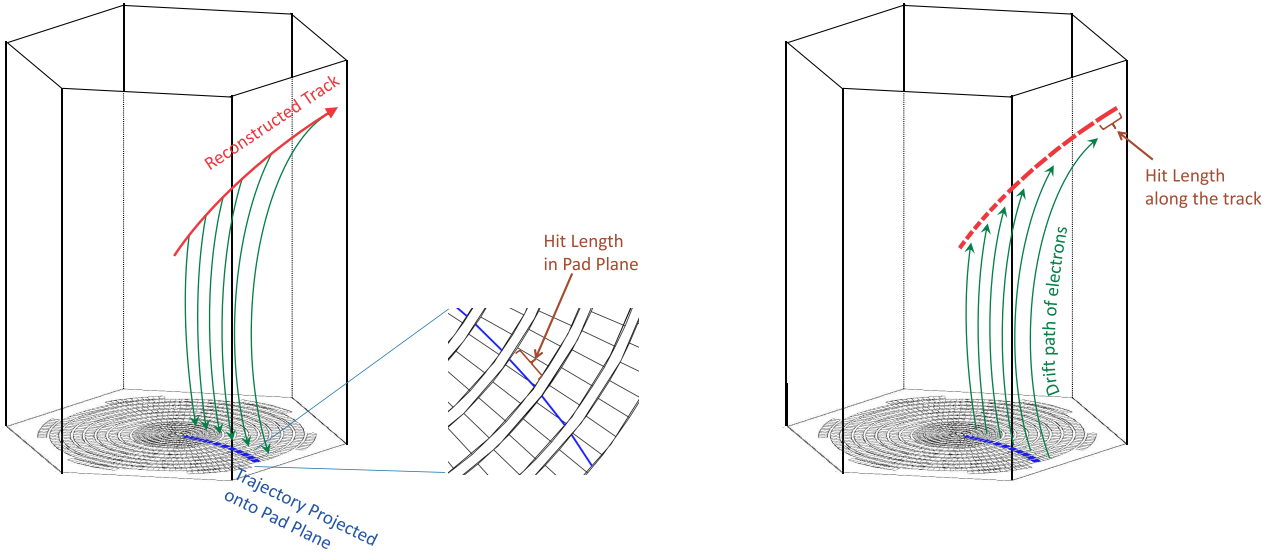


Figure B.9: Conceptual diagrams of $(dx)_{\text{cathode}}$ (left) and $(dx)_{\text{hit}}$ (right).

B.6 Particle Identification (PID)

In this section, we described the calculation and correction of dE/dx , the decision of selection boundary of dE/dx for PID, and their validity.

B.6.1 Truncation and Weighted Average of dE/dx

The fluctuations of energy loss by ionization of a charged particle in a thin layer of matter is described with an asymmetric probability density function [36–38]. This makes the mean and the width of the energy loss distribution to be larger, and requires the multiple samples and the truncated mean analysis to achieve good particle identification.

In the experiments with the large-size of TPC, the truncated mean method - the multiple energy loss samples along the ionization track are evaluated and then a fixed fraction of higher side values are rejected - is used for calculating dE/dx , to get rid of the Landau tail.

However, for the TPC in this experiment, the truncated mean method with a fixed fraction rejection is inappropriate because of the limited number of energy loss samples which came from the size limitation of this TPC. To achieve a good performance of the particle identification with the small number of samples, we adopted not the fixed fraction rejection but truncated mean method using the dE/dx resolution and the weighted average of dE/dx . The procedures are discussed in detail below.

The truncation and the weighted average of dE/dx has been calculated in the following way:

- *Step.1*
Calculating the $(dE/dx)_{\text{hit}_i}$ in each hit along a track.

- *Step.2*

When the track leaves the active gas volume in the middle of the virtual sensitive segment, the corresponding hit is rejected in the calculation of dE/dx . Here, the virtual sensitive segment means the gas volume in which the drift electrons reach into the fired pad, and has a three-dimensional curved shape under the influence of a magnetic field.

- *Step.3*

Calculating the $(dE/dx)_{\text{expect}_i}$, which is the expected value of dE/dx for the i -th hit, is described as

$$\begin{aligned} (dE/dx)_{\text{expect}_i} &= \frac{\sum_{j \neq i} \omega_j (dE/dx)_{\text{hit}_j}}{\sum_{j \neq i} \omega_j}, \\ \omega_j &= \frac{1}{\sigma_j^2}, \end{aligned} \quad (\text{B.2})$$

where the σ_j is the $(dE/dx)_{\text{hit}}$ resolution of j -th hit, and discussed in detail later.

- *Step.4*

Calculating the $(dE/dx)_{\text{residual}_i}$ in each hit, which is the residual of (dE/dx) defined as

$$(dE/dx)_{\text{residual}_i} = (dE/dx)_{\text{hit}_i} - (dE/dx)_{\text{expect}_i}. \quad (\text{B.3})$$

- *Step.5a*

Calculating the following variables x_i in each hit, defined as

$$x_i = \frac{1}{\sigma_i} \cdot \frac{(dE/dx)_{\text{residual}_i}}{(dE/dx)_{\text{expected}_i}}. \quad (\text{B.4})$$

When the largest x_i in all hits along the track is larger than the “*threshold of truncation*”, the hit that the largest x_i belongs to is truncated in the calculation of dE/dx , and we return to *Step.2*.

- *Step.6a*

Calculating the $(dE/dx)_{\text{wav}}$, which is the weighted average of $(dE/dx)_{\text{hit}_i}$ only with the all remaining hits. It described as

$$\begin{aligned} (dE/dx)_{\text{wav}} &= \frac{\sum \omega_i (dE/dx)_{\text{hit}_i}}{\sum \omega_i}, \\ \omega_i &= \frac{1}{\sigma_i^2}. \end{aligned} \quad (\text{B.5})$$

The optimal truncation is set where “the RMS of $(dE/dx)_{\text{wav}}$ ” / $\langle (dE/dx)_{\text{wav}} \rangle$ is minimized. Figure B.10 shows the $(dE/dx)_{\text{wav}}$ distributions of the MIP particles with the various truncations: the simple average (a), the weighted average without truncation (b), and the weighted averages with $6\sigma \sim 1\sigma$ truncations (c)~(h). The red lines show the fit results with Gaussian. The MIP selection cut (π^- selection cut) is applied as follows;

- CH₂ target run
- Number of tracks in the LEPS spectrometer == 1 and PID== π^+
- Number of positive track in the TPC == 1 (and assumed as p)
- Number of negative track in the TPC == 1 (and assumed as π^-)
- Vertex is in Target

- Tracking χ^2 probability > 0.02
- $|0. - (p_{x\pi^+} + p_{x\pi^-} + p_{xp})| < 0.1 \text{ GeV}/c$
- $|0. - (p_{y\pi^+} + p_{y\pi^-} + p_{yp})| < 0.1 \text{ GeV}/c$
- $|p_\gamma - (p_{z\pi^+} + p_{z\pi^-} + p_{zp})| < 0.15 \text{ GeV}/c$
- $|(E_\gamma + E_p) - (E_{\pi^+} + E_{\pi^-} + E_p)| < 0.2 \text{ GeV}/c^2$
- π^- momentum $> 0.35 \text{ GeV}/c$
- π^- polar angle: $60 \sim 120 \text{ deg}$

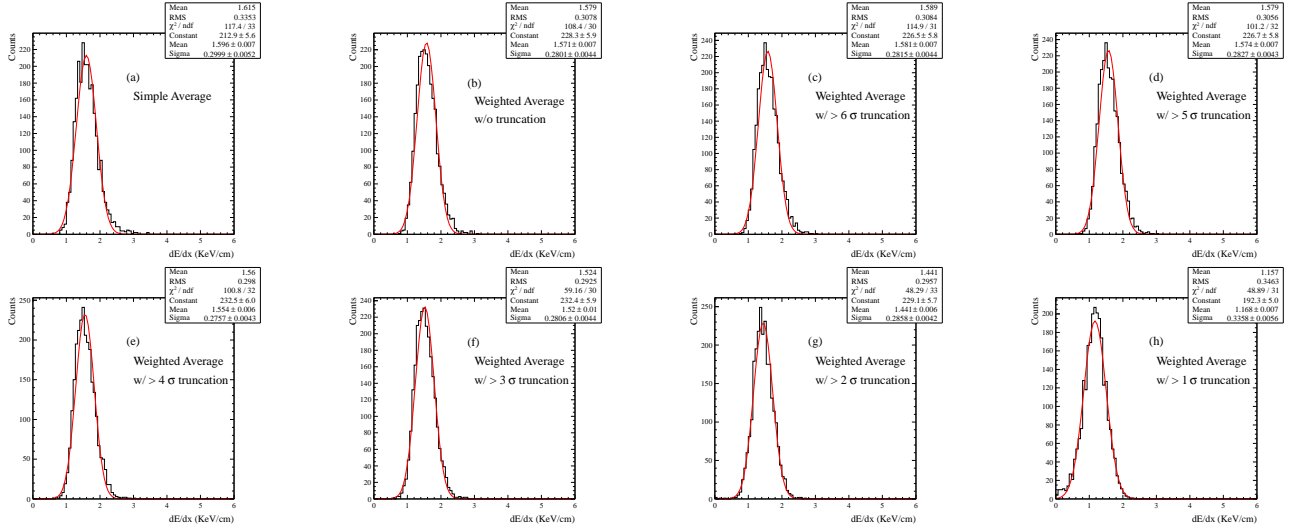


Figure B.10: Distributions of $(dE/dx)_{\text{wav}}$ from the MIP particles with the various truncations: the simple average (a), the weighted average without truncation (b), and the weighted averages with $6\sigma \sim 1\sigma$ truncations (c)~(h). The red lines show the fit results with Gaussian.

Figure B.11 shows the “RMS of $(dE/dx)_{\text{wav}}$ ” / $\langle (dE/dx)_{\text{wav}} \rangle$ with $6\sigma \sim 1\sigma$ truncations, calculated from the result of Fig. B.10. The black and red lines show the results of the simple and the weighted average values without truncation. The optimal truncation in this analysis is set 3σ where “the RMS of $(dE/dx)_{\text{wav}}$ ” / $\langle (dE/dx)_{\text{wav}} \rangle$ is minimized.

The $(dE/dx)_{\text{hit}}$ resolution using in the above procedures has been estimated in the following way:

- *Step.1 ~ Step.4*

Same as the procedures for calculating the $(dE/dx)_{\text{wav}}$.

- *Step.5b*

Making the distribution of the following variables y_i in each hit, defined as

$$y_i = \frac{(dE/dx)_{\text{residual}_i}}{(dE/dx)_{\text{expected}_i}}. \quad (\text{B.6})$$

And the $(dE/dx)_{\text{hit}}$ resolution σ_i is estimated as the RMS of the y_i distributions in each polar angle, each energy deposition, and each layer.

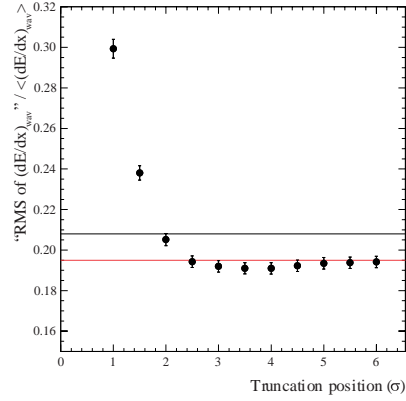


Figure B.11: “RMS of $(dE/dx)_{wav}$ ” / $\langle (dE/dx)_{wav} \rangle$ with $6\sigma \sim 1\sigma$ truncations. The black and red lines show the results of the simple and the weighted average values without truncation.

The $(dE/dx)_{hit}$ resolution depends on mainly the track polar angle and the amount of energy deposition, corresponding to the pulse shape and the pulse height respectively. Figure B.12 shows a sample of $(dE/dx)_{hit}$ resolution as a function of the energy deposition, at layer 4 and at polar angle between 30 and 40 degrees.

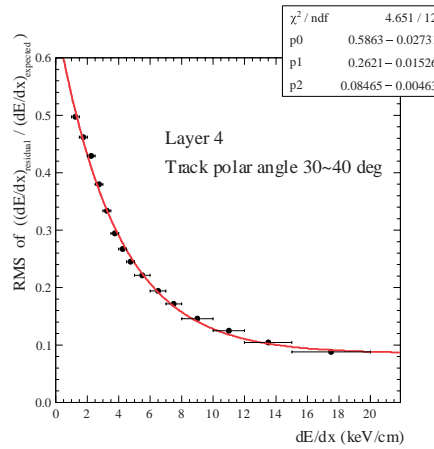


Figure B.12: A sample of $(dE/dx)_{hit}$ resolution as a function of the energy deposition, at layer 4 and at polar angle between 30 and 40 degrees.

B.6.2 Gain Drop due to the Space Charge

In the avalanche process, the electrons created in the avalanche are collected in a very short time, but a cloud of positive ions is remained and move slowly away from the sense wire. When the cloud of ions created in the avalanche are accumulated near the sense wire (called as “*Space Charge*”), it influences the next avalanche of the subsequent incoming electrons. This space charge changes a shape of potential and leads to a local reduction of the electric field near the sense wire as shown in Fig. B.13 and Fig. B.14, and

causes a reduction of the gas amplification factor. This gain drop is reported in the high-rate performance of gas chambers.

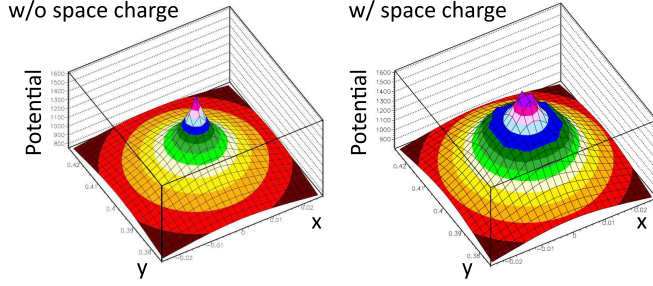


Figure B.13: Contour plots of potential near a sense wire without (left) and with (right) the space charge effect, calculated using the GARFIELD program [32]. The space charge reduces the gradient of potential.

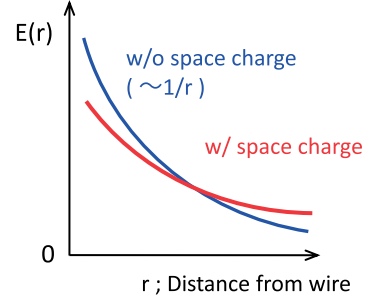


Figure B.14: The conceptual diagram of the local reduction of the electric field near a sense wire. The blue and red lines shows the electric fields without (left) and with (right) the space charge effect.

Meanwhile, the space charge can also be a matter of the gain drop even for a single track in the low-rate environment. We measured the magnitude of gain drop as a function of the ion-pair density, therefore the avalanche density, on cathode plane. This is an approximation. In a precise sense, we should measured as a function not on cathode “plane”, but on sense “wire”. Here, the small variations caused by the angle between the pad and wires are canceled in the procedures for the gain calibration in Sec. B.2, so we adopted the avalanche density on cathode “plane” in the following procedures.

Figure B.15 shows the two dimensional correlation plots suggesting the magnitude of gain drop effect. Horizontal axis represents the *observed* energy deposition divided by the track path length projected into cathode plane. This corresponds to “the *observed* avalanche density on sense wires, which is the result after the gain drop”. Vertical axis represents the *expected* energy deposition divided by the track path length projected into cathode plane. “The expected energy deposition” equals to “the dE/dx value predicted by Bethe-Bloch formula” multiplied by “the track path length in three dimension”, assuming that the charged particle is p , K^+ , d , and π^- in the 1st \sim 4th rows, respectively. The vertical axis corresponds to “the *expected* avalanche density on sense wire without the gain drop”. The data points in all figures, therefore in any polar angle and any particle, are concentrated on the same curved line. This means the magnitude of gain drop effect only depend to the avalanche density on sense wire. The relation function $gain_func(x)$ is obtained as

$$func_gaindrop(x) = 1.05x + 0.03x^2 + 0.002x^3 + 0.00077x^4. \quad (\text{B.7})$$

The gain drop correction for dE/dx is applied as follow:

$$(dE/dx)_{corrected} = (dE/dx)_{wav} * \text{Gain correction factor}. \quad (\text{B.8})$$

Here, the gain correction factor is described using the Equation B.7 as follows:

$$\text{Gain correction factor} = (dE/dx)_{cathode} / func_gaindrop((dE/dx)_{cathode}), \quad (\text{B.9})$$

where

$$\begin{aligned}
 (dE/dx)_{\text{cathode}} &= \text{Total charge along the track} / \text{Track length on cathode plane} \\
 &= (dE/dx)_{\text{wav}} * \text{Track length in space} / \text{Track length on cathode plane} \\
 &= (dE/dx)_{\text{wav}} * \sum (dx)_{\text{space}_i} / \sum (dx)_{\text{cathode}_i} .
 \end{aligned} \tag{B.10}$$

i represents the index of hits constitute of the track, and the track length in Equation B.10 is obtained by summing all hits constitute of the track except the hits removed in the truncation process.

Figure B.16 shows the correlation polots between the dE/dx and the track polar angle of a positively charged particle measured by the TPC before (top) and after (bottom) the gain drop correction. The gain drops found in the tracks with the polar angle far from 90 degrees are corrected.

Figure B.17 shows the correlation between the dE/dx and the momentum of a positively charged particle measured by the TPC before (top) and after (bottom) the gain drop correction, and the red lines show the expected energy losses given from the Bethe-Bloch formula. The gain drops found in the tracks with small $\beta\gamma$ are corrected, and the corrected dE/dx values are good agreement with the Bethe-Bloch formula.

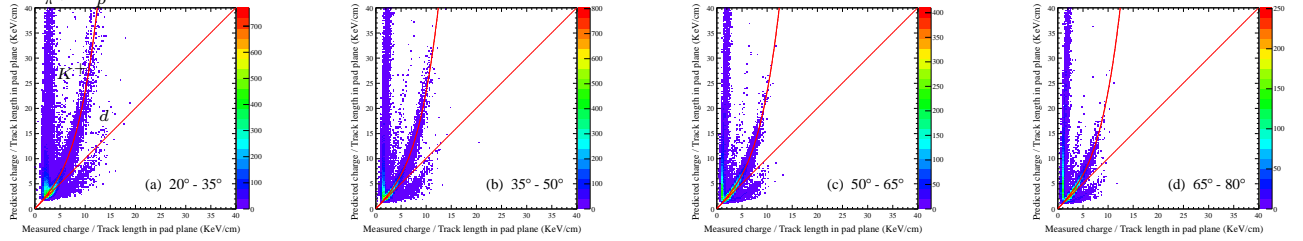
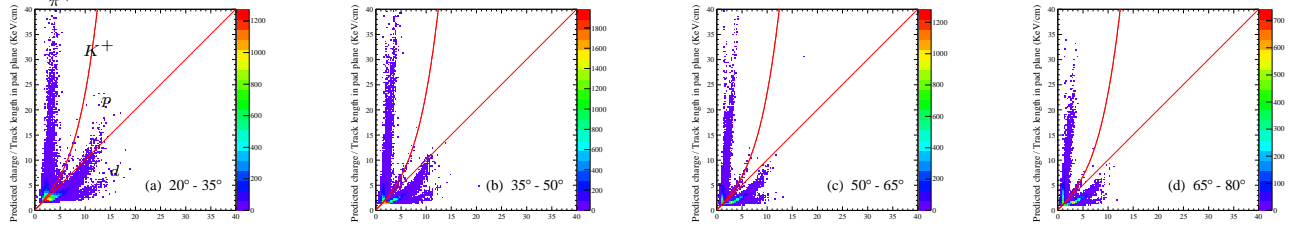
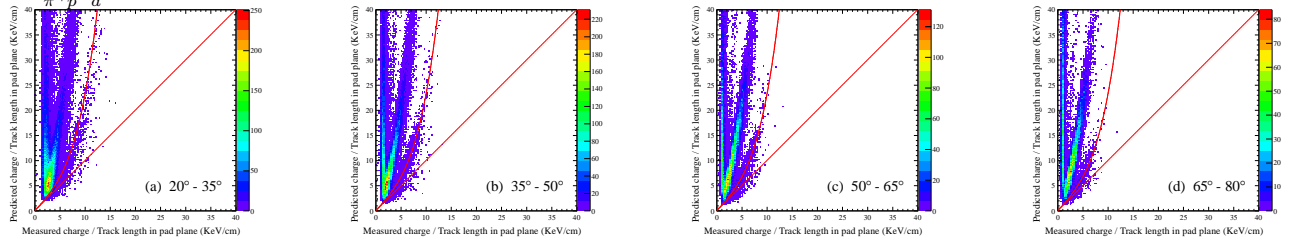
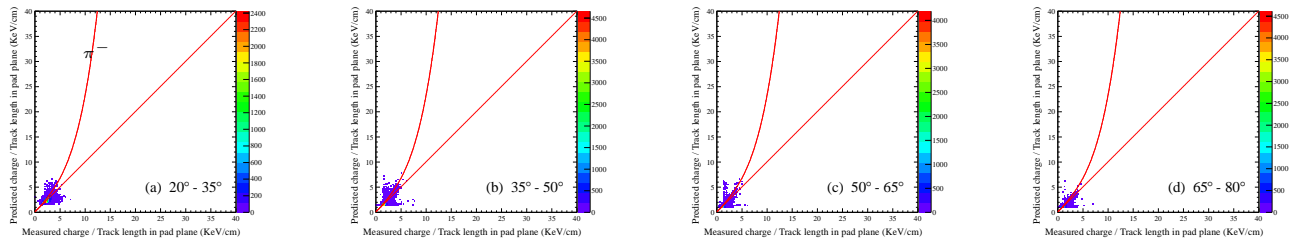
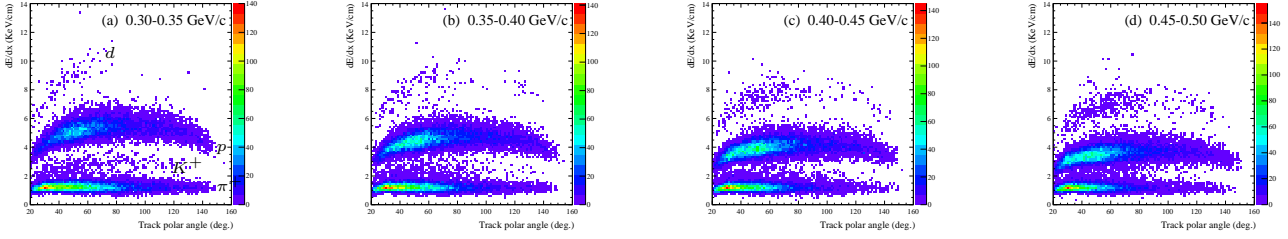
Assumed as p Assumed as K^+ Assumed as d Assumed as π^- 

Figure B.15: Correlation plots suggesting the magnitude of gain drop effect. Horizontal axis represents the *observed* avalanche density on sense wires, which is the result after the gain drop. Vertical axis represents the *expected* avalanche density on sense wire without the gain drop, assuming that the charged particle is p , K^+ , d , and π^- in the 1st \sim 4th rows, respectively. The curved line is the function representing the magnitude of gain drop effect.

Before Correction



After Correction

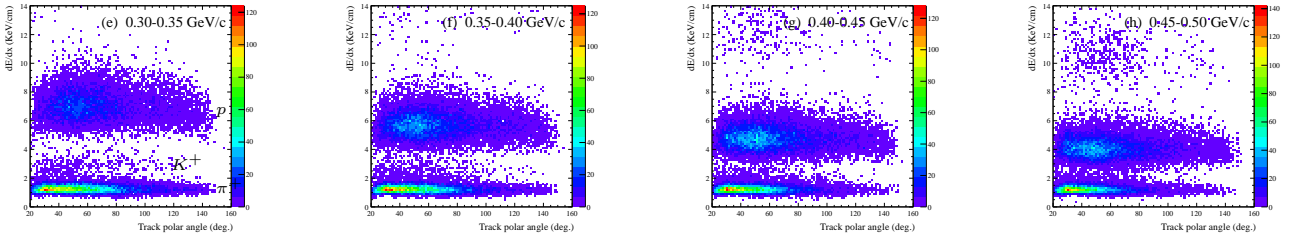
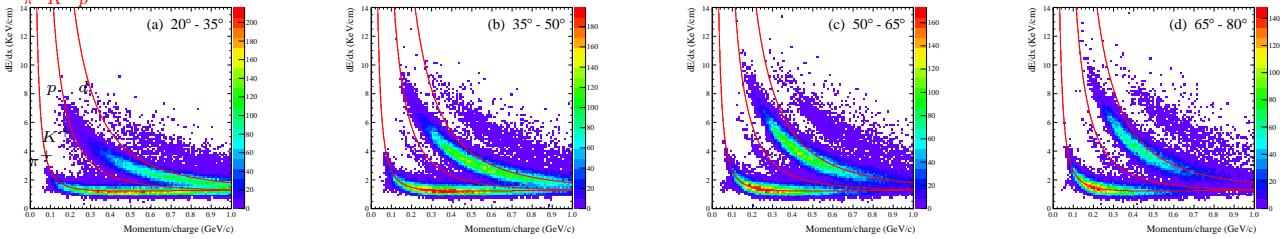


Figure B.16: Correlation between the dE/dx and the track polar angle of a positively charged particle measured by the TPC before (top) and after (bottom) the gain drop correction.

Before Correction



After Correction

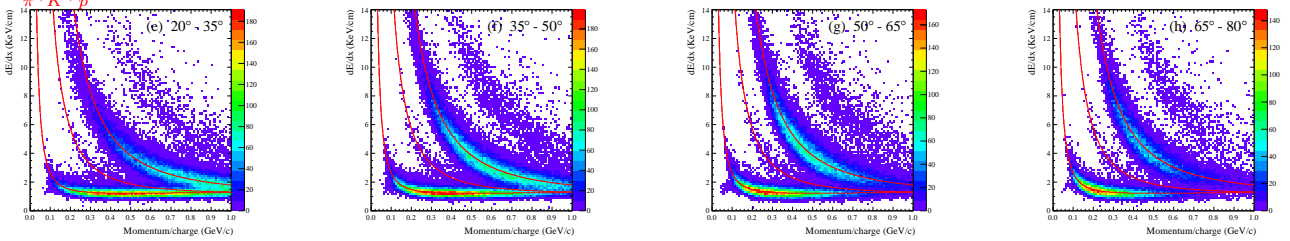


Figure B.17: Correlation between the dE/dx and the momentum of a positively charged particle measured by the TPC before (top) and after (bottom) the gain drop correction. The red lines show the expected energy losses given from the Bethe-Bloch formula.

B.6.3 Selection Boundaries of dE/dx

The selection boundaries of dE/dx for PID are determined using the dE/dx resolution. The (dE/dx) resolution (in three dimensional coordinate) is described by a $(dE/dx)_{\text{cathode}}$ resolution (on cathode plane) as follows:

$$(dE/dx) \text{ resolution} = (dE/dx)_{\text{cathode}} \text{ resolution} * (dE/dx)/(dE/dx)_{\text{cathode}}, \quad (\text{B.11})$$

The $(dE/dx)_{\text{cathode}}$ resolution is obtained in the following way.

Figure B.18 shows the conceptual diagram for obtaining the peak positions *Mean* and the widths *Sigma* of p and π^+ in the distribution of $(dE/dx)_{\text{cathode}}$ at certain polar angle and momentum. These variables are obtained from Gaussian fitting. Figure B.19 shows the correlation plot between the *Mean* and the *Sigma/Mean* at various polar angles and momenta. The *Mean* and the *Sigma/Mean* are corresponding to the $(dE/dx)_{\text{cathode}}$ and the 1σ relative deviation of $(dE/dx)_{\text{cathode}}$, respectively. In this figure, the data points concentrate on the curved line, being independent of the particle, the polar angle, and the momentum. This suggests that the $(dE/dx)_{\text{cathode}}$ relative deviation depends only on the value of $(dE/dx)_{\text{cathode}}$, and we obtained the relation function for 1σ relative deviation of $(dE/dx)_{\text{cathode}}$ by the two dimensional fitting, where the fitting function used is

$$1\sigma \text{ relative deviation of } (dE/dx)_{\text{cathode}} = \text{FitPar} / \sqrt{(dE/dx)_{\text{cathode}}}. \quad (\text{B.12})$$

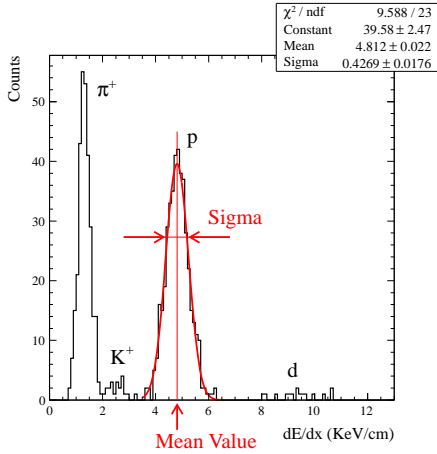


Figure B.18: Conceptual diagram for obtaining the peak positions *Mean* and the widths *Sigma* of p and π^+ in the distribution of $(dE/dx)_{\text{cathode}}$ at certain polar angle and momentum.

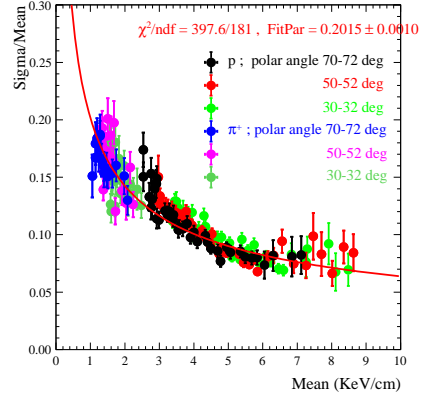


Figure B.19: Correlation plot between the *Mean* and the *Sigma/Mean* at various polar angles and momenta. The *Mean* and the *Sigma/Mean* are corresponding to the $(dE/dx)_{\text{cathode}}$ and the 1σ relative deviation of $(dE/dx)_{\text{cathode}}$, respectively.

Validation

The validity of the selection boundaries for the PID is confirmed by checking the correlation between the selection boundary for Kaon and the amount of observed ϕ mesons. Figure B.20 and Fig. B.21 show the yields of ϕ mesons as a function of the selection boundary cuts for Kaon in the $tpcK^\pm spK^\mp$ and $tpcK^+K^-$ mode, respectively. The data and statistical expectation show a good agreement in all figures, and this indicates that the selection boundaries for Kaon are appropriate.

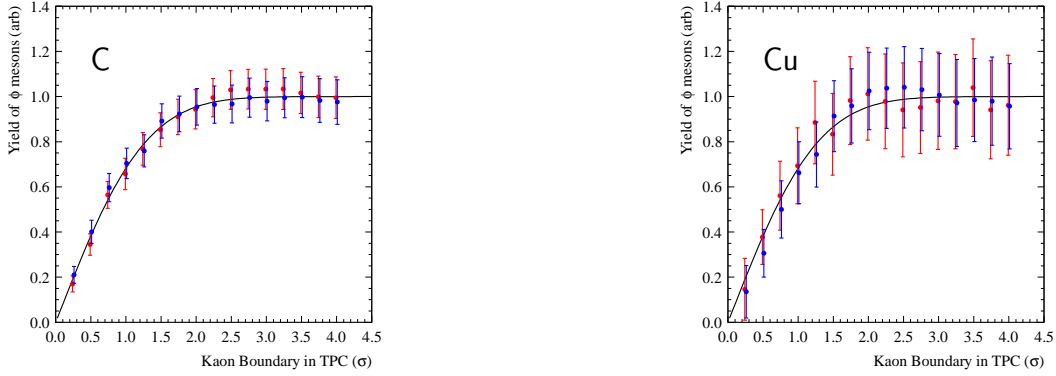


Figure B.20: The yields of ϕ mesons as a function of the selection boundary cuts for Kaon in the $tpcK^+spK^-$ and $tpcK^-spK^+$ mode. The blue and red points represents the yields of ϕ mesons in the $tpcK^+spK^-$ and $tpcK^-spK^+$ mode, respectively. The data show a good agreement with the statistical expectation (black line).

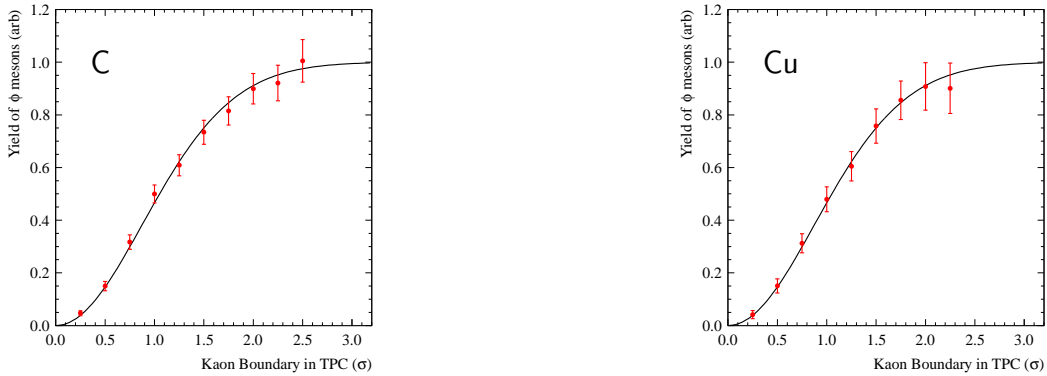


Figure B.21: The yields of ϕ mesons as a function of the selection boundary cuts for Kaon in the $tpcK^+K^-$ mode. The red points represents the yields of ϕ mesons in the experimental data. The data show a good agreement with the statistical expectation (black line).

Most Appropriate Cut Positions for PID

In the analysis for ϕ meson production, the optimal selection boundary cut for Kaon PID is set where the ratio “Error of the yield of ϕ mesons / Yield of ϕ mesons” is minimized. This value is determined for

each detection mode. Figure B.22 and Fig. B.23 show the diagrams of the ratio “Error of the yield of ϕ mesons / Yield of ϕ mesons” as a function of the selection boundary cuts for Kaon in the $tpcK^\pm spK^\mp$ and $tpcK^+K^-$ mode, respectively. The optimal selection boundary cuts for Kaon are set to be 2.0σ in the $tpcK^\pm spK^\mp$ mode, and 1.5σ in the $tpcK^+K^-$ mode, respectively.

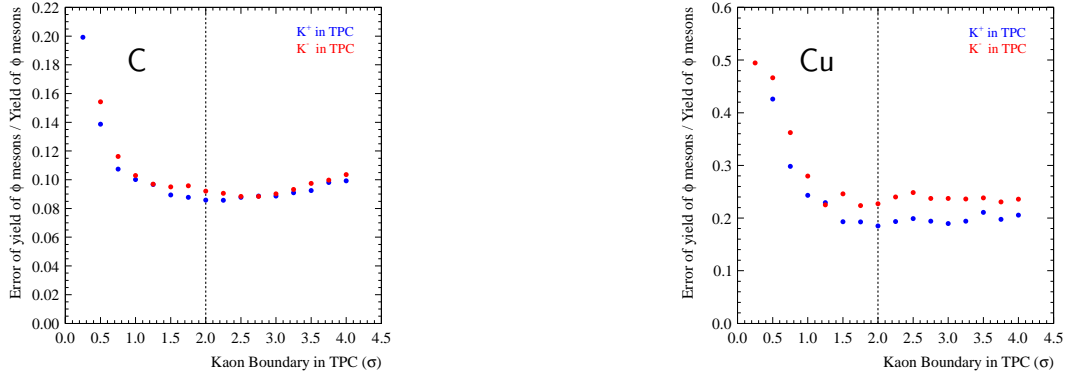


Figure B.22: The ratio “Error of the yield of ϕ mesons / Yield of ϕ mesons” as a function of the selection boundary cuts for Kaon in the $tpcK^+ spK^-$ and $tpcK^- spK^+$ mode. The blue and red points correspond to the $tpcK^+ spK^-$ and $tpcK^- spK^+$ mode, respectively. The optimal selection boundary cut for Kaon is set to be 2.0σ where the ratio is minimized.

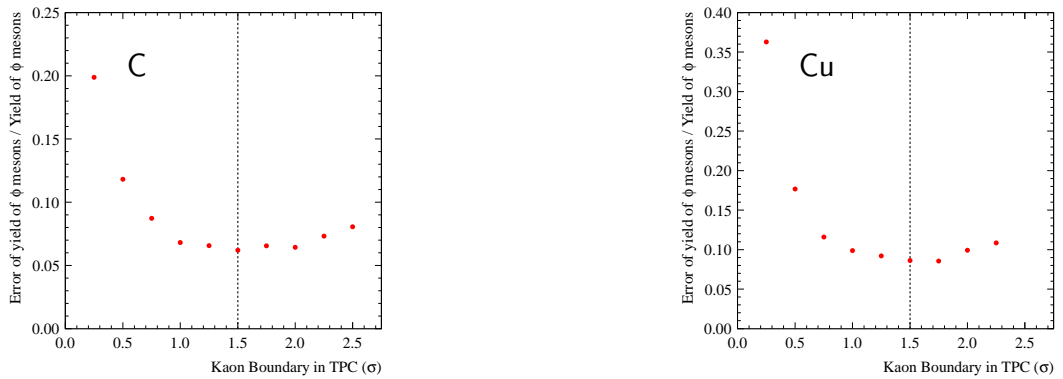


Figure B.23: The ratio “Error of the yield of ϕ mesons / Yield of ϕ mesons” as a function of the selection boundary cuts for Kaon in the $tpcK^+K^-$ mode. The optimal selection boundary cut for Kaon is set to be 1.5σ where the ratio is minimized.

Appendix C

Acceptance Correction

By taking the ratio, the systematic contributions from detector acceptances, detector inefficiencies, and analysis inefficiencies are canceled out. The remaining contribution is mainly from the difference in the attenuation of the charged particles in each target material. The thicknesses of all the targets in this experiment are set to 10 % of the radiation length: 22.4 mm for C and 1.4 mm for Cu target, respectively. As shown in Table. 2.2, these thicknesses corresponded to 7.21 % and 1.53 % of the nuclear collision length, and 4.98 % and 0.94 % of the nuclear interaction length for C and Cu target, respectively. The difference of the nuclear collision/interaction length between C and Cu target cause the difference of the magnitude of attenuation for the particles through each nuclear target, with the momentum dependence.

This attenuation is estimated using the GHEISHA routine [39] in GEANT3 package and the acceptance correction is done, so its accuracy directly affect the transparency ratio. We have verified the validity of the results from GHEISHA routine by comparing to the experimental data using the proton attenuation in the $\gamma A \rightarrow \pi^+ \pi^- p X$ process. Figure C.1 (left) shows the transparency ratio for proton in the $\gamma A \rightarrow \pi^+ \pi^- p X$ process as a function of the proton momentum in the *tpc* $\pi^+ \pi^- p$ detection mode. The red points represent the results from Monte Carlo simulation with GHEISHA routine and the black points represent the results from experimental data. The significant enhancements are observed in both data at the low momentum. This is caused by the fact that the proton-nucleon interaction is very strong in the low momentum (e.g. $\sigma_{pp} = 155$ mb, $\sigma_{pn} = 498$ mb at the $p_p = 0.19$ GeV/c [20].) and emphasized the difference of the nuclear collision/interaction length between C and Cu target. Even the difference of scale exists between the two data, the ratio of Monte Carlo to experimental data is almost constant within the error bars even in the low momentum region, and is shown in Fig. C.1 (right). Figure C.2 shows the results in the *tpc* $\pi^\pm p$ *sp* π^\mp detection mode, and the similar results are obtained.

These results indicate that the estimation of the attenuation of the charged particles in each target material is valid, and does not make the momentum dependent.

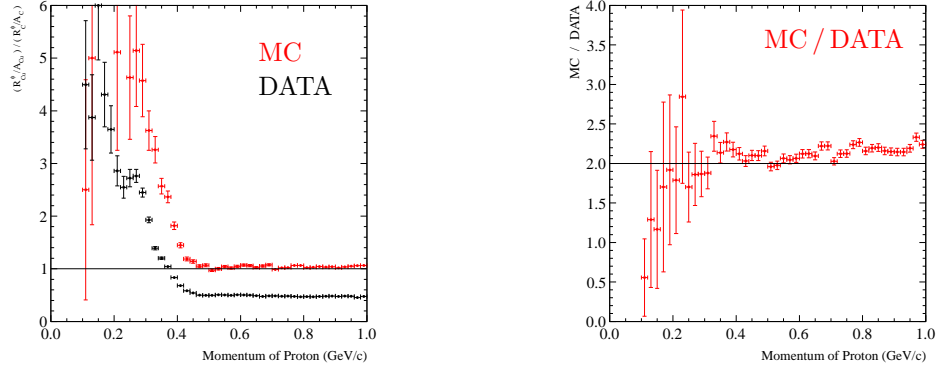


Figure C.1: (Left): The transparency ratio for proton in the $\gamma A \rightarrow \pi^+ \pi^- p X$ process as a function of the proton momentum in the $tpc \pi^+ \pi^- p$ detection mode. The red points represent the results from Monte Carlo simulation with GHEISHA routine and the black points represent the results from experimental data. (Right): The ratio of the transparency ratios obtained from the Monte Carlo simulation and the experimental data. The black line is only guide line drew by eye.

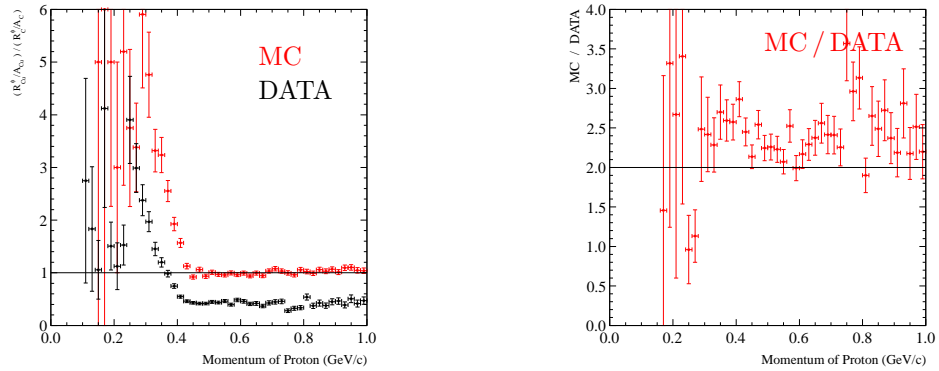


Figure C.2: (Left): The transparency ratio for proton in the $\gamma A \rightarrow \pi^+ \pi^- p X$ process as a function of the proton momentum in the $tpc \pi^\pm p sp \pi^\mp$ detection mode. The red points represent the results from Monte Carlo simulation with GHEISHA routine and the black points represent the results from experimental data. (Right): The ratio of the transparency ratios obtained from the Monte Carlo simulation and the experimental data. The black line is only guide line drew by eye.

Appendix D

Scattering of Emitted Nucleon

In the data taking, we have requested by the trigger level that three or more charged particles are detected in the final state (See in Sec. 2.8). When the emitted nucleon from the $\gamma N \rightarrow \phi N$ process makes no-scattering or elastic-scattering with other nucleons in the nucleus, $\gamma p \rightarrow \phi p \rightarrow K^+ K^- p$ process satisfies the trigger but $\gamma n \rightarrow \phi n \rightarrow K^+ K^- n$ doesn't satisfy the trigger. As a result, the observed ϕ production rates from Cu and C have the relation:

$$\frac{R_{Cu}^\phi}{R_C^\phi} \rightarrow \frac{Z_{Cu}}{Z_C}, \quad (\text{D.1})$$

and the transparency ratio is expected to be

$$T = \frac{R_{Cu}^\phi/A_{Cu}}{R_C^\phi/A_C} \rightarrow \frac{Z_{Cu}/A_{Cu}}{Z_C/A_C} \sim 0.914 \quad (\text{D.2})$$

at $\sigma_{\phi N} = 0$.

By contrast, when the emitted nucleon from $\gamma N \rightarrow \phi N$ process makes inelastic-scattering with other nucleons, the 2-step processes like $\gamma n \rightarrow \phi n$, $nN \rightarrow nN^*$ or $\gamma n \rightarrow \phi n$, $nN \rightarrow \pi X$ could satisfy the trigger. This implies that the observed ϕ mesons might be mixed from $\gamma p \rightarrow \phi p$ and $\gamma n \rightarrow \phi n$ processes even if we detect $K^+ K^- p$ in the final state. If the most of emitted nucleons make inelastic-scattering, the observed ϕ production rates from C and Cu have the relation:

$$\frac{R_{Cu}^\phi}{R_C^\phi} \rightarrow \frac{A_{Cu}}{A_C}, \quad (\text{D.3})$$

and the transparency ratio is expected to be

$$T = \frac{R_{Cu}^\phi/A_{Cu}}{R_C^\phi/A_C} \rightarrow 1 \quad (\text{D.4})$$

at $\sigma_{\phi N} = 0$.

We examined the ratio from inelastic process using $K^+ K^- p$ missing mass distributions when the only three particles $K^+ K^- p$ are detected. Here, the $K^+ K^- p$ missing mass $MM(K^+ K^- p)$ is defined as

$$MM^2(K^+ K^- p) = \left(E_\gamma + m_p - \sqrt{m_{K^+}^2 + p_{K^+}^2} - \sqrt{m_{K^-}^2 + p_{K^-}^2} - \sqrt{m_p^2 + p_p^2} \right)^2 - (p_\gamma - p_{K^+} - p_{K^-} - p_p)^2. \quad (\text{D.5})$$

Figure D.1 and Fig. D.2 show the $MM(K^+ K^- p)$ distributions from C and Cu target, respectively. We divided into three bins by the magnitude of $K^+ K^-$ missing momentum, that is the momentum of the

emitted nucleon. Each figure in left, center, or right column corresponds to the momentum of the emitted nucleon, and in top or bottom row corresponds to $tpcK^\pm PspK^\mp$ or $tpcK^+K^-P$ mode, respectively. The black, red, and blue lines show the experimental data, the components from no-scattering or elastic scattering, and the components from inelastic scattering. The number of percentage in figures represents the ratio of no-scattering or elastic scattering components to all. The both figures of C and Cu data indicate that many emitted protons has made a inelastic scattering. Therefore, we consider that the observed ϕ mesons had been mixed from $\gamma p \rightarrow \phi p$ and $\gamma n \rightarrow \phi n$ processes at this momentum region, and we assumed the ϕ production rates from C and Cu have the relation $R_{Cu}^\phi/R_C^\phi \sim A_{Cu}/A_C$ at $\sigma_{\phi N} = 0$ in this analysis.

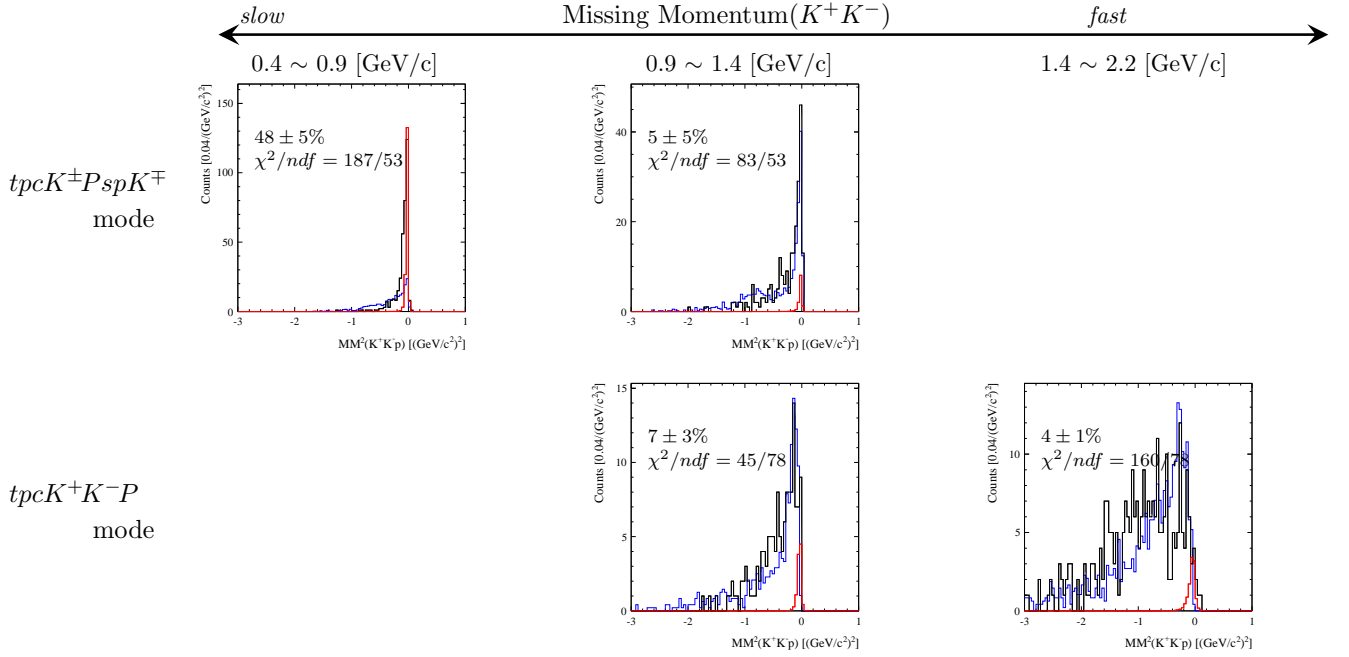


Figure D.1: The $MM(K^+K^-p)$ distributions from C target. Each figure in left, center, or right column corresponds to the momentum of the emitted nucleon, and in top or bottom row corresponds to $tpcK^\pm PspK^\mp$ or $tpcK^+K^-P$ mode, respectively. The black, red, and blue lines show the experimental data, the components from no-scattering or elastic scattering, and the components from inelastic scattering. The number of percentage in figures represents the ratio of no-scattering or elastic scattering components to all.

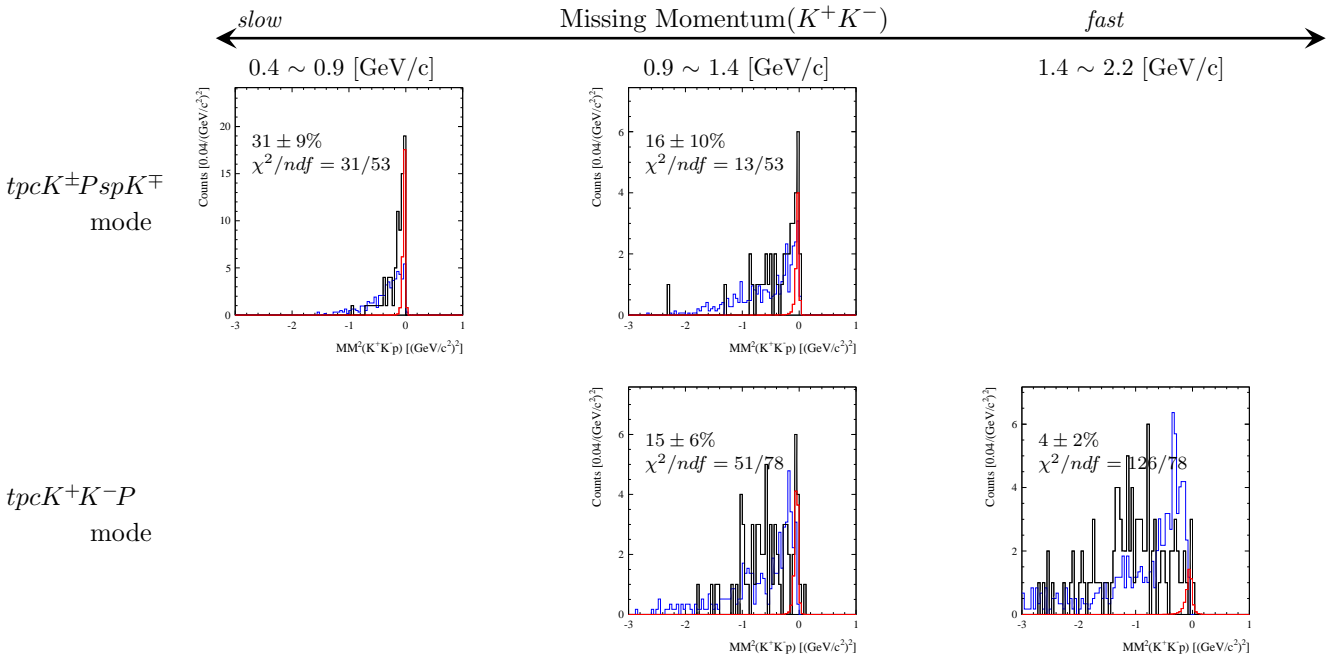


Figure D.2: The $MM(K^+K^-p)$ distributions from Cu target. Each figure in left, center, or right column corresponds to the momentum of the emitted nucleon, and in top or bottom row corresponds to $tpcK^\pm PspK^\mp$ or $tpcK^+K^-P$ mode, respectively. The black, the red, and the blue lines show the experimental data, the components from no-scattering or elastic scattering, and the components from inelastic scattering. The number of percentage in figures represents the ratio of no-scattering or elastic scattering components to all.

Appendix E

Model Calculations

E.1 Glauber Approximation

In this appendix, we described how to relate the transparency ratio and the $\sigma_{\phi N}$.

The basic idea of the eikonal formalism is to express the interaction of a particle with a nucleus in terms of effective two-body interactions. To leading order, the total reaction amplitude is built up from a sum of amplitudes on a single nucleon. The eikonal approximation is proposed by Glauber [11, 40] for incoherent and coherent scattering of hadrons from nuclei. In which, the incident particle is assumed to move along a straight line trajectory through the nucleus and interact independently with each target nucleon, and the final particle move away along the same direction with incident particle. Since the experimental data are collected at some angles in the actual experiments, it is important to estimate how much the transparency ratio is affected by the emission angle of the final particle. Such a estimation is described as below, using a Glauber-type approximation extended for the emission angle influence.

The attenuation probability of a beam of particles i passing through the nucleus at impact parameter \mathbf{b} and longitudinal positions from $-\infty$ to z is then given by

$$S_i(\mathbf{b}, z) = \exp \left[-\sigma_i \int_{-\infty}^z dz' \rho_A(\mathbf{b}, z') \right]. \quad (\text{E.1})$$

The incident particle i interacts with target nucleon at a transverse \mathbf{b} and longitudinal z coordinate and produces the final particle f . When the final particle f is moving along the line fixed at an azimuthal angle ϕ and polar angle θ with respect to the incident particle beam direction, the attenuation probability of passing f through the nucleus in that case is given as

$$S_f(\mathbf{b}, z, \theta, \phi) = \frac{1}{2\pi} \exp \left[-\sigma_f \oint d\xi \rho(|\mathbf{r}_\xi|) \right], \quad (\text{E.2})$$

where the integration is performed along the path of the produced particle f defined by

$$r_\xi^2 = (b + \xi \cos \phi \sin \theta)^2 + (\xi \sin \phi \sin \theta)^2 + (z + \xi \cos \theta)^2. \quad (\text{E.3})$$

Finally, the effective number of target nucleon is evaluated by integration over the nuclear volume as

$$N_A^{eff} = \int d^2b dz \rho(\mathbf{b}, z) S_i(\mathbf{b}, z) S_f(\mathbf{b}, z, \theta, \phi), \quad (\text{E.4})$$

and the transparency ratio T (See in Sec. 4.1) is connected by a relational expression:

$$T = \frac{N_{Cu}^{eff}/A_{Cu}}{N_C^{eff}/A_C}. \quad (\text{E.5})$$

The calculations are performed with a nuclear density function ρ_A taken as a Wood-Saxon distribution:

$$\rho_A(r) = \frac{\rho_0}{1 + \exp[(r - R)/d]}, \quad (\text{E.6})$$

with the density parameters [41]:

$$\begin{aligned} R &= 1.28A^{1/3} - 0.76 + 0.8A^{-1/3} \text{ fm}, \\ d &= \sqrt{3}/\pi \text{ fm}, \end{aligned} \quad (\text{E.7})$$

with the $\sigma_i = \sigma_{\gamma N}$ fixed to be 0.14 mb in the energy range from 1.5 to 2.4 GeV [20], and with the process of ϕ meson decay.

Figure E.1 shows the transparency ratio T calculated from the Equation E.5 ignoring the effect of the $K^\pm N$ interactions. In this experiment, the typical emission angles of ϕ mesons are around 15 degrees in $tpcK^\pm spK^\mp$ mode, and around 30 degrees in $tpcK^+K^-$ mode, respectively. This corresponds to that the reductions of T are 0.2 % and 0.9 % in the case of $\sigma_{\phi N} = 10$ mb, and 1.3 % and 4.6 % in the case of $\sigma_{\phi N} = 30$ mb, respectively. Since these are not so large enough to affect the final result, We made an approximate calculation as being the emission angle is 0 deg in this analysis,

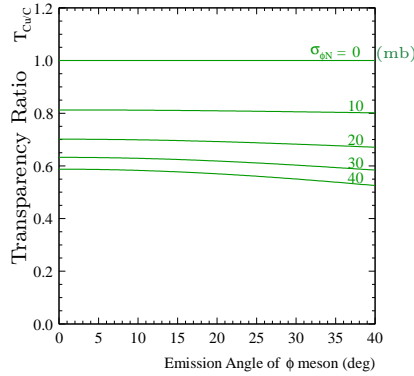


Figure E.1: The transparency ratio T as a function of the emission angle of ϕ meson. The numerical values represent the assumed value of $\sigma_{\phi N}$.

E.2 Decay Probability inside the Nucleus

The relation between N_ϕ^{in}/N_ϕ^{out} is obtained by the Monte Carlo calculation and shown in Fig. E.2. We assumed that the decays inside the half-density radius of the Woods-Saxon distribution contribute to N_ϕ^{in} , and the other to N_ϕ^{out} .

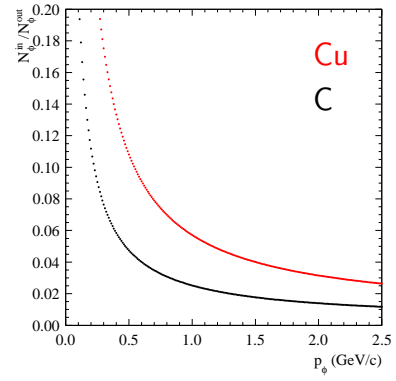
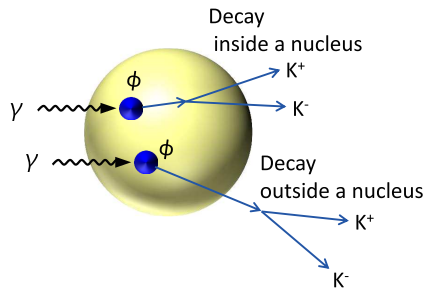


Figure E.2: The conceptual diagram of the ϕ mesons decay inside the nucleus or outside the nucleus (left), and the relation N_ϕ^{in}/N_ϕ^{out} and p_ϕ for C and Cu nuclei obtained by the Monte Carlo calculation (right).

Bibliography

- [1] G. E. Brown and M. Rho. Scaling effective Lagrangians in a dense medium. *Phys.Rev.Lett.*, 66:2720–2723, 1991.
- [2] T. Hatsuda and S. H. Lee. QCD sum rules for vector mesons in nuclear medium. *Phys.Rev.*, C46:34–38, 1992.
- [3] T. Hatsuda, H. Shiomi, and H. Kuwabara. Light vector mesons in nuclear matter. *Prog.Theor.Phys.*, 95:1009–1028, 1996.
- [4] R. Muto et al. Evidence for in-medium modification of the ϕ meson at normal nuclear density. *Phys.Rev.Lett.*, 98:042501, 2007.
- [5] C.M. Ko, P. Levai, X.J. Qiu, and C.T. Li. Phi meson in dense matter. *Phys.Rev.*, C45:1400–1402, 1992.
- [6] H. Kuwabara and T. Hatsuda. phi meson in nuclear matter. *Prog.Theor.Phys.*, 94:1163–1168, 1995.
- [7] F. Klingl, T. Waas, and W. Weise. Modification of the phi meson spectrum in nuclear matter. *Phys.Lett.*, B431:254–262, 1998.
- [8] E. Oset, M.J. Vicente Vacas, H. Toki, and A. Ramos. Test of phi renormalization in nuclei through phi photoproduction. *Phys.Lett.*, B508:237–242, 2001.
- [9] D. Cabrera, L. Roca, E. Oset, H. Toki, and M.J. Vicente Vacas. Mass dependence of inclusive nuclear phi photoproduction. *Nucl.Phys.*, A733:130–141, 2004.
- [10] M. H. Wood et al. Absorption of the ω and ϕ Mesons in Nuclei. *Phys. Rev. Lett.*, 105:112301, 2010.
- [11] R. J. Glauber. High energy physics and nuclear structure, 1967.
- [12] K.S. Kolbig and B. Margolis. Particle production in nuclei and unstable particle cross-sections. *Nucl.Phys.*, B6:85–101, 1968.
- [13] P. Mühlich and U. Mosel. omega attenuation in nuclei. *Nucl.Phys.*, A773:156–172, 2006.
- [14] P. Mühlich and U. Mosel. Attenuation of ϕ mesons in γA reactions. *Nucl.Phys.*, A765:188–196, 2006.
- [15] T. Ishikawa et al. ϕ photo-production from Li, C, Al, and Cu nuclei at $E_\gamma = 1.5\text{-}2.4$ GeV. *Phys. Lett.*, B608:215–222, 2005.
- [16] M. Kotulla et al. Modification of the omega-Meson Lifetime in Nuclear Matter. *Phys.Rev.Lett.*, 100:192302, 2008.

- [17] M. Nanova et al. Transparency ratio in $\gamma A \rightarrow \eta' A'$ and the in-medium η' width. *Phys.Lett.*, B710:600–606, 2012.
- [18] A. Polyanskiy et al. Measurement of the in-medium ϕ -meson width in proton- nucleus collisions. *Phys. Lett.*, B695:74–77, 2011.
- [19] M. Hartmann et al. Momentum dependence of the ϕ -meson nuclear transparency. *Phys. Rev.*, C85:035206, 2012.
- [20] J. Beringer et al. Review of Particle Physics (RPP). *Phys.Rev.*, D86:010001, 2012.
- [21] H. J. Lipkin. Quark Models and High-Energy Scattering. *Phys.Rev.Lett.*, 16:1015–1019, 1966.
- [22] H.-J. Behrend, J. Bodenkamp, W. P. Hesse, D. C. Fries, P. Heine, et al. Photoproduction of ϕ Mesons at Small t Values. *Phys.Lett.*, B56:408, 1975.
- [23] SPring-8 Web Site. <http://www.spring8.or.jp/>.
- [24] PDG. Atomic and Nuclear Properties of Materials. <http://pdg.lbl.gov/2012/AtomicNuclearProperties/>.
- [25] S. Baker and R. D. Cousins. Clarification of the use of chi square and likelihood functions in fits to histograms. *Nucl.Instrum.Meth.*, 221:437–442, 1984.
- [26] XCOM: Photon Cross Sections Database. <http://www.nist.gov/pml/data/xcom/>.
- [27] GEANT3 - Detector Description and Simulation Tool. <http://wwwasd.web.cern.ch/wwwasd/geant/>.
- [28] W.C. Chang et al. Measurement of the incoherent $\gamma d \rightarrow \phi pn$ photoproduction near threshold. *Phys.Lett.*, B684:6–10, 2010.
- [29] D.R. Nygren and J.N. Marx. The Time Projection Chamber. *Phys.Today*, 31N10:46–53, 1978.
- [30] HEED - Modeling of ionization produced by fast charged particles in gases. <http://ismirnov.web.cern.ch/ismirnov/heed/>.
- [31] MAGBOLTZ - Transport of electrons in gas mixtures. <http://consult.cern.ch/writeup/magboltz/>.
- [32] GARFIELD - Simulation of gaseous detectors. <http://garfield.web.cern.ch/garfield/>.
- [33] RADIA. <http://www.esrf.eu/Accelerators/Groups/InsertionDevices/Software/Radia>.
- [34] P. Yepes. A fast track pattern recognition. *Nuclear Instruments and Methods in Physics Research Section A: Accelerators, Spectrometers, Detectors and Associated Equipment*, 380(3):582 – 585, 1996.
- [35] F. James and M. Roos. Minuit: A System for Function Minimization and Analysis of the Parameter Errors and Correlations. *Comput. Phys. Commun.*, 10:343–367, 1975.
- [36] L. Landau. On the energy loss of fast particles by ionization. *J.Phys.(USSR)*, 8:201–205, 1944.
- [37] W. Franzen and L. W. Cochran. Pulse Ionization Chambers and Proportional Counters. In A. H. Snell, editor, *Nuclear Instruments and their Uses, Volume 1*, page 3, 1962.

-
- [38] P.V. Vavilov. Ionization losses of high-energy heavy particles. *Sov.Phys.JETP*, 5:749–751, 1957.
 - [39] H. Fesefeldt. The Simulation of Hadronic Showers: Physics and Applications. *Technical Report PITHA 85-02*, 1985.
 - [40] R. J. Glauber. Boulder lectures in theoretical physics, 1958.
 - [41] Joern Knoll and J. Randrup. Microscopic Study of the Equilibration in High-Energy Nuclear Collisions. *Nucl.Phys.*, A324:445–463, 1979.

Acknowledgments

I would like to express my sincere gratitude to my supervisor Prof. Takashi Nakano. He showed me the philosophy of physics and experiments through the course of my study in the graduate school, that opened deep insights in my mind and brought me to the frontier of the nuclear physics. He gave me encouragements continuously and patiently throughout my research life, which was crucial for accomplishing this work.

I would like to show my great appreciation to Prof. Masaru Yosoi. He have found solutions for many problems about the experimental techniques and advised me every time. I could not carry out the experiment and analysis without his help.

I am deeply grateful to Dr. Masayuki Niiyama. He gave me the great opportunity to work on the TPC experiments at SPring-8/LEPS facility. He gave me many suggestions in many aspects. I respect his deep knowledge and understanding in nuclear physics.

I would like to show my deep gratitude to Prof. Hisako Fujimura. She kindly taught me lots of things about the experiment when I began to participate in this group.

I would like to show my great appreciation to Prof. Wen-Chen Chang. He has been made a great effort to construct the FADC modules and DAQ system for the TPC. He has also given me many helpful advices on the analysis.

I would like to show my deep gratitude for all members of the SPring-8/LEPS collaboration. This work would never finished without their efforts. I would like to thank Ms. Deuk-Soon Ahn, Prof. Jung-Keun Ahn, Prof. Shuji Fukui, Dr. Kate Horie, Dr. Tomoaki Hotta, Dr. Takatsugu Ishikawa, Prof. Kohichi Kino, Dr. Hideki Kohri, Dr. Toru Matsumura Prof. Tsutomu Mibe Prof. Norihito Muramatsu, Mr. Yohei Nakatsugawa, Dr. Yorihiro Sugaya, Prof. Mizuki Sumihama, Dr. Makoto Uchida, and Dr. Tetsuhiko Yorita.

I particularly like to thank Dr. Manabu Miyabe, Dr. Yuji Kato, and Dr. Jia-Ye Chen for their great encouragement. I am sure that this thesis would not be completed without their continuous encouragements. I would like to thank Dr. Schin Date and Dr. Yuji Ohashi for the important roles that they played in preparation and running the SPring-8/LEPS experiments. I would like to express my gratitude to Prof. Hiroyuki Noumi. I have had the many supports and encouragements of him. I appreciate Prof. Harutaka Sakaguchi. He has given me invaluable advices on the physic from his deep insight. Special thanks to Mr. Keiichi Nagayama and Mr. Michio Uraki for sincere and passionate encouragement. I am deeply grateful to the members in Room#300, Prof. Atsushi Tamii and Dr. Kenjiro Miki for warm encouragement. My academic life can not explain without referring to them. Finally, I would like to thank to my parents and brother for their continuous encouragement and supports.